University of Southampton

Faculty of Environmental and Life Sciences

Ocean and Earth Science

Investigation of surface ocean carbon distribution using large global datasets

by

Yingxu Wu

ORCID ID 0000-0002-7847-6215

Thesis for the degree of Doctor of Philosophy

December 2019

University of Southampton

Abstract

Faculty of Natural and Environmental Sciences

Ocean and Earth Science

Thesis for the degree of Doctor of Philosophy

Investigation of surface ocean carbon distribution using large global datasets

Yingxu Wu

Despite considerable progress in our understanding of marine biogeochemistry there are many unknowns. We have probably identified all the major processes (physical and geological as well as biological and chemical) influencing the carbon cycle, but the exact nature and magnitude of the different impacts remain to be fully determined. This study aims at taking advantage of a new wealth of carbonate system observational data coming out of the expansion of research into ocean carbon uptake and ocean acidification. The release of new large datasets (e.g., GLODAPv2: Global Ocean Data Analysis Project version 2) provides an opportunity to make advances in our fundamental understanding (Chapter 2). I compare the distributions of carbon, and some other related parameters (e.g., sea surface temperature, total alkalinity, and nutrients in Chapter 3; dissolved oxygen in Chapter 4) in the surface open ocean to expectations based on current understanding, and derive new understanding (including improved quantification and geographical localization of key processes) from investigation of discrepancies.

To contribute to these goals, I have firstly improved the understanding of the drivers of the global open ocean surface DIC latitudinal gradient (Chapter 3), demonstrating that sea surface temperature effects on CO_2 solubility and high-latitude upwelling (particularly in the Southern Ocean) are the two major factors. I have also clarified the different effects of upwelling depending on the timescale: the short-term effect of upwelling acts immediately, accounting for 98% of the observed nDIC latitudinal gradient; the long-term effect of upwelling acts on timescales of months to a year, accounting for 33% of the observed nDIC latitudinal gradient. Secondly, I have combined and compared the coupled changes in the surface ocean dissolved O_2 and CO_2 (Chapter 4) by developing a new technique, namely Carbon and Oxygen Relative to Saturation (CORS). By using this technique, I have identified regions and periods where processes are driving O_2 and CO_2 away from their equilibrium with the atmosphere. Thirdly, I have used a surface carbon balance

calculation (by taking the Drake Passage as an example) to test the claim, based on SOCCOM float data, of significant rates of CO_2 outgassing from the high-latitude Southern Ocean (Chapter 5). I have shown the implausibility of this finding in the Drake Passage, but with limitation in extrapolating my result to the broader Southern Ocean. I have also applied the CORS technique to float-measured/estimated O_2 and CO_2 data, showing that CORS is capable of distinguishing suspect data from credible data.

Contents

List of tables

List of figures

Declaration of Authorship

Print name: **Yingxu Wu**

Title of thesis: **Investigation of surface ocean carbon distribution using large global datasets**

I declare that this thesis and the work presented in it is my own and has been generated by me as the result of my own original research.

I confirm that:

1. This work was done wholly or mainly while in candidature for a research degree at this University;

2. Where any part of this thesis has previously been submitted for a degree or any other qualification at this University or any other institution, this has been clearly stated;

3. Where I have consulted the published work of others, this is always clearly attributed;

4. Where I have quoted from the work of others, the source is always given. With the exception of such quotations, this thesis is entirely my own work;

5. I have acknowledged all main sources of help;

6. Where the thesis is based on work done by myself jointly with others, I have made clear exactly what was done by others and what I have contributed myself;

7. Either none of this work has been published before submission, or parts of this work have been published as: [please list references below]:

Wu, Y., Hain, M. P., Humphreys, M. P., Hartman, S., and Tyrrell, T.: What drives the latitudinal gradient in open-ocean surface dissolved inorganic carbon concentration?, Biogeosciences, 16, 2661–2681, https://doi.org/10.5194/bg-16-2661-2019, 2019.

Signature: Date:

Acknowledgements

The work completed in the past four years and presented in this thesis cannot exist without the supports and inspirations from my supervisors, colleagues and friends. In no particular order, special thanks and recognition must be given to:

Minhan Dai, for guiding me into marine science since I was a master student at Xiamen University, and for offering me such a great opportunity to start my PhD study at the National Oceanography Centre, Southampton.

Toby Tyrrell and Sue Hartman, for their supervision, support, and encouragement throughout the four-year period of my PhD research. I very appreciate the great efforts, time and patience that Toby has put into supporting me as well as his care for my life as an oversea student. I could always remember the period when my first submission was rejected and followed by the endless revisions. It was Toby's encouragement and insightful suggestions that help me overcome stress and difficulties. I will never forget the moment when the submission was finally received and we toasted our success in Toby's office. There are also a lot of times when Toby shared with me his experiences in publishing papers, writing up thesis, and critical thinking that inspired me a lot on how to proceed my PhD research and even my future career plan.

Matthew Humphreys and Mathis Hain, for taking the time to read and engage with my first publication (Chapter 3), for their insightful comments that have improved it, and for their guidance on the Matlab software.

Eric Achterberg and Dorothee Bakker, for providing valuable contributions to Chapter 4 with their advanced understandings of subjects beyond the scope of my own knowledge.

Peter Brown, for giving me advice on the carbon cycle in the Southern Ocean, and for giving me the inspiration of writing up Chapter 5.

My Chinese friends, especially Xiaolong Yu, Chen Chen, Chuang Xuan, Yuxi Jin, Xiaodong Yang, Wenhao Wang, Guantong Lv, Ruilin Huang, Xiangzhi Chen, Jiayi Hu, Yifu Zhang, for their companies and encouragements throughout my four years life in UK, and for the entertainment they brought to me.

All the crews, scientists, and data analysts that contribute to the global data synthesis (e.g., the GLODAPv2 database), with which most of the data analyses in this thesis are based on.

The Swire Education Trust, for funding the scholarship for my PhD study.

And my family, for always supporting my choice and believing in me.

At last, I would like to quote one saying from my colleague Mathis Hain. It was his words that encouraged and inspired me for quite a long time during the revision of my first publication:

The modern carbon cycle is a tall mountain to climb; many try because it is worth it.

Definitions and Abbreviations

AABW	Antarctic Bottom Water
AAIW	Antarctic Intermediate Water
AASW	Antarctic Surface Water
AAWW	Antarctic Winter Water
ACC	Antarctic Circumpolar Current
Alk*	Alkalinity anomaly, a tracer of calcium carbonate cycling
Alk_m	Measured alkalinity
Alk_r	River alkalinity concentration
APF	Antarctic Polar Front
aq	aqueous
ASZ	Antarctic Southern Zone
$CaCO_3$	Calcium carbonate
CARINA	CARbon dioxide in the North Atlantic
CDW	Circumpolar Deep Water
CO_2	Carbon dioxide
CO_3^{2-}	Carbonate ion
CORS	Carbon and Oxygen Relative to Saturation
DIC	Dissolved inorganic carbon
DP	Drake Passage
ENSO	El Nino-Southern Oscillation
HCO_3^-	Bicarbonate ion
GEOSECS	Geochemical Ocean Sections Study

GLODAP	Global Ocean Data Analysis Project data product
GLODAPv2	Global Ocean Data Analysis Project data product version 2
IPCC	Intergovernmental Panel on Climate Change
K_0	Henry's constant for carbon dioxide (interchangeable with K_H)
K_1	First stoichiometric dissociation constant of carbonic acid
K_2	Second stoichiometric dissociation constant of carbonic acid
LCDW	Lower Circumpolar Deep Water
LDEO	Lamont-Doherty Earth Observatory
LIAR	Locally interpolated alkalinity regression
MATLAB	A numerical computing environment and programming language developed by MathWorks
MLR	Multiple linear regression
NADW	North Atlantic Deep Water
NAO	North Atlantic Oscillation
NCP	Net community production
nDIC	S Salinity-normalized dissolved inorganic carbon
nTA	Salinity-normalized alkalinity
P_{baro}	Barometric pressure
P_{sw}	Water vapor pressure
PACIFICA	PACIFIc ocean Interior CArbon data product
pCO_2	Partial pressure of carbon dioxide
$pCO_{2,atm}$	Atmospheric partial pressure of carbon dioxide (interchangeable with $pCO_{2,air}$)
$pCO_{2,sea}$	Seawater partial pressure of carbon dioxide (interchangeable with $pCO_{2,sw}$)
PDO	Pacific Decadal Oscillation
PFZ	Polar Frontal Zone

Phos	Phosphate concentration
$R_{C:P}$	Redfield ratio of carbon to phosphorus
$R_{DIC:TA}$	Ratio of DIC to TA during primary production
S	Salinity
S_{abs}	Absolute salinity
sat	Saturation
SAF	Subantarctic front
SAMW	Subantarctic Mode Water
SAZ	Subantarctic Zone
SIZ	Seasonal Ice Zone
SOCCOM	Southern Ocean Carbon and Climate Observations and Modeling project
SST	Sea surface temperature
SSW	Summer Surface Water
T	Temperature
T_{14}	Takahashi et al. (2014) Climatology
TA	Total alkalinity
TA_C	Carbonate alkalinity
T_{cons}	Conservative temperature
UCDW	Upper Circumpolar Deep Water
WSW	Winter Surface Water
X	Representative of variables involved (can be referred to DIC, TA, etc.)
X_{supply}	Value at depth, along isopycnals that upwell at this location
X_{surf}	Predicted value in the surface layer
X_{obs}	Observed value at the surface location

$X_{SST=27}$	Predicted value with SST changed to 27°C
X_{nonupw}	Predicted value with upwelled alkalinity subtracted
X_{eq}	Predicted equilibrium value with respect to gas exchange
ΔpCO_2	Difference between $pCO_{2,sea}$ and $pCO_{2,atm}$
ΔX_{temp}	Effect of SST variations
ΔX_{upw_st}	Short-term effect of upwelling
ΔX_{upw_lt}	Long-term effect of upwelling
ΔX_{Fe}	Effect of iron limitation
$[CO_2]$	Concentration of dissolved carbon dioxide in seawater
$[O_2]$	Concentration of dissolved oxygen in seawater
Y^n	Neutral density of seawater

Chapter 1 Introduction

1.1 Research background

Carbon dioxide (CO_2) is one of the most important greenhouse gases that absorb thermal radiation, creating the 'greenhouse effect'. It exists in Earth's atmosphere in relatively small concentrations, but is critical in maintaining a habitable temperature for the planet and sustaining life. Since the industrial revolution, consumption of fossil fuels has led to a large quantity of CO_2 being emitted into the atmosphere, resulting in a rapid increase in the atmospheric CO_2 concentration (Fig. 1.1) and planetary warming (IPCC, 2013).

The ocean absorbs about one quarter of the anthropogenic CO_2 emitted every year (Le Quéré et al., 2018). It is the largest non-geological carbon reservoir (~38000 Gt C; Falkowski et al., 2000), containing 50 times as much carbon as the pre-industrial atmosphere, and for this reason has the potential to modulate the Earth's climate system. Approximately 97% of the carbon in the ocean is in the form of Dissolved Inorganic Carbon (DIC, Eq. 1.2). CO_2 that has diffused in from the atmosphere is transported from the surface ocean into the ocean interior mainly through the solubility and biological pumps (Toggweiler et al., 2003a; Toggweiler et al., 2003b), where it is then isolated from the atmosphere for a timescale of hundreds of years, according to the large-scale ocean circulation (Broecker, 1991). It is reported that about 90% of the anthropogenic CO_2 emissions will end up in the ocean after several thousand years; however, due to the slow mixing time of the ocean, the current oceanic uptake is only about one third of this value (Le Quéré et al., 2018; Sabine et al., 2004).

Although rising atmospheric CO_2 can be tempered by oceanic uptake, it is not benign; as some of the extra CO_2 enters the ocean and dissolves and reacts with seawater, it causes pH reductions and alterations in fundamental chemical balances that together are referred to ocean acidification ("the other CO_2 problem") (Doney et al., 2009). Figure 1.1 records the growth rates of sea surface pCO_2 and atmospheric CO_2 at the Hawaii Ocean Time-Series (HOT) Station ALOHA and shows that they are in a good agreement, accompanied by the corresponding decrease in surface seawater pH (approximately 0.02 units per decade). Ocean acidification also affects the biology of the ocean and threatens marine ecosystems, especially for calcifying organisms such as corals which will have difficulty maintaining their calcium carbonate skeletons (Doney et al., 2009; Orr et al., 2005).

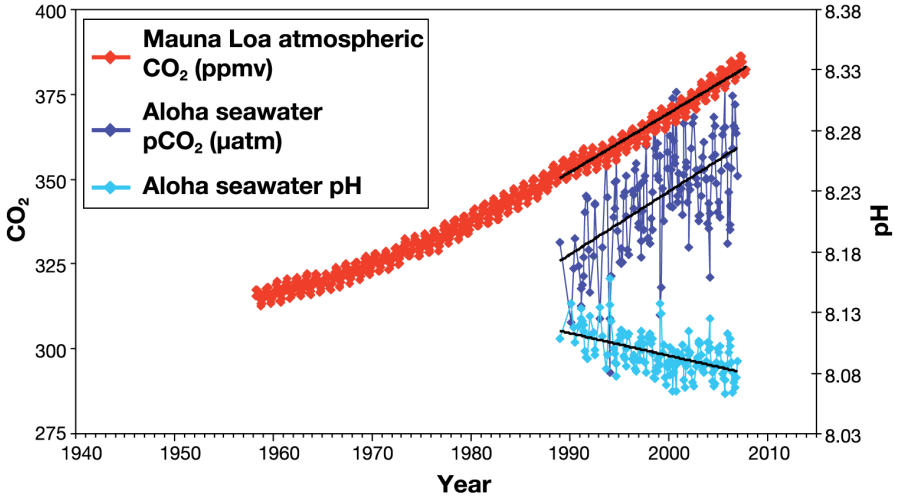

Figure 1.1. Time series of atmospheric CO_2 at Mauna Loa Observatory, together with surface ocean pCO_2 and pH measured at Ocean Station Aloha in the subtropical North Pacific Ocean. Figure adapted from Feely (2008).

Moreover, the global warming induced by human activities also affects other biogenic dissolved gases in seawater, such as dissolved oxygen (O_2), which is inter-converted with CO_2 by marine organisms during organic matter production and remineralization. The warming of seawater reduces the solubility of O_2 and simultaneously enhances stratification, thereby slowing down the ventilation of subsurface waters with atmospheric O_2 (Schmidtko et al., 2017).

The following sections introduce primarily the marine carbonate system (focusing on DIC), with the content of dissolved oxygen introduced in further detail in Chapter 4.

1.2 The marine carbonate system

The marine carbonate system consists of four fundamental measurable parameters: dissolved inorganic carbon (DIC), total alkalinity (TA), pH and partial pressure of CO_2 (pCO_2).

The difference between CO_2 and many other soluble gases is that CO_2 can not only dissolve in seawater, but also reacts with water to form carbonic acid, H_2CO_3, followed by its dissociation into bicarbonate (HCO_3^-) and carbonate (CO_3^{2-}) ions (Zeebe and Wolf-Gladrow, 2001):

$$CO_2 + H_2O \overset{k_0}{\Leftrightarrow} H_2CO_3 \overset{k_1}{\Leftrightarrow} H^+ + HCO_3^- \overset{k_2}{\Leftrightarrow} 2H^+ + CO_3^{2-} \quad (1.1)$$

where k_0 is the Henry's constant for CO_2 (also known as the solubility of CO_2), as a function of seawater temperature and salinity (Weiss, 1974), and k_1 and k_2 are the first and second dissociation constants of carbonic acid, respectively. The sum of the aqueous CO_2, HCO_3^- and CO_3^{2-} concentrations makes up the dissolved inorganic carbon (DIC):

$$DIC = [CO_2^*] + [HCO_3^-] + [CO_3^{2-}] \quad (1.2)$$

where $[CO_2^*]$ refers to the sum of aqueous CO_2 and undissociated H_2CO_3, with the latter negligible (Zeebe and Wolf-Gladrow, 2001).

Under typical seawater conditions (e.g., temperature = 15 °C and salinity = 35, pH = 8.2, atmospheric pCO_2 =380 µatm), most of the dissolved CO_2 is in the form of HCO_3^- (which accounts for about 90% of DIC), followed by CO_3^{2-} (accounting for about 10%), with typically less than 1% contributed by CO_2^*.

Another essential parameter to describe the marine carbonate system is the total alkalinity (TA), which is defined as the excess of proton acceptors over proton donors during an acidimetric titration of seawater to a pH of 4.5 (Dickson, 1981; Wolf-Gladrow et al., 2007):

$$TA = [HCO_3^-] + 2[CO_3^{2-}] + [B(OH)_4^-] + [OH^-] + [HPO_4^{2-}] + 2[PO_4^{3-}] + [H_3SiO_4^-] + [NH_3] + [HS^-] + \ldots - [H^+] - [HSO_4^-] - [HF] - [H_3PO_4] - [HNO_2] - \ldots \quad (1.3)$$

Under typical seawater conditions, the majority of TA is contributed by $[HCO_3^-]$ (~77%) and $2[CO_3^{2-}]$ (~19%). Therefore we can approximate TA by the carbonate alkalinity (TA_C), which only consists of bicarbonate and carbonate ions, with their charge making up together about 95% of TA:

$$TA_C = [HCO_3^-] + 2[CO_3^{2-}] \quad (1.4)$$

TA is also related to the charge balance in seawater, which takes into account the contributions of the most abundant ions: conservative ions (e.g., Na+, Cl-, Mg^{2+}, Ca^{2+}, etc.) derived from strong electrolytes which are effectively completely ionised, and non-conservative ions (e.g., H+, HCO_3^-, CO_3^{2-}, etc.) derived from weak electrolytes (Wolf-Gladrow et al., 2007). Due to the fact that the charge contributions from all cations and anions should balance, TA can therefore be expressed as (Wolf-Gladrow et al., 2007):

$$TA \equiv [Na^+] + 2[Mg^{2+}] + 2[Ca^{2+}] + [K^+] + 2[Sr^{2+}] - [Cl^-] - 2[SO_4^{2-}] - [Br^-] - [F^-] - [NO_3^-] + \ldots = [HCO_3^-] + 2[CO_3^{2-}] + [B(OH)_4^-] + [OH^-] - [H^+] + \ldots \quad (1.5)$$

pH ($-\log_{10}[H^+]$) is a logarithmic scale used to reflect the acidity or basicity of seawater. pH at the ocean surface is observed to be fairly uniform, varying between about 8.0 and 8.2, regulated by the carbonate buffering system (Zeebe, 2012).

CO_2 is exchanged across the air-sea interface, at a rate governed by the difference between the atmospheric and sea surface partial pressures of CO_2. The seawater pCO_2 refers to the partial

pressure of CO_2 in the gas phase that would be found in equilibrium with the seawater. It can be expressed as:

$$pCO_2 = [CO_2]/k_0 \quad (1.6)$$

With the combination of Eq. 1.2, Eq. 1.4, together with the formulas of k_1 and k_2:

$$k_1 = \frac{[HCO_3^-][H^+]}{[CO_2]} \quad (1.7)$$

$$k_2 = \frac{[CO_3^{2-}][H^+]}{[HCO_3^-]} \quad (1.8)$$

The marine carbonate system can therefore be characterized from any two of the four fundamental parameters (DIC, TA, pH and pCO_2) with the equations described above, together with the relevant dissociation constants and auxiliary variable such as salinity, temperature, phosphate and silicate (Zeebe and Wolf-Gladrow, 2001).

1.3 Surface ocean distributions of carbon variables and dissolved oxygen

1.3.1 Dissolved inorganic carbon and its species

Surface observations reveal that DIC ranges between more than 2100 µmol kg^{-1} in the polar regions to less than 2000 µmol kg^{-1} in the tropics (Fig. 1.2). The subarctic Atlantic and Pacific exhibit significantly different DIC values, attributed to the effect of warm saline Atlantic surface water with high alkalinity; DIC flows northwards into the Greenland, Iceland and Norwegian Seas, whereas the northward transport of less saline Pacific water into the Bering Sea is partially impeded by the Aleutian Arc (Takahashi et al., 2014; Woodgate et al., 2006). Another conspicuous feature of surface DIC is the higher values (by ~100 µmol kg^{-1}) in the tropical and subtropical Atlantic Ocean relative to the same latitudes in the Pacific and Indian Oceans (Fig. 1.2a), attributed to the transport of water vapor from the Atlantic to the Pacific (Broecker, 1989). However, the global patterns of DIC and its carbon species are not identical: DIC, $[HCO_3^-]$, and $[CO_2^*]$ generally increase with latitude, while the opposing trend is observed in $[CO_3^{2-}]$ (Fig. 1.2d).

The increases in $[CO_2^*]$ and $[HCO_3^-]$ with latitude are conventionally attributed to the increasing solubility of CO_2 in cooler waters (Williams and Follows, 2011). The concentration of $[CO_3^{2-}]$ can be thought of as the difference between carbonate alkalinity (Eq. 1.4) and DIC, assuming that DIC approximates the sum of bicarbonate and carbonate ions (neglecting the very small proportion of aqueous CO_2). Therefore, $[CO_3^{2-}]$ can be inferred from the opposing trends of carbonate alkalinity

and DIC with latitude: carbonate alkalinity has its maximum in the subtropical gyres due to the net evaporation and decreases polewards (Fry et al., 2015; Takahashi et al., 2014), while DIC increases polewards.

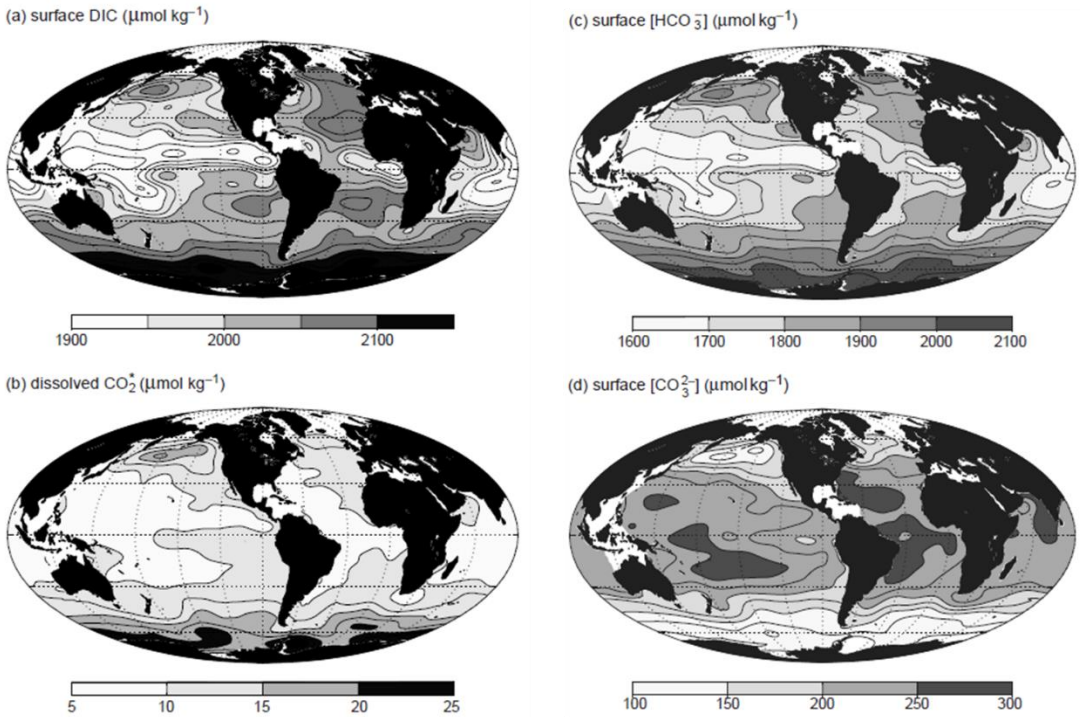

Figure 1.2. Global surface distributions of carbonate system variables. (a) DIC, DIC = $[CO_2^*]$ + $[HCO_3^-]$ + $[CO_3^{2-}]$, (b) aqueous CO_2, $[CO_2^*]$, (c) bicarbonate ion, $[HCO_3^-]$, and (d) carbonate ion, $[CO_3^{2-}]$. The components were determined assuming thermodynamic equilibrium based on climatological DIC and TA values from Key et al. (2004). Figure from Williams and Follows (2011).

1.3.2 Partial pressure of CO_2

The distribution of surface seawater pCO_2 (Fig. 1.3) shows a stronger spatial variability than $[CO_2]$ (Fig. 1.2b) although it is calculated from $[CO_2]$ through solubility. The highest surface pCO_2 over the global open ocean are observed in the tropical zones, especially in the eastern equatorial Pacific upwelling area, the northern Indian Ocean, along the Californian Current in the North Pacific, and also in the high-latitude North Pacific. The lowest surface pCO_2 are whereas observed in the high-latitude North Atlantic, along the North Pacific Current, and in the subtropical bands of the Southern Hemisphere.

In addition, large seasonal variations in pCO_2 are also found between summer and winter, with the most significant changes taking place in the subtropical gyre areas where pCO_2 is dominated by the seasonal temperature changes. The seasonal variation is also noteworthy in the subpolar

and polar areas where pCO_2 increases in winter due to upwelling of deep waters and decreases in summer due to photosynthesis (Takahashi et al., 2014).

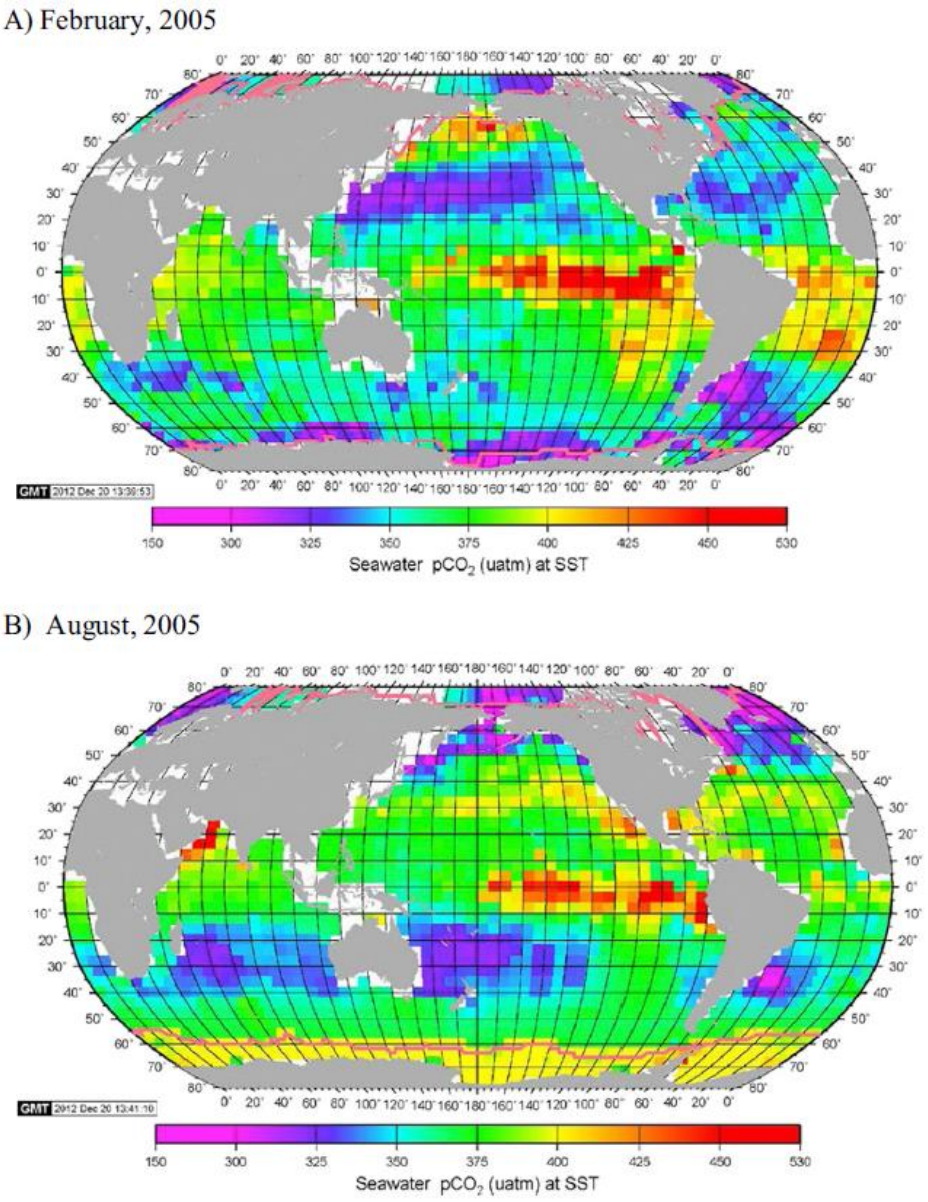

Figure 1.3. Climatological mean distribution of the global surface pCO_2 in the reference year 2005. Figure from Takahashi et al. (2014).

1.3.3 Dissolved oxygen

Figure 1.4 gives a view of the overall supersaturation (average of 3%) of dissolved O_2 over a large fraction of the global surface ocean (Sarmiento and Gruber, 2006). It suggests a reasonably close agreement between the observed O_2 concentration and its temperature-dependent saturation concentration (discussed in more detail in Chapter 4). The supersaturations of O_2 come mostly from regions at low latitude where warmer surface temperatures lead to decreased O_2 solubility.

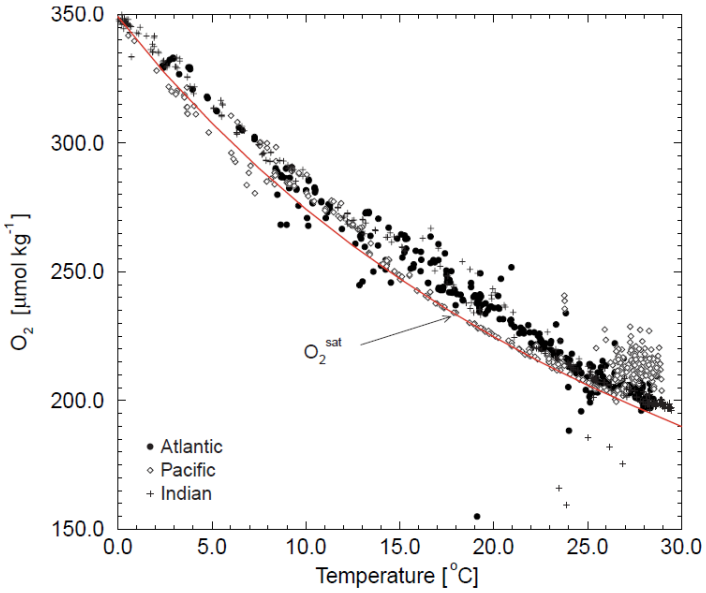

Figure 1.4. Relationship between dissolved oxygen concentration and temperature in the global surface ocean (shallower than 20 m) during a few selected cruises of the GEOSECS program. The red curve shows the calculated saturation concentration of oxygen in equilibrium with the atmosphere. Figure from Sarmiento and Gruber (2006).

Figure 1.5 suggests that there are some similarities in the latitudinal patterns of dissolved O_2 and CO_2 in the surface seawater along a transect from 60°S to 60°N in the Pacific Ocean. Although both [O_2] and [CO_2] exhibit well-recognized latitudinal gradient (Fig. 1.5a,b) due to solubilities, their deviations from the equilibrium values (saturation values) with the atmosphere are different (Fig. 1.5c,d). The fractional departure of surface O_2 from its saturation is on average 0.05 or less over most of the transect, while the fractional departure of CO_2 exhibits a large-scale pattern, ranging from -0.2 to 0.2. This phenomenon is somehow puzzling because the re-equilibration of both these two dissolved gases is driven by the air-sea gas exchange, and it takes roughly the same time for dissolved O_2 and CO_2 in the surface mixed layer to equilibrate with the atmosphere (e.g., assuming a mixed layer depth of 40 m at temperature of 25 °C with a wind speed of 7.5 m s^{-1}, the residence times of O_2 and CO_2 in the surface mixed layer are 8 days and 11 days, respectively; Sarmiento and Gruber, 2006). The answer to this question is the existence of carbon chemistry: free CO_2 only accounts for a minor part (0.5% to 1%) of DIC; therefore DIC buffers changes in the CO_2 concentration and slows down equilibration (Zeebe and Wolf-Gladrow, 2001), resulting in a 20 times longer timescale of re-equilibrium of CO_2 with the atmosphere than other dissolved gases (Jones et al., 2014; Sarmiento and Gruber, 2006; Zeebe and Wolf-Gladrow, 2001).

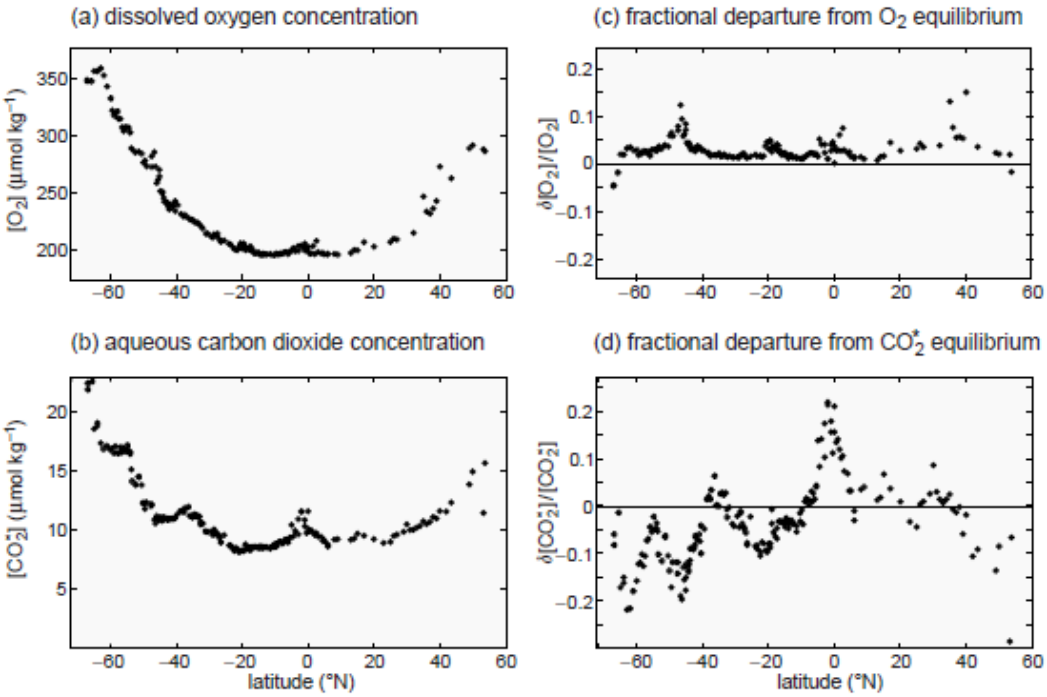

Figure 1.5. Concentrations of different dissolved gases in the surface mixed layer (shallower than 25 m) along 170°W transect in the Pacific Ocean. (a) dissolved O_2, (b) aqueous CO_2 in the surface mixed layer, (c) the fractional departure from equilibrium for dissolved O_2, and (d) the fractional departure from equilibrium for CO_2. Data from Key et al. (2004). Figure from Williams and Follows (2011).

1.4 Variability of DIC in the open ocean

1.4.1 Spatial variability

The vertical distribution of DIC throughout the water column is controlled by a combination of physical, biological and chemical processes. DIC gradually increases with depth (Fig. 1.6) as a result of the solubility pump, biological soft-tissue pump, and carbonate pump (Cameron et al., 2005).

The solubility pump is based on the assumption that, at high latitudes where deep waters form, DIC is high because the low water temperature increases CO_2 solubility. The biological soft-tissue pump refers to the processes of biological production of organic matter in the sunlit, surface ocean, followed by its transportation downward and subsequent decomposition during the sinking process, enhancing deep DIC with respired CO_2. The carbonate pump refers to the formation, transportation, and dissolution of calcium carbonate ($CaCO_3$), from the upper ocean to the deep.

The vertical distribution of DIC also differs in each basin (Fig. 1.6). In the Pacific, there seems to be a relatively large vertical gradient compared to that in the Atlantic. The strong Atlantic-Pacific contrast is due to the fact that, because of the "conveyor belt", younger waters in the deep Atlantic hold less DIC, whereas older waters in the deep Pacific hold more regenerated DIC.

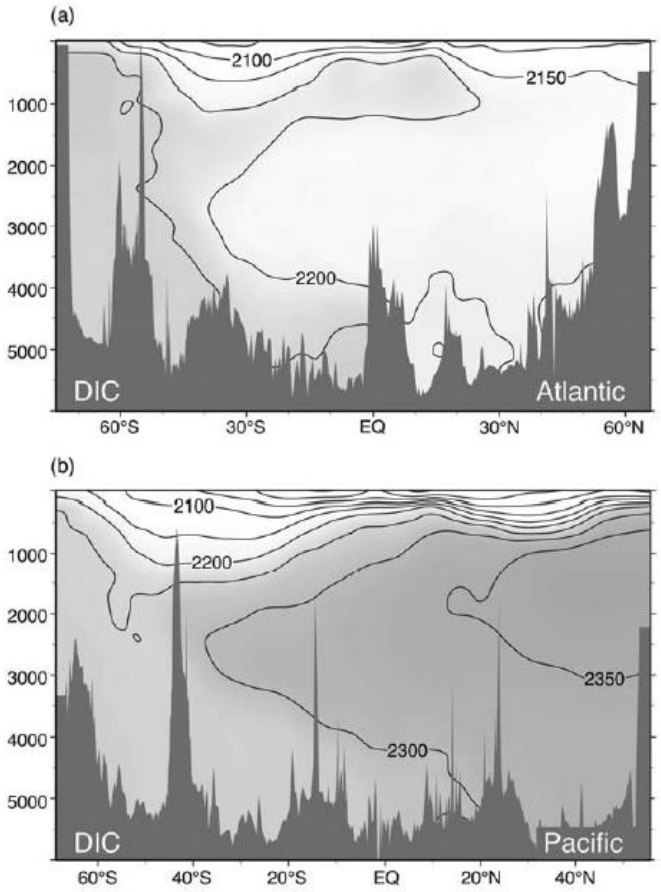

Figure 1.6. Observed meridional sections of DIC in (a) the Atlantic, along 20°W transect, and (b) the Pacific, along 170°W transect. Figure from Williams and Follows (2011).

In the surface open ocean, the distribution of DIC is also subjected to various physical and biogeochemical processes (see Section 1.5 for more details). The observed global surface ocean DIC pattern is suggested to be more similar to nutrients (Key et al., 2004), with its highest values at high latitudes, and reaching its lowest values at low latitudes.

Of particular interest is the distribution of surface DIC in the Southern Ocean, where intense upwelling takes place and the circulation connects ocean basins, linking the deep and shallow layers of the ocean. The uniqueness of the Southern Ocean makes it prominent in the exchange of carbon between the atmosphere and the ocean. Significant changes in pCO_2, TA, and DIC compared to other ocean areas are found in this region by previous studies (e.g., Fry et al., 2015; Takahashi et al., 2009 & 2014).

The changes in the ability of the Southern Ocean to take up CO_2 is also particularly important for the global carbon cycle: the Southern Ocean carbon sink was reported to be "saturated" from the 1980s to the 2000s (Le Quéré et al., 2007; Lovenduski et al., 2008), and then followed by a "reinvigoration" between 2002 and 2011 (DeVries et al., 2017; Landschützer et al., 2015). With the longer and more complete observations and new approaches, such as the biogeochemical Argo floats released into the Southern Ocean by SOCCOM project (Johnson et al., 2017), there is a new challenge view of the Southern Ocean carbon cycle that the high-latitude Southern Ocean (especially in the Antarctic Southern Zone) is actually releasing much more CO_2 to the atmosphere than previous ship-based estimates (Gray et al., 2018). The following chapter (Chapter 5) will address this issue in further detail.

1.4.2 Temporal variability

On short-term time scales (e.g., diurnal to intra-seasonal), the surface ocean carbonate system is usually modulated by bio-physical interactions (discussed later in Section 1.5). The diurnal change in surface DIC is usually fairly small in the oligotrophic ocean (e.g., Bates et al., 1998b), but can be larger in regions with higher biological productivity (Lefèvre et al., 2008; Yates et al., 2007). Episodic events such as tropical cyclones, storms, and blooms can have significant short-term impacts on the carbonate system and DIC in the surface ocean (Bates et al., 1998a; Evans et al., 2015; Fujii and Yamanaka, 2008).

Seasonal variability

Sustained observations in the subtropical and temperate regions (such as the Bermuda Atlantic Time-series Study (BATS, Bates et al., 2012), the Hawaii Ocean Time-series (HOT, Dore et al., 2009; Keeling et al., 2004), and the European Station for Time Series in the Ocean near the Canary Island (ESTOC, González-Dávila et al., 2010)) provide great opportunities to understand the seasonal variation of DIC in the open ocean.

Surface DIC is usually higher during winter due to the greater upward mixing or entrainment of high-CO_2 subsurface waters, and lower during summer due to biological CO_2 utilization (Bates et al., 2014; Takahashi et al., 2014). Almost all the time series observations revealed considerable seasonal variability of DIC in the surface water, ranging from less than 10 µmol kg^{-1} to over 60 µmol kg^{-1}. The seasonality seems to increase upon moving polewards. For instance, the seasonal amplitude of surface salinity-normalized DIC (which excludes the effect of salinity variation) is ~20 µmol kg^{-1} in the subtropical Pacific Ocean (Keeling et al., 2004), and ~40 µmol kg^{-1} in the subtropical Atlantic Ocean (Bates et al., 1996), while it increases to ~113 µmol kg^{-1} in the

northwestern Pacific Ocean (Kawakami et al., 2007) and ~60 µmol kg^{-1} in the subarctic northeast Pacific Ocean (Wong et al., 2002), to be discussed further in Section 3.2.4.

Interannual to decadal variability

Interannual changes in seawater carbonate chemistry can be caused by natural variations of the carbon cycle imparted by climate modes of variability, and by variability of deep, intermediate, and mode water formation (Bates, 2012; Gruber et al., 2002), perhaps influenced by the El Nino-Southern Oscillation (ENSO), the North Atlantic Oscillation (NAO), and the Pacific Decadal Oscillation (PDO).

Over multidecadal time scales, the observations indicate a similar rate of increase between the surface seawater CO_2 and atmospheric CO_2 (Takahashi et al., 2014): an increase in DIC of about 11 µmol kg^{-1} $decade^{-1}$ in response to an increase in atmospheric CO_2 of 19 µatm $decade^{-1}$. Figure 1.6 summarizes previous studies of the long-term trends in surface nDIC at seven time-series sites over the global ocean (Bates et al., 2014); the surface DIC increases by 0.6 to 1.8 µmol kg^{-1} yr^{-1} in the Atlantic and Pacific oceans, and nDIC has a slightly higher rate of 0.8 to 1.9 µmol kg^{-1} yr^{-1}, representing a 1.5% to 2.5% increase over the last three decades due to the continuous oceanic uptake of anthropogenic CO_2. Other evidence such as trends in the Revelle Factor also revealed a reduced buffering capacity of global surface water (Bates et al., 2014).

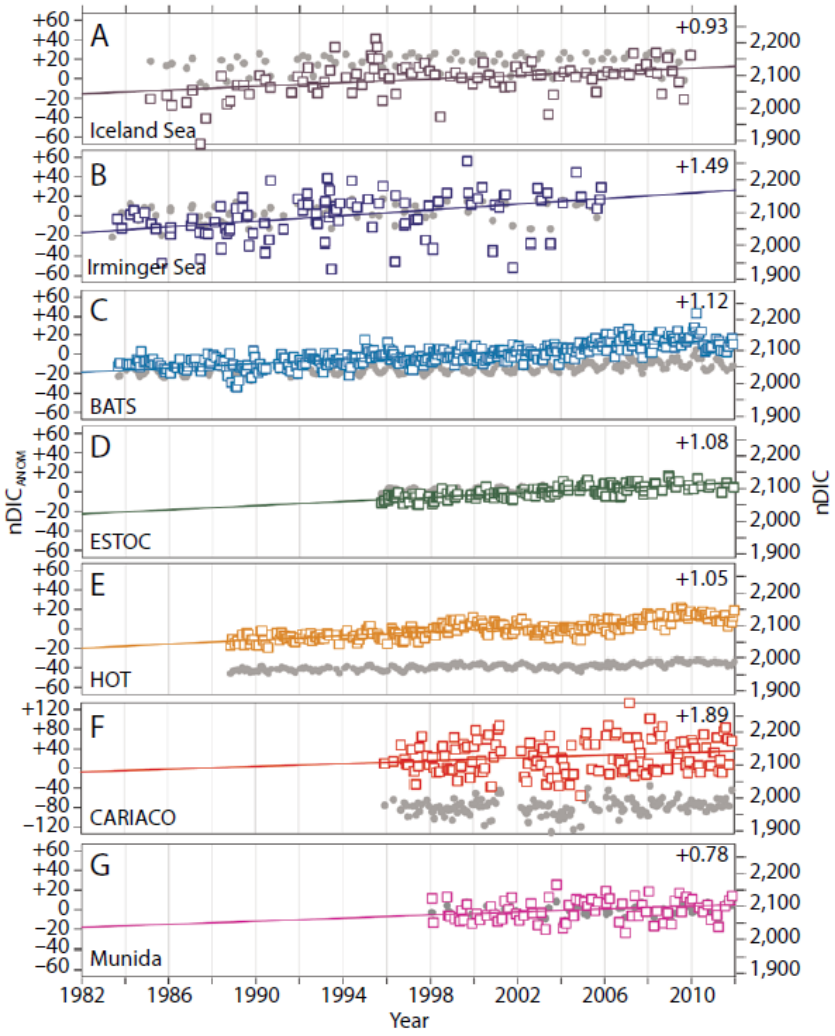

Figure 1.7. Time series of surface seawater anomalies of salinity-normalized DIC (nDIC, coloured symbols) and observed nDIC (grey symbols, µmol kg^{-1}). Trends (µmol kg^{-1} yr^{-1}) are shown in top right-hand corner of each panel. Figure from Bates et al. (2014).

1.5 Controls of DIC in the surface ocean

The marine carbonate system variables within the water column are controlled by a combination of physical, biological and chemical processes (Fig. 1.8), such as physical mixing, air-sea CO_2 exchange, photosynthesis and respiration, formation and dissolution of $CaCO_3$, and external sources (e.g., riverine inputs). The following text will describe the influences of the main processes on the marine carbonate system, especially DIC.

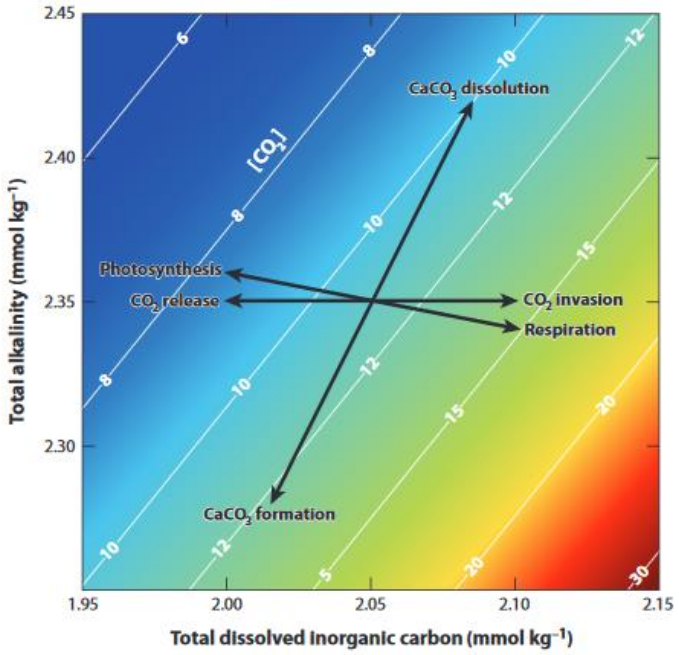

Figure 1.8. Schematic showing the impacts of different processes on the marine carbonate system. The white lines refer to the concentration of aqueous CO_2. CO_2 release/invasion (mainly through air-sea CO_2 gas exchange) only alters DIC; photosynthesis and respiration change DIC and TA in a ratio of -106:17; the formation and dissolution of $CaCO_3$ change DIC and TA in a ratio of 1:2. Figure from Zeebe (2012).

Physical mixing affects the carbonate system through the mixture of different water parcels with different properties. Since DIC and TA are both measured in gravimetric units (mol kg^{-1}), they are conservative with respect to mixing, as opposed to pH or pCO_2 which are affected by changes in pressure or temperature. For a pure physical mixing with no biogeochemical processes taking place, the amount of DIC or TA after mixing events is equal to the weighted sum of those in the contributing individual initial water parcels. One unique example of physical mixing is precipitation (dilution through addition of freshwater) and evaporation (concentration through removal of freshwater). The effects of precipitation and evaporation are most significant in the subtropical and tropical regions. Conservative mixing results in a proportional change in DIC and TA depending on the amounts of water added or removed and the concentrations of DIC and TA in those waters (Postma, 1964). Therefore, DIC and TA at different salinities (an indicator of precipitation and evaporation) are usually normalized to a reference salinity to account for the effects of freshwater input/removal (see more details in Chapter 2).

Air-sea CO_2 gas exchange occurs when there is a difference between sea surface pCO_2 ($pCO_{2,sea}$) and atmospheric pCO_2 ($pCO_{2,atm}$). The ocean absorbs CO_2 from the atmosphere if $pCO_{2,sea}$ is lower than $pCO_{2,atm}$, and releases CO_2 to the atmosphere in the opposite scenario. The air-sea CO_2 exchange only changes DIC, with no influence on TA because the charge balance is not affected

during the reaction of CO_2 with seawater (CO_2 molecules are not charged; Zeebe and Wolf-Gladrow, 2001).

Photosynthesis and respiration have a larger impact on DIC than TA, with a ratio of -106:17 (Redfield, 1963; Wolf-Gladrow et al., 2007), as shown in Fig. 1.8. The biological production and dissolution of $CaCO_3$ affects DIC and TA in a ratio of 1:2, following the reaction below (the dissolution of $CaCO_3$ has the opposite effects):

$$Ca^{2+} + 2HCO_3^- \overset{CaCO_3 \text{ precipitation}}{\Longleftrightarrow} CaCO_3 + CO_2 + H_2O \quad (1.9)$$

In contrast to the previous studies, Williams and Follows (2011) presented a new perspective: DIC in the surface ocean at equilibrium with a given atmospheric pCO_2 is controlled by two principle factors: (1) the temperature, and (2) the alkalinity of the surface water. As shown in Fig. 1.9, when in equilibrium with a fixed atmospheric pCO_2, DIC in the surface water is highly related to temperature and TA.

Temperature is suggested to play an important role on DIC because the solubility of all soluble gases increases with decreasing temperature. For instance, decreasing the water temperature enhances the solubility of CO_2, pushes Eq. 1.1 to the right, thus decreasing pCO_2 and driving more CO_2 into the surface ocean. Therefore, cooler waters tend to hold more DIC, and vice versa. Total alkalinity is also believed to be an important factor affecting DIC because: (1) both DIC and TA are largely composed of bicarbonate ions, which means that the concentration of DIC normally scales more or less linearly with TA; (2) in order to keep equilibrium with atmospheric pCO_2, DIC and TA of the water parcel have to change simultaneously (Humphreys et al., 2018) according to the vector diagram of DIC and TA (Fig. 1.8).

As a consequence, the surface DIC (Fig. 1.9) follows the temperature-dependent trend in the extra-tropics where surface waters are cooler and have lower TA; in contrast, surface DIC follows the alkalinity-dependent trend in the tropics and subtropics where waters are warmer and have higher TA (also see the discussion in Chapter 3).

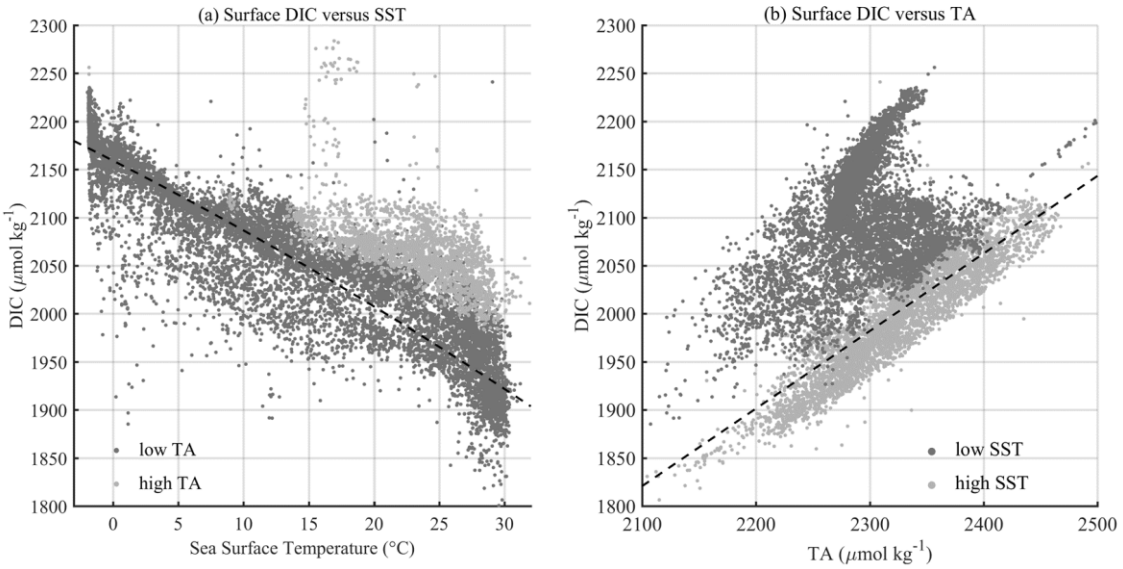

Figure 1.9. Relationships between DIC, Sea Surface Temperature (SST), and TA, over the global surface ocean (0-25 m). (a) DIC vs. SST separated into low alkalinity (dark grey, TA<2350 µmol kg^{-1}) and high alkalinity (light grey, TA>2350 µmol kg^{-1}); and (b) DIC vs. TA separated into cold waters (dark grey, SST<20°C) and warm waters (light grey, SST>20°C). The black dashed lines in (a) and (b) refer to the theoretical equilibrium DIC calculated under pCO_2 = 370 µatm (the average value of surface atmosphere in the 1990s) as a function of SST (with fixed TA of 2280 µmol kg^{-1}) or TA (with fixed SST of 25 °C). Data from Key et al. (2015). Figure redrawn from Williams and Follows (2011), based on a larger dataset – GLODAPv2.

1.6 Aims and objectives

Since the production of large observational datasets, a lot of effort has been put into studying the vertical and horizontal distributions of DIC in the global open ocean (e.g., Cameron et al., 2005; Gruber and Sarmiento, 2002; Key et al., 2004; Lee et al., 2000; Takahashi et al., 2014). However, regarding the latitudinal distribution of surface DIC there are still knowledge gaps regarding the key processes driving the DIC latitudinal gradient. This is also true for another important dissolved gas in seawater, dissolved O_2. O_2 is strongly related to the carbon cycle through biological activities. There is also a lack of studies investigating the coupled variations of CO_2 and O_2 on the global scale.

Therefore, the main objectives of this thesis are:

1. To understand the latitudinal distribution of the surface ocean DIC concentration and the drivers of it. Of particular interest are the tendencies of temperature and upwelling to raise high-latitude surface DIC (Chapter 3). This includes (1) to test different hypotheses as to the drivers of the observed latitudinal gradient in surface nDIC; (2) to understand

the importance of high-latitude upwelling in shaping the global open ocean surface DIC pattern; and (3) to compare the DIC distribution to those of other parameters such as alkalinity and nutrients.

2. To understand the relationship between the dissolved gases O_2 and CO_2 in the global surface ocean. More specifically, to investigate the nature of, and the factors producing, both coupled and uncoupled deviations of O_2 and CO_2 from gas exchange equilibrium with the atmosphere (Chapter 4). This includes (1) to develop a technique which is capable of investigating the coupled deviations of O_2 and CO_2 from their equilibrium values; (2) to identify the key controlling factors of the main deviations of O_2 and CO_2.
3. To examine the recent claim (Gray et al., 2018) that the Southern Ocean is releasing large amounts of CO_2 to the atmosphere in winter, mainly due to the upwelling of carbon-rich deep waters (Chapter 5). This includes (1) to quantify the impact of upwelling on elevating sea surface pCO_2; (2) to investigate the coupled variations of float-derived dissolved O_2 and CO_2 data using technique created in Chapter 4; and (3) to examine the validity of float-measured data.

1.7 Structure of thesis

Chapter 2: Methodology

This chapter describes the methodology used in this thesis, including the global dataset I used and the main techniques for data processing and analysis.

Chapter 3: What drives the latitudinal gradient in open ocean surface DIC concentration

This chapter focuses on the most important processes driving the surface DIC latitudinal distribution, using the GLODAPv2 database. I evaluated three main hypotheses (sea surface temperature-driven effect, salinity-related TA-driven effect, and high-latitude upwelling-driven effect) as to the principal drivers of the increase in surface DIC and salinity-normalized DIC from low to high latitude.

Chapter 4: Coupled deviations from gas exchange equilibrium of carbon dioxide and oxygen in the global surface ocean

This chapter investigates simultaneous changes in dissolved O_2 and CO_2 concentrations and develops a new technique – CORS – to identify regions and periods where processes are driving O_2 and CO_2 away from their equilibrium with the atmosphere.

Chapter 5: Carbon balance in the Drake Passage and the application of CORS

This chapter looks to test the claim of large winter emissions of CO_2 to the atmosphere suggested by the SOCCOM float data. The CORS technique is also used to investigate the changes in float-derived dissolved O_2 and CO_2 data, as well as to provide suggestions for the validity of float-measured data.

Chapter 6: Conclusion and Discussion

This chapter contains synthesis, bringing together the work presented in the individual chapters, and discusses the future implications of the major findings of this PhD project.

Chapter 2 Methodology

This chapter only introduces the databases and the common methods I used in the thesis. The specific methods and calculations involved with the individual study will appear in the following chapters.

2.1 Datasets used in this thesis

2.1.1 GLODAPv2

The Global Ocean Data Analysis Project version 2 database (GLODAPv2, Key et al., 2015; Olsen et al., 2016) was mainly used for the studies in Chapter 3 and 4. GLODAPv2 includes data in the original GLODAP (Key et al., 2004) database, CARINA and PACIFICA, as well as data from 168 new cruises. This compilation contains data from 724 cruises conducted from 1972 to 2013 (Fig. 2.1), with about one third collected since 2003. The GLODAPv2 database was not just a simple merging of the above products, but also an updated, unified, bias-corrected interior ocean data product with the following characteristics (Olsen et al., 2016):

- synthesis of previous data product such as GLODAPv1.1, CARINA, PACIFICA, and any new data;
- the core variables data (e.g., salinity, oxygen, DIC, TA, etc.,) have been calibrated and bias-corrected;
- preserve actual variability and trends;
- contain interpolated values for the missing data whenever possible;
- contain calculated values for the third seawater carbonate system variable.

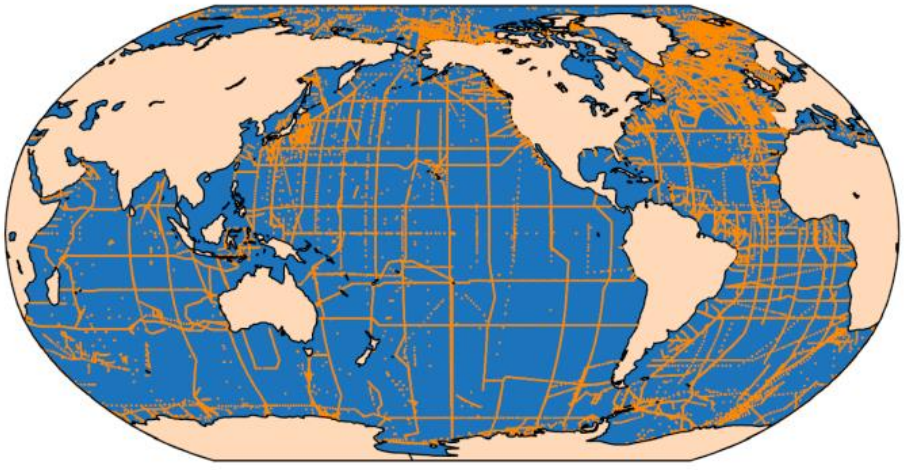

Figure 2.1. GLODAPv2 station locations. Figure from Key et al. (2015).

The data have undergone primary quality control and secondary quality control (with the most important tool being the crossover analysis, Fig. 2.2; Tanhua et al., 2010), and have been adjusted for consistency (Lauvset and Tanhua, 2015). Data with primary quality control flag of '0' and '2' (Table 2.1) were used for studies in this thesis (please refer to Olsen et al. (2016) for the specific adjustment for each parameter). For the parameters interested in this thesis, the compiled and adjusted data product is reported to be consistent to better than 1% in oxygen, 4 µmol kg^{-1} in DIC, 6 µmol kg^{-1} in TA (see Olsen et al. (2016) for more details).

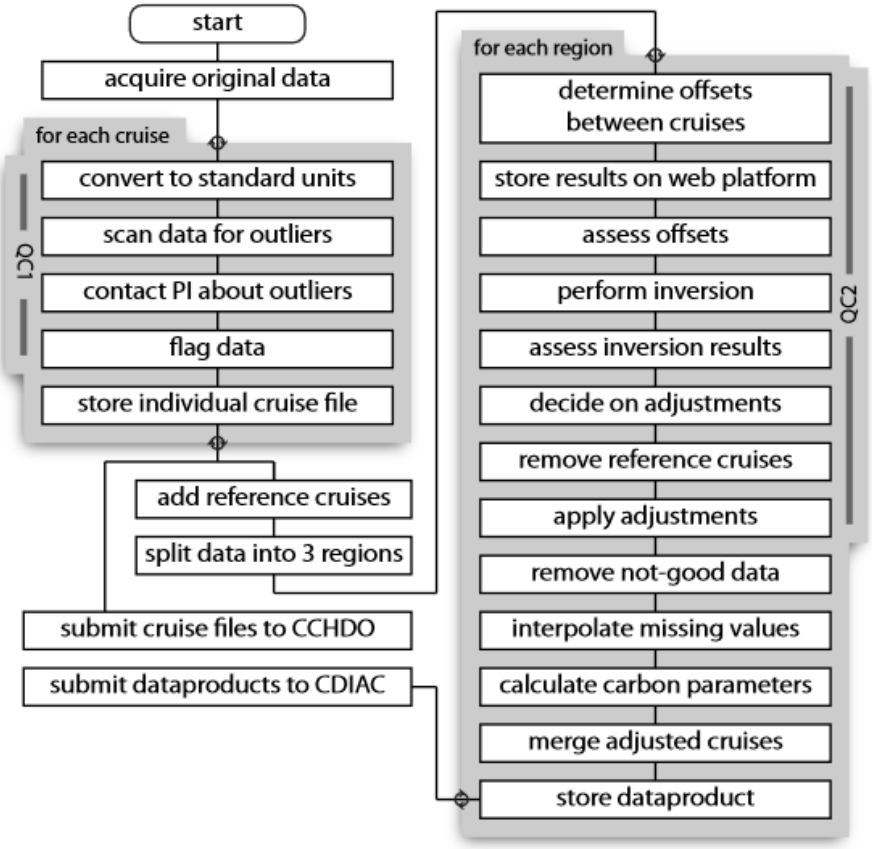

Figure 2.2. Flowchart showing the steps during the secondary quality control. Figure from Tanhua et al. (2010).

Table 2.1. Flags used in GLODAPv2. Table adapted from Olsen et al. (2016).

Flag value*	Interpretation
0	Interpolated or calculated value
2	Acceptable
3	Questionable (not included in product)
4	Bad (not included in product)
5	Value not reported
6	Not used
9	Not measured

* based on WOCE flags

2.1.2 SOCCOM

The Southern Ocean Carbon and Climate Observations and Modelling project (SOCCOM, https://soccom.princeton.edu/) is a multi-institutional program focused on investigating the complex Southern Ocean system; this dataset was used for studies in Chapter 5. This project has so far deployed over 150 floats equipped with biogeochemical sensors in the Southern Ocean. Most of the SOCCOM floats are Autonomous Profiling Explorers (APEX) floats assembled at the University of Washington from components purchased from Teledyne/Webb Research (Johnson et al., 2017). The deployed float follows a standard Argo mission with a profile at 10-day interval. The floats park at 1000 m between profiles, and then descend to depth between 1400 m and 2000 m before returning to the surface. Measurements are made on their ascents and data are transmitted via the Iridium satellite network at the ocean surface (surface time less than 15 min) before the floats descend back. The parameters measured include oxygen (by Aanderaa oxygen sensor), nitrate (by ISUS optical nitrate sensor), pH (by Deep-Sea DuraFET pH sensor), chlorophyll fluorescence (by WET Labs), and optical backscatter. Quality-controlled and adjusted data is available from floats that have been in the water at least 6 months (Johnson et al., 2017).

The carbonate system data from SOCCOM biogeochemical floats were calculated by SOCCOM researches from the measured in situ pH and an algorithm-based estimate for TA. The calibration and correction of the pH sensor is described in Williams et al. (2016), by comparing the sensor-measured pH value to the nearest available ship-collected data from GLODAPv2 at 1500 m depth. The measured pH is stated to have an uncertainty of 0.005 (Johnson et al., 2017). TA was

estimated using a Multiple Linear Regression (MLR; Williams et al., 2017)-derived algorithm or a Locally Interpolated Alkalinity Regression (LIAR; Carter et al., 2018)-derived algorithm based on measured temperature, salinity, pressure, oxygen and also location. The standard uncertainty in the estimated TA is stated to be 4.3 and 5 μmol kg^{-1}, respectively (Williams et al., 2017; Williams et al., 2018). The pCO_2 value calculated from measured pH and estimated TA thus has an uncertainty of 2.7% (Williams et al., 2017). The quality-controlled files can be obtained at ftp://ftp.mbari.org/pub/SOCCOM/FloatVizData/QC. More details about the SOCCOM dataset are introduced in Chapter 5.

2.2 Data processing

2.2.1 Normalization of DIC to a reference year

To prevent temporal DIC trends (anthropogenic CO_2 accumulation) from generating artificial spatial variability, I normalized surface DIC to a reference year of 2005, by assuming that surface seawater pCO_2 tracks atmospheric pCO_2 (Feely, 2008; see also "CO_2 Time Series in the North Pacific" at https://pmel.noaa.gov/co2/file/CO2+time+series). I first calculated the change in atmospheric mole fraction of CO_2 ($xCO_{2,air}$) compared to the reference year 2005:

$$\Delta xCO_{2,air} = xCO^{t}_{2,air} - xCO^{2005}_{2,air} \quad (2.1)$$

where the superscript "t" and "2005" refer to year, and the globally averaged atmospheric xCO_2 data can be found at https://www.esrl.noaa.gov/gmd/ccgg/trends/ (neither spatial nor seasonal variability in atmospheric CO_2 is considered).

Then I converted $\Delta xCO_{2,air}$ into $\Delta pCO_{2,air}$ (Takahashi et al., 2009) just above the sea surface, using calculated humidity data. It is then assumed that $\Delta pCO_{2,sw}$, representing the change of sea surface pCO_2 relative to the year 2005, is equal to $\Delta pCO_{2,air}$.

Therefore the sea surface pCO_2 normalized to year 2005 was calculated as:

$$pCO^{2005}_{2,sw} = pCO^{t}_{2,sw} - \Delta pCO_{2,sw} \quad (2.2)$$

where $pCO^{t}_{2,sw}$ was calculated from in-situ DIC, TA, temperature and salinity using CO_2SYS v1.1 (Van Heuven et al., 2011).

Since the anthropogenic CO_2 perturbation does not change TA, DIC normalized to the year 2005 was calculated with inputs of in-situ TA and $pCO^{2005}_{2,sw}$ using CO_2SYS (Van Heuven et al., 2011):

$$DIC^{2005} = f\,(T_{in\text{-}situ},\ S_{in\text{-}situ},\ TA_{in\text{-}situ},\ pCO^{2005}_{2,sw}) \quad (2.3)$$

2.2.2 Salinity normalization

Salinity normalization was used to correct for the influence of precipitation and evaporation in the open ocean (Postma, 1964) for Chapter 3. Data were normalized to a reference salinity of 35 using a standard procedure:

$$nX = X_{obs} \times 35/S_{obs} \quad (2.4)$$

where nX refers to the normalized variable, X_{obs} is the observed value of the variable, and S_{obs} is the observed salinity.

I acknowledge that this approach (Eq. 2.4) can create artificial variance in DIC distribution (Friis et al., 2003) because it ignores the influences of riverine input and upwelling from below the lysocline. I avoided the riverine problem partly by excluding the affected regions (Section 3.2.1).

In terms of the former concern (riverine input), I calculated the likely impact on the results. Fig. 2.2 shows the relationship between surface DIC and salinity based on the GLODAPv2 dataset. I selected data between 30°S and 30°N (i.e., the oligotrophic surface oceans) in order to avoid the perturbations of upwelling (discussed later) and biological activities on surface DIC. By fitting surface DIC against salinity, a 'non-zero intercept' was found for each of the ocean basins (Fig. 2.2), ranging from -187 µmol kg^{-1} (Pacific Ocean) to 262 µmol kg^{-1} (Atlantic). By substituting the values into the Equation (Friis et al., 2003)

$$nDIC = \frac{DIC^{meas} - DIC^{S=0}}{S^{meas}} \cdot S^{ref} + DIC^{S=0} \quad (2.5)$$

where subscript 'meas' refers to 'measured', S^{ref} equates 35.

Eq. 2.5 can be further rearranged into

$$nDIC = \frac{DIC^{meas}}{S^{meas}} \cdot S^{ref} + DIC^{S=0} \cdot \left(1 - \frac{S^{ref}}{S^{meas}}\right) \quad (2.6)$$

I found that the discrepancy (i.e., the term $DIC^{S=0} \cdot \left(1 - \frac{S^{ref}}{S^{meas}}\right)$) between the Friis et al. (2013) method and our calculation (Eq. 2.4) only accounts for a difference ranging from -5 µmol kg^{-1} to 7 µmol kg^{-1}, which is of similar magnitude to the uncertainty in DIC measurement and also much smaller than the DIC latitudinal difference (about 200 µmol kg^{-1}, see Section 3.3).

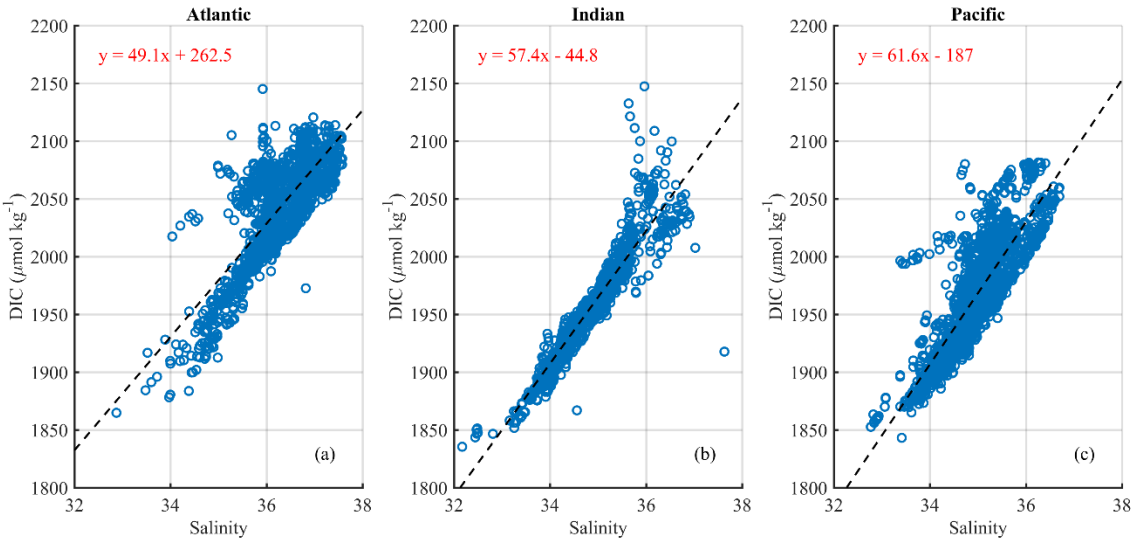

Figure 2.3. Relationship between sea surface DIC and salinity in the Atlantic, Indian, and Pacific oceans between 30°S and 30°N in each ocean. The black dashed lines are best-fit linear regression lines.

In terms of the latter concern (upwelling), I took the Southern Ocean for instance where the largest upwelling in the world takes place. The magnitude of the discrepancy term ($DIC^{S=0} \cdot (1-\frac{S^{ref}}{S^{meas}})$) depends on $DIC^{S=0}$ and S_{meas}. $DIC^{S=0}$ refers to the region-specific term of S=0 due to upwelling of deep water which accumulates remineralized inorganic carbon. Based on the GLODAPv2 database, the average concentration of DIC at depths greater than 500 m (the largest mixed layer depth in winter in the Southern Ocean, Dong et al., 2008) in the Southern Ocean (south of 40°S) is 2250 μmol kg^{-1}, and the average concentration of DIC in the surface layer (shallower than 30 m) in the Southern Ocean is 2130 μmol kg^{-1}. As a consequence, upwelling from below the lysocline can create the largest DIC difference of 120 μmol kg^{-1}. Therefore, the discrepancy term ($DIC^{S=0} \cdot (1-\frac{S^{ref}}{S^{meas}})$) is always relatively small, given that the average measured salinity in the surface Southern Ocean is 34 and the reference salinity is 35, resulting in a ratio very close to 1.

To conclude, the 'non-zero intercept' of DIC vs. salinity relationships in different ocean basins has negligible influence on salinity normalization of DIC, accounting for at most 7 μmol kg^{-1} change in DIC; upwelling from below the thermocline also has negligible influence, accounting for at most 4 μmol kg^{-1} change in DIC. These are small compared to the DIC latitudinal gradient of about 200 μmol kg^{-1} that I investigate in Chapter 3.

2.2.3 Carbonate system calculations

Given that the marine carbonate system can be calculated from any two of the four fundamental parameters, i.e., DIC, TA, pH and pCO_2 (Zeebe and Wolf-Gladrow, 2001), the MATLAB version of CO_2SYS (version 1.1, Van Heuven et al., 2011) was used for the carbonate system calculations. The dissociation constants for carbonic acid and bisulfate were taken from Lueker et al. (2000) and Dickson (1990) respectively, and the total borate-salinity relationship was taken from Lee et al. (2010).

2.2.4 Calculation of ΔO_2 and ΔCO_2

The concentrations of $\Delta[O_2]$ and $\Delta[CO_2]$ are calculated to represent the deviations of O_2 and CO_2 from their saturations with respect to the atmosphere (used in Chapter 4 and Chapter 5):

$$\Delta[O_2] = \left[O_{2,obs}\right] - [O_{2,sat}] \quad (2.7)$$

$$\Delta[CO_2] = \left[CO_{2,obs}\right] - [CO_{2,sat}] \quad (2.8)$$

where the subscript 'obs' indicates the observed concentration, and 'sat' indicates the saturation concentration in equilibrium with the atmosphere, respectively.

The saturation concentration for O_2 was calculated using the equation introduced by Garcia and Gordon (1992) and Garcia and Gordon (1993) for the solubility of O_2. In order to account for the impacts of bubble injection and the thermal skin effect on O_2 saturation in the surface ocean, I applied a saturation anomaly of 0.75% (Sarmiento and Gruber, 2006) to O_2 saturation (i.e., the saturation of O_2 in the surface ocean is 100.75% the traditionally-calculated value).

The observed CO_2 concentration was calculated using CO_2SYS (Van Heuven et al., 2011) from in-situ temperature, salinity, dissolved inorganic carbon (DIC), total alkalinity (TA), phosphate, and silicate concentration in the GLODAPv2 database; the dissociation constants for carbonic acid and sulfate were from Lueker et al. (2000) and Dickson (1990), respectively, and the total borate-salinity relationship from Lee et al. (2010).

The saturation concentration for CO_2 was calculated using Henry's Law

$$[CO_2] = K_H \times pCO_{2,eq} \quad (2.9)$$

where the solubility constant (K_H) of CO_2 was calculated following Weiss (1974). $pCO_{2,eq}$ refers to the value in equilibrium with atmospheric CO_2, which was calculated as

$$pCO_{2,eq} = xCO_{2,air} \times (P_{baro} - P_{sw}) \quad (2.10)$$

The value of $xCO_{2,air}$ increases year after year; I used the global annual mean atmospheric xCO_2 for the year of measurement from NOAA/ESRL/Global Monitoring Division (ftp://ftp.cmdl.noaa.gov/ccg/co2/trends/co2_annmean_gl.txt). For P_{baro}, I used 101,325 Pa, which is the long-term average value of the barometric pressure at the sea surface (https://www.esrl.noaa.gov/psd/data/gridded/data.ncep.reanalysis.derived.surface.html). P_{sw} (water vapor pressure) was calculated from in-situ temperature and salinity of surface water (Weiss and Price, 1980).

Chapter 3 What drives the latitudinal gradient in open-ocean surface dissolved inorganic carbon concentration?

This chapter is published as Wu, Y., Hain, M. P., Humphreys, M. P., Hartman, S., and Tyrrell, T.: What drives the latitudinal gradient in open-ocean surface dissolved inorganic carbon concentration?, Biogeosciences, 16, 2661–2681, https://doi.org/10.5194/bg-16-2661-2019, 2019.

Abstract

Previous work has not led to a clear understanding of the causes of spatial pattern in global surface ocean dissolved inorganic carbon (DIC), which generally increases polewards. Here, I revisit this question by investigating the drivers of observed latitudinal gradients in surface salinity-normalized DIC (nDIC) using the Global Ocean Data Analysis Project version 2 (GLODAPv2) database. I used the database to test three different hypotheses for the driver producing the observed increase in surface nDIC from low to high latitudes. These are: (1) sea surface temperature, through its effect on the CO_2 system equilibrium constants, (2) salinity-related total alkalinity (TA), and (3) high-latitude upwelling of DIC- and TA-rich deep waters. I find that temperature and upwelling are the two major drivers. TA effects generally oppose the observed gradient, except where higher values are introduced in upwelled waters. Temperature-driven effects explain the majority of the surface nDIC latitudinal gradient (182 of the 223 µmol kg^{-1} increase from the tropics to the high-latitude Southern Ocean). Upwelling, which has not previously been considered as a major driver, additionally drives a substantial latitudinal gradient. Its immediate impact, prior to any induced air-sea CO_2 exchange, is to raise Southern Ocean nDIC by 220 µmol kg^{-1} above the average low-latitude value. However, this immediate effect is transitory. The long-term impact of upwelling (brought about by increasing TA), which would persist even if gas exchange were to return the surface ocean to the same CO_2 as without upwelling, is to increase nDIC by 74 µmol kg^{-1} above the low-latitude average.

3.1 Introduction

The ocean absorbs about one-quarter of the anthropogenic CO_2 emitted every year (Le Quéré et al., 2018). It is the largest non-geological carbon reservoir (~38000 Gt C; Falkowski et al., 2000), containing 50 times as much carbon as the pre-industrial atmosphere, and thereby modulates the Earth's climate system. Approximately 97% of the carbon in the ocean is in the form of dissolved inorganic carbon (DIC), which is the total concentration of aqueous CO_2 and bicarbonate and carbonate ions:

$$DIC = \left[CO_2^*\right] + [HCO_3^-] + [CO_3^{2-}] \quad (3.1)$$

where $[CO_2^*]$ refers to the sum of aqueous CO_2 and undissociated carbonic acid (H_2CO_3), with the latter being negligible (Zeebe and Wolf-Gladrow, 2001).

Understanding what controls the distribution of oceanic DIC is essential for quantifying anthropogenic CO_2 invasion (e.g., Gruber, 1998; Humphreys et al., 2016; Lee et al., 2003; Sabine et al., 1999; Sabine et al., 2002; Vázquez-Rodríguez et al., 2009) and consequent ocean acidification (e.g., Doney et al., 2009; Orr et al., 2005). As most marine organisms live in the sunlit surface ocean, where CO_2 exchange with the atmosphere happens, the controls on surface ocean DIC in particular merit investigation.

Many previous studies focused on the vertical, rather than latitudinal, distribution of DIC. They investigated the contributions of the different "carbon pumps" – solubility pump, soft tissue pump, and carbonate pump (Cameron et al., 2005; Gruber and Sarmiento, 2002; Toggweiler et al., 2003a; Toggweiler et al., 2003b) – to the pattern of DIC with depth. The solubility pump is based on the assumption that, at high latitudes where deep waters form, DIC is high because the low water temperature increases CO_2 solubility. Lee et al. (2000) used this principle to predict salinity-normalized DIC (nDIC) from empirical functions of sea surface temperature and nitrate that varied seasonally and geographically.

Key et al. (2004) depicted the global distribution of surface DIC using an earlier version (GLODAPv1) of the dataset than I used in this study, noting that the surface DIC pattern is more similar to nutrients (including the Southern Ocean, where both DIC and nutrients are enriched) than to salinity - unlike total alkalinity (TA), whose pattern more closely resembles that of salinity (Fry et al., 2015). Using the data from the new GLODAPv2 database (Key et al., 2015; Olsen et al., 2016), surface DIC is confirmed here to have its highest values at high latitudes, like nutrients, and to reach its lowest values at low latitudes in each basin (Fig. 3.1a). Earlier studies (Lee et al., 2000; Toggweiler et al., 2003a; Williams and Follows, 2011, Sect. 6.3 "What controls DIC in the surface

ocean?") suggested that temperature is of primary importance in regulating surface DIC (e.g., Lee et al., 2000; Toggweiler et al., 2003a; Williams and Follows, 2011; Humphreys, 2017). Under this assumption, surface waters in cool regions at high latitudes should hold more DIC than surface waters in the warm regions at low latitudes.

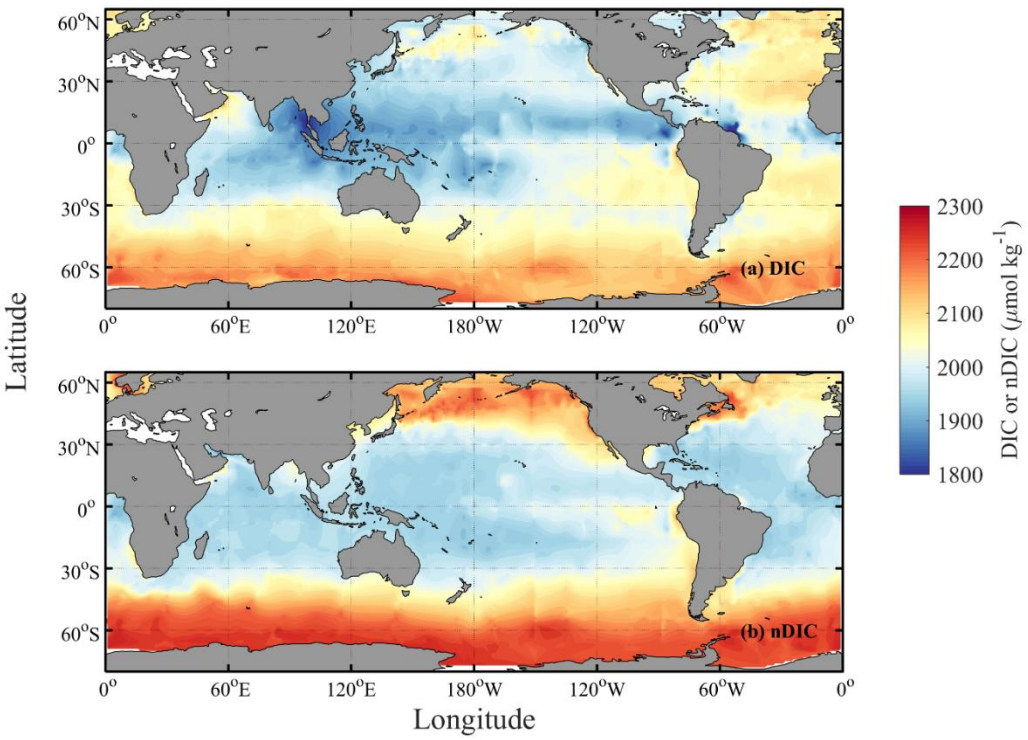

Figure 3.1. Spatial distributions of DIC and nDIC. (a) DIC (normalized to year 2005), (b) salinity-normalized DIC (nDIC, DIC normalized to reference year of 2005 and salinity of 35) in the surface global ocean. The latitudinal trends are clear, particularly for nDIC.

Williams and Follows (2011) argued that another variable also exerts control on the surface DIC distribution: TA sets the equilibrium capacity for seawater to hold DIC in solution (Humphreys et al., 2018; Omta et al., 2011), so higher surface TA values may lead to higher DIC. Takahashi et al. (2014) explored the seasonal distribution of climatological surface DIC using seawater pCO_2 from the Lamont Doherty Earth Observatory (LDEO) database and TA estimated from salinity, qualitatively attributing seasonal differences (on a regional scale) to the greater upward mixing of high-CO_2 deep waters in winter and summer biological carbon drawdown. They noted the potential for upwelling to alter surface DIC, but focused on DIC seasonality rather than its spatial variability. In recent years, the global surface DIC database has greatly expanded, culminating in GLODAPv2 (Key et al., 2015; Olsen et al., 2016), but the drivers of the global surface DIC distribution have not yet been reassessed.

The processes that influence the distribution of surface DIC at the local scale can be divided into those which change DIC by direct addition or removal, and those which affect DIC indirectly. The

direct processes include: (1) biological carbon assimilation during primary production and release during remineralization (Bozec et al., 2006; Clargo et al., 2015; Toggweiler et al., 2003b; Yasunaka et al., 2013); (2) transport of DIC-rich deep waters into the surface layer (Jiang et al., 2013; Lee et al., 2000); and (3) production and export of $CaCO_3$. Indirect processes include: (4) seawater dilution or concentration due to precipitation or evaporation (Friis et al., 2003); (5) warming and cooling, which alter CO_2 solubility and induce air-sea gas exchange that acts to reduce air-sea CO_2 disequilibrium (Bozec et al., 2006; Toggweiler et al., 2003a; Williams and Follows, 2011); and (6) the above processes (1-4) through their impact on TA - if high/low TA values are not matched by high/low DIC values then the resulting low/high seawater pCO_2 stimulates CO_2 ingassing/outgassing until DIC matches TA (Humphreys et al., 2018). The effects of equilibrium processes (the effects through temperature and upwelled TA) change the surface ocean DIC at which air-sea CO_2 equilibrium occurs, so these effects can persist beyond the air-sea CO_2 equilibrium timescale (months to a year; Jones et al., 2014). The effects of disequilibrium processes, such as direct DIC supply from upwelling, and biological uptake of DIC in response to upwelled nutrients (principally iron; Moore et al., 2016) can persist no longer than the CO_2 equilibrium timescale.

Our study builds on previous work in several ways. First, whereas many previous studies looked to understand the *vertical* DIC distribution, our target is to understand the *latitudinal* surface DIC distribution. Second, I identify the most important *processes*, not just the *variables*, driving the surface DIC distribution (Fig. 3.2). Third, I use a much larger observational global dataset – GLODAPv2.

I evaluate three main hypotheses as to which processes cause the increase in surface DIC and nDIC from low to high latitude (Fig. 3.1):

(1) latitudinal variation in solar heating via its effect on sea surface temperature, and hence CO_2 solubility;

(2) evaporation and precipitation, through their effects on TA; and

(3) upwelling and winter entrainment through the introduction of DIC- and TA-rich deep waters to the (sub)polar surface oceans, when coupled with iron limitation of biological uptake of DIC.

It is easier to constrain the dynamics of upwelling and quantify their impact on surface DIC in the Southern Ocean (where upwelling has been more comprehensively studied; e.g., Marshall and Speer, 2012; Morrison et al., 2015) than in the subarctic North Atlantic and North Pacific oceans (where upward transport occurs via deep mixing in the winter, combined with upwelling in the North Pacific). The Southern Ocean also plays a crucial role in the global overturning circulation

(e.g., Marshall and Speer, 2012), and the global carbon cycle (Landschützer et al., 2015; Mikaloff-Fletcher, 2015). Therefore, I focused on the Southern Ocean for the evaluation of the third hypothesis. A novel conclusion of this study is that upwelling, whose global significance has previously been overlooked, is very important in shaping the spatial distribution of surface ocean DIC, in part because upwelling of TA changes equilibrium DIC.

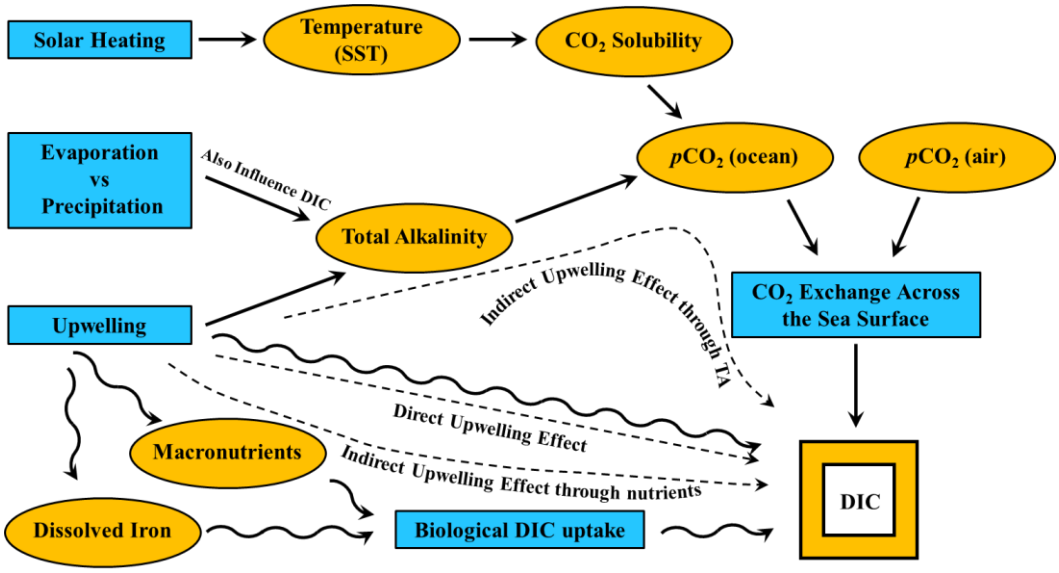

Figure 3.2. Major controls on surface DIC. Schematic showing the main processes exerting an influence over the concentration of DIC in the global surface ocean (producing variation with latitude). Blue shapes are processes and orange shapes are variables. Straight solid arrows represent equilibrium processes regulating DIC in the long term and wavy solid arrows represent disequilibrium processes regulating DIC in the short term. In this chapter, I evaluate the upwelling effect on surface DIC in the Southern Ocean. Dashed arrows with text denote the three different ways that upwelling affects DIC: the direct effect through upwelled DIC, the indirect effect through upwelled nutrients which stimulate biological removal of DIC, and the indirect effect through upwelled TA changing the equilibrium DIC with the atmosphere.

3.2 Methods

I used data from GLODAPv2 (Key et al., 2015; Olsen et al., 2016). This compilation contains data from over 700 cruises conducted from 1972 to 2013, with about a third collected since 2003. The data have undergone secondary quality control and have been adjusted for consistency (Key et al., 2015; Lauvset and Tanhua, 2015; Olsen et al., 2016). Table 3.1 summarizes the definitions of subscripts used in the following text.

Table 3.1. Definitions of subscripts and main terms used in the text. X represents any variable involved in the calculations. The program CO_2SYS was used to calculate values under different conditions.

Subscript	*Meaning*
	Referring to (n)DIC values at a particular location
X_{supply}	Value at depth, along isopycnals that upwell at this location
X_{surf}	Predicted value in the surface layer
X_{obs}	Observed value at this surface location
	Referring to predicted (n)DIC values under different conditions
$X_{SST=27}$	Predicted value with sea surface temperature changed to 27°C
X_{nonupw}	Predicted value with upwelled TA subtracted
	Referring to changes in (n)DIC values because of processes
ΔX_{Fe}	Effect of iron limitation (biological drawdown that is prevented)
ΔX_{temp}	Effect of sea surface temperature variations
ΔX_{upw_st}	Short-term effect of upwelling, through upwelled DIC
ΔX_{upw_lt}	Long-term effect of upwelling, through upwelled TA
	Carbonate variables used to calculate predicted DIC values with CO_2SYS
$DIC_{SST=27} = f(T_{SST=27}, S_{in\text{-}situ}, TA_{in\text{-}situ}, pCO_{2,in\text{-}situ})$	$DIC_{SST=27}$ is a function of in-situ S, TA, and pCO_2, and SST at 27°C
$DIC_{nonupw} = f(T_{in\text{-}situ}, S_{in\text{-}situ}, TA_{nonupw}, pCO_{2,in\text{-}situ})$	DIC_{nonupw} is a function of in-situ SST, S, and pCO_2, and pre-upwelling TA

3.2.1 Data processing

The "surface" ocean is defined as the uppermost 30 m at latitudes greater than 30°, and shallower than 20 m at latitudes less than 30° (following e.g., Fry et al., 2015; Lee et al., 2006). Only open-ocean data (water depth > 200 m) were included in this study (Fig. 3.3).

I excluded regions perturbed by river inputs in order to remove confounding factors affecting the latitudinal distributions of DIC and nDIC on smaller length scales than being investigated here. I excluded the Arctic Ocean (> 65° N) (Fig. 3.3) because it is heavily influenced by river inputs (Fry et al., 2015; Jiang et al., 2014); all data from the Mediterranean Sea and the Red Sea because of their

very high salinity (Jiang et al., 2014); and some data (those where S is less than 34) from other ocean areas: the Amazon River plume in the North Atlantic (5° N-10° N, > 45° W), the Ganges-Brahmaputra plume in the Bay of Bengal (> 5° N, 80-94° E) (both Fry et al., 2015) and the western North Atlantic margins (Cai et al., 2010). I also excluded low-latitude ocean areas affected by upwelling (i.e., the eastern equatorial Pacific and northern Californian upwelling regions).

The surface DIC was normalized to a reference year of 2005 according to Section 2.2.1. The salinity-normalization of DIC follows Section 2.2.2. For the carbonate system calculations, all the dissociation constants I used are summarized in Section 2.2.3.

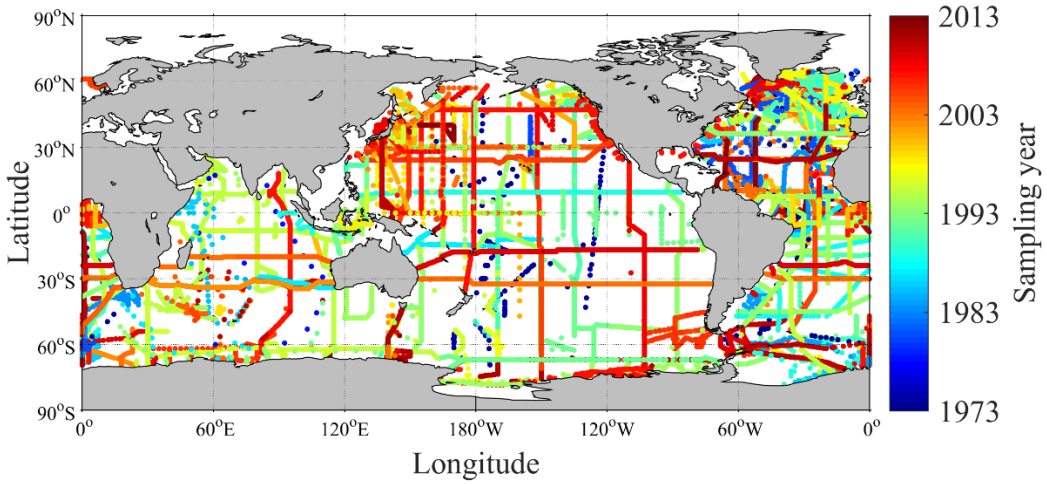

Figure 3.3. Spatial and temporal distribution of GLODAPv2 sampling stations used for this study.

3.2.2 Calculation of DIC and nDIC latitudinal gradients

The magnitude of the latitudinal gradient depends on the time of year. It is calculated because DIC values are higher in winter at high latitudes. The seasonal amplitude of surface nDIC varies over the global open ocean. It is generally small at low latitudes: ~20 µmol kg^{-1} in the subtropical Pacific Ocean (Keeling et al., 2004) and ~40 µmol kg^{-1} in the subtropical Atlantic Ocean (Bates et al., 1996). It is much larger at some (but not all) high-latitude locations: ~113 µmol kg^{-1} in the northwestern Pacific Ocean (Kawakami et al., 2007) and ~60 µmol kg^{-1} in the subarctic northeast Pacific Ocean (Wong et al., 2002), but only ~25 µmol kg^{-1} at the KERFIX site in the Southern Ocean (Louanchi et al., 2001; Louanchi et al., 1999). Because most ship-collected data (as contained in GLODAPv2) are collected in spring or summer months, the latitudinal gradients averaged across the whole year will be larger in some locations than presented here, and the magnitudes of the latitudinal gradients presented here should be considered lower estimates. For instance, the observed nDIC difference (ΔnDIC) between the North Pacific (40°N - 60°N) and low latitudes (30°S - 30°N) is 171 µmol kg^{-1} when calculated from summer data only and 224 µmol kg^{-1} when

calculated from winter data only. For the Southern Ocean, ΔnDIC is 214 μmol kg^{-1} in summer and 240 μmol kg^{-1} in winter. This sensitivity to time of year should be noted but is not considered further here because it is relatively small compared to the overall magnitude of ΔnDIC.

3.2.3 Calculations of the effects of various processes on DIC

The second hypothesis (evaporation and precipitation through their effects on TA) was evaluated by salinity normalization (Eq. 2.4). The methods for calculating the impacts of the other two processes on the surface DIC concentration are now explained. The effect of upwelling is evaluated in the Southern Ocean, from both short- and long-term perspectives. In addition, I also quantify the effect of iron limitation, which would potentially affect the observed (n)DIC distribution.

3.2.3.1 SST-driven effect

The temperature effect on the carbonate system has two aspects. First, when water temperature increases, the equilibria between carbonate species (Eq. 3.2) shift towards increasing the aqueous CO_2 and carbonate ion concentrations (Dickson and Millero, 1987):

$$CO_2 + H_2O + CO_3^{2-} \rightleftharpoons 2HCO_3^- \quad (3.2)$$

Second, CO_2 solubility is lower at higher temperatures and vice versa (Weiss, 1974). Neither effect alters DIC directly, but both change the seawater pCO_2. A larger proportion of DIC exists as aqueous CO_2 at higher temperatures and the ratio of pCO_2 to $[CO_2]$ also increases as solubility decreases (Eq. 1.6, Henry's law):

Both effects tend to increase sea surface pCO_2 as seawater warms, potentially increasing the net air-to-sea CO_2 flux; the induced outgassing of CO_2 reduces sea surface pCO_2 and DIC as it shifts the system towards CO_2 equilibrium. Therefore, for an open-ocean system in contact with the atmosphere, sea surface temperature (SST) can control the DIC distribution, and this can by itself produce DIC latitudinal variations.

To examine the magnitude of the expected temperature-induced DIC changes, I chose the low-latitude area as the reference, then removed the latitudinal SST variation and recalculated the open-ocean surface DIC everywhere for a constant SST of 27°C (the mean sea surface temperature in the subtropics from 30° S to 30° N). I first calculated the in-situ pCO_2 from observed SST, SSS (sea surface salinity), TA and DIC using CO_2SYS. The calculated pCO_2 from TA and DIC has been found to agree well with the measured pCO_2 by Takahashi et al. (2014) (root-mean-square deviation of ± 6.8 μatm). I then altered the sea surface temperature from its in-situ

value to 27°C, which would change the solubility of CO_2 and induce air-sea CO_2 gas exchange. Then air-sea CO_2 gas exchange (which does not change TA) was assumed to proceed until pCO_2 was back to the same level as before resetting the temperature. Next, I used CO_2SYS to calculate $DIC_{SST=27}$ based on an input temperature of 27°C, observed salinity and TA, and the in-situ pCO_2 calculated as above. $DIC_{SST=27}$ thus represents temperature-normalized DIC, and should exhibit the same spatial variability as DIC except that the temperature-induced component of the variability has been removed. Finally, the difference between observed DIC and $DIC_{SST=27}$ gives the DIC variation attributed to temperature variation:

$$\Delta DIC_{temp} = DIC_{obs} - DIC_{SST=27} \quad (3.3)$$

The same procedure was followed for calculating $\Delta nDIC_{temp}$:

$$\Delta nDIC_{temp} = nDIC_{obs} - nDIC_{SST=27} \quad (3.4)$$

3.2.3.2 Upwelled DIC-driven effect (short-term effect of upwelling)

Upwelling of DIC-rich subsurface waters can increase the surface DIC. The largest upwelling flux anywhere in the world takes place in the Southern Ocean (Talley, 2013): the upwelling there is made up of 18 Sv (Sverdrup, 1 Sv = 10^6 m^3/s) of NADW (North Atlantic Deep Water), 11 Sv of IDW (Indian Deep Water), and 9 Sv of PDW (Pacific Deep Water). Subsurface waters in the Southern Ocean upwell along the neutral density isopycnals of 27.6 kg m^{-3}, 27.9 kg m^{-3} and 27.9 kg m^{-3} in the southern Atlantic, Indian, and Pacific oceans, respectively (Ferrari et al., 2014; Lumpkin and Speer, 2007; Marshall and Speer, 2012; Talley, 2013).

Upwelling occurs within the Antarctic Circumpolar Current (ACC) where the wind stress is greatest (Morrison et al., 2015). As the upwelled water subsequently advects away, the effects of upwelling on DIC are transported to nearby locations. Therefore, instead of a direct supply from deep to surface locations such as L3 (Fig. 3.4), DIC is brought to the subsurface primarily along isopycnals (shown in Fig. 3.4 as the black curve to L1), finally reaching the surface at L2. Then, the upwelled waters with enriched DIC, TA and nutrients feed both branches of the Southern Ocean overturning circulation. One branch is transported northwards via Ekman transport from L2 to L3, as shown by the black arrow towards the Equator, and the other is recycled to form Antarctic Bottom Water (AABW) (Talley, 2013). The effect of upwelling on sea surface temperature is negligible and not considered here, because both deep water and high-latitude surface waters have similarly low temperatures.

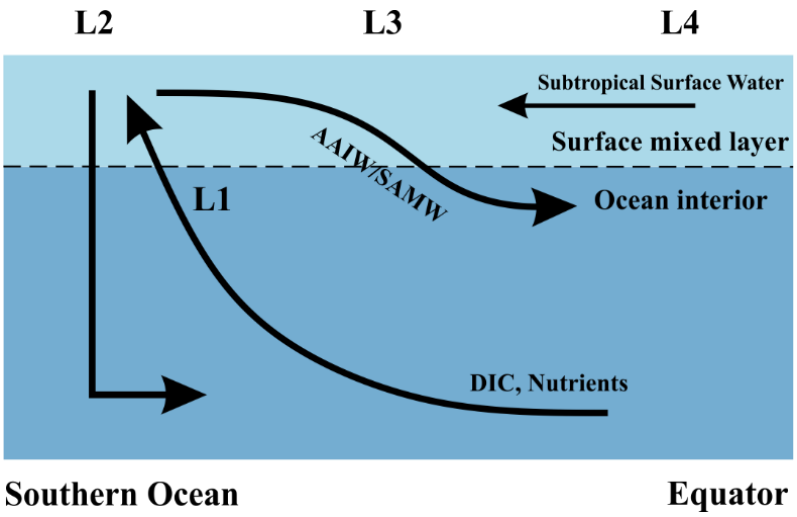

Figure 3.4. A schematic illustrating location of interest and assumed major flow paths in the Southern Ocean. Black arrows represent the flow directions of water masses. The lower curved arrow denotes upwelling of deep water along isopycnal surfaces, and the upper curved arrow denotes subduction to form Subantarctic Mode Water (SAMW) and Antarctic Intermediate Water (AAIW). L1: upwelling water below the mixed layer, prior to any influence of surface processes; L2: sea surface within the core of the Southern Ocean upwelling south of 50° S (Morrison et al., 2015); L3: sea surface from 30° S to 50° S; L4: sea surface north of 30° S which experiences no direct effects from upwelling in the Southern Ocean.

I first consider the increase in DIC induced by the upwelling of deep water with high DIC concentrations. While some of the initial increase is usually removed shortly afterwards by biological export fueled by the nutrients brought up at the same time, excess DIC remains if the subsequent biological removal of DIC does not match the initial increase. Phosphorus has the simplest nutrient behavior in the ocean with only one significant source to the ocean as a whole (river input) and one major sink (organic matter burial) (Ruttenberg, 2003; Tyrrell, 1999). In this study, the salinity-normalized phosphate (nPhos) concentration was used as a proxy for calculating how much salinity-normalized DIC (nDIC) was upwelled along with it and not yet removed again by biological uptake of phosphate and DIC. I used salinity-normalized concentrations to correct for the influence of precipitation (rainfall) that dilutes DIC and phosphate concentrations in proportion to the effects on salinity (Eq. 2.4). In this calculation, it was assumed that the only external source of phosphate to surface waters is from upwelling and the only subsequent loss is through export of organic matter, leading to the equation:

$$nPhos_{surf} = nPhos_{supply} - NCP/R_{C:P} \quad (3.5)$$

where the subscript ‘supply’ indicates the end-member concentration of deep water supplied along the upwelling isopycnals (i.e., the value at L1 in Fig. 3.4), and the subscript ‘surf’ indicates

the surface water concentration at some later time. NCP refers to the total time-integrated net community production (uptake and export by biology) in carbon units, and $R_{C:P}$ is the Redfield ratio of carbon to phosphorus. $R_{C:P}$ is given the standard value of 106:1 (Redfield, 1963), except for the cold nutrient-rich high-latitude region in the Southern Ocean (south of 45° S), where $R_{C:P}$ is given a lower value of 78:1 (Martiny et al., 2013). I only considered the spatial variation in $R_{C:P}$ in this study. $R_{C:P}$ has seasonal variation as well (e.g., Frigstad et al., 2011), but this is much smaller than its latitudinal variation. $nPhos_{surf}$ refers to the observed surface value of nPhos at some location distant from where upwelling occurs.

Another possible process involved in the change of DIC during its upwelling and subsequent advection is calcium carbonate ($CaCO_3$) precipitation and dissolution (Balch et al., 2016), which alters DIC and TA with a ratio of 1:2. In order to quantify the magnitude of this process, I used Alk^* (Fry et al., 2015) as an indicator, which is capable of diagnosing $CaCO_3$ cycling in the context of the large-scale ocean circulation (see more details on Alk^* distribution in Fig. 3.10). The change in Alk^* concentrations between its supplied and surface end-members is attributed to $CaCO_3$ precipitation/dissolution and assimilation of inorganic nutrients by primary production (Brewer and Goldman, 1976):

$$Alk^*_{surf} = Alk^*_{supply} - \Delta Alk^*_{CaCO3} - NCP/R_{DIC:TA} \quad (3.6)$$

$$Alk^* = \frac{Alk_m - Alk_r + 1.36 \times NO_3^-}{S} \times 35 + Alk_r - 2300\ \mu mol\ kg^{-1} \quad (3.7)$$

where $R_{DIC:TA}$ is the relative ratio of -106/17 between changes in DIC and TA during primary production (Wolf-Gladrow et al., 2007). Alk_m is the measured TA, Alk_r is the riverine TA end-member (zero in the Southern Ocean), and 2300 µmol kg^{-1} is the average TA in the low-latitude surface oceans. Alk^*_{surf} is calculated by Eq. 3.7.

Assuming the carbon source is from upwelled CO_2-rich deep waters and carbon sinks are from organic matter export (NCP) and $CaCO_3$ cycling, then:

$$nDIC_{surf} = nDIC_{supply} - NCP - 0.5 \times \Delta Alk^*_{CaCO3} \quad (3.8)$$

Three hydrographic sections, one in each of the Indian (I95E), Pacific (P150W), and Atlantic (A25W) oceans, were used to determine the different supply concentrations ($nPhos_{supply}$, Alk^*_{supply}, and $nDIC_{supply}$) for each basin (see Fig. 3.5c inset). In the Indian Ocean, $nPhos_{supply}$, Alk^*_{supply}, and $nDIC_{supply}$ along the 27.9 kg m^{-3} isopycnal are. 2.29 ± 0.01 µmol kg^{-1}, 109.4 ± 1.0 µmol kg^{-1}, and 2273.1 ± 1.1 µmol kg^{-1}, respectively (values here are expressed as mean ± standard error of the mean), as it approaches the surface. In the Pacific Ocean, $nPhos_{supply}$, Alk^*_{supply}, and $nDIC_{supply}$ along the 27.9 kg m^{-3} isopycnal are 2.32 ± 0.01 µmol kg^{-1}, 108.1 ± 1.9 µmol kg^{-1}, and 2277.2 ± 1.8 µmol

kg^{-1}, respectively. In the Atlantic Ocean, $nPhos_{supply}$, Alk^{*}_{supply}, and $nDIC_{supply}$ along the 27.6 kg m^{-3} isopycnal are 2.28 ± 0.01 µmol kg^{-1}, 103.5 ± 1.1 µmol kg^{-1}, and 2254.6 ± 1.3 µmol kg^{-1}, respectively (Fig. 3.5).

Since $nPhos_{surf}$ tends to decrease to zero upon moving northwards, due to biological uptake, $nDIC_{surf}$ has a relatively constant value in the subtropical regions (data not shown), where is not influenced by upwelling in the Southern Ocean. Because of this, the potential effect of upwelling on surface nDIC is calculated as the excess in $nDIC_{surf}$ compared to the subtropical average value (30° S-30° N):

$$\Delta nDIC_{upw\_st} = nDIC_{surf} - \overline{nDIC_{surf}\ (30° S\text{-}30° N)} \quad (3.9)$$

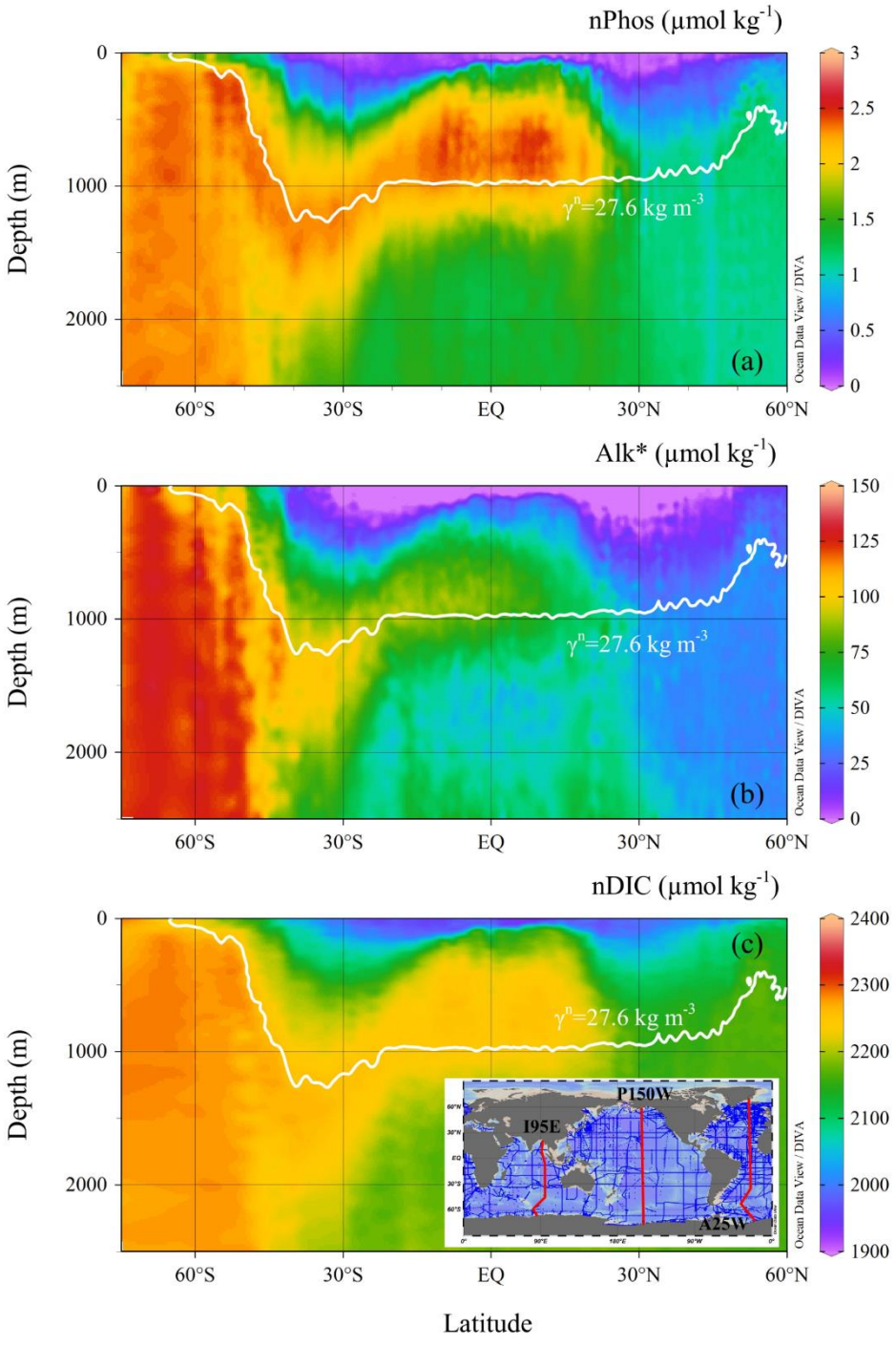

Figure 3.5. Vertical distributions of (a) nPhos, (b) Alk* and (c) nDIC along the Atlantic Ocean section. The Indian and Pacific sections are not shown. The selected Atlantic section (A25W) is shown as the red line on the right-hand side of the inset. The neutral density isopycnal along which upwelling occurs is indicated by the white contour, which is characterized by neutral density of 27.6 kg m^{-3} in the Atlantic sector of the Southern Ocean.

3.2.3.3 Upwelled TA-driven effect (long-term effect of upwelling)

Some effects of upwelling on DIC are temporary, becoming overridden later by gas exchange. In contrast, the effect of upwelled TA persists because it changes the equilibrium DIC with respect to gas exchange (DIC_{eq}) (discussed also in Section 3.4.1.3). Upwelling of high-TA water has a long-lasting effect on DIC because, if all else remains constant, an increase in TA decreases the fraction of DIC that exists as CO_2 molecules. The resulting decrease in CO_2 concentration lowers seawater partial pressure of CO_2 (pCO_2), having the potential to lower seawater pCO_2 to below atmospheric values which in turn drives an influx of CO_2 from the atmosphere, raising DIC (Humphreys et al., 2017).The effects of upwelling are complex because they consist of both direct and indirect effects on DIC (Fig. 3.2), lasting over both short (when DIC is altered but DIC_{eq} is not) and long (when DIC_{eq} is altered) timescales. The different effects and the meanings of the terms used here are illustrated in Fig. 3.6.

The calculation of the long-term effect of upwelling through upwelled TA in the Southern Ocean (i.e., the difference between DIC_3 and DIC_0 in Fig. 3.6) was achieved through five steps:

(1) Calculate TA in the Southern Ocean with the upwelling effect subtracted, TA_{nonupw}:

$$TA_{nonupw} = TA_{obs} - (Alk^{*} \times S_{obs} / 35) \quad (3.10)$$

where TA_{obs} is the observed in-situ TA, and Alk^{*} is the TA tracer (Fry et al., 2015) revealing excess TA supplied by the large-scale ocean circulation (upwelling in the Southern Ocean), as well as removal by calcification and export (Eq. 3.7). Since Alk^{*} is a salinity-normalized concept, it is necessary to restore it to the in-situ salinity before subtracting it from the in-situ TA.

(2) Calculate in-situ sea surface pCO_2, following the same method as described in Section 3.2.3.1.

(3) Calculate DIC with the effect of upwelled TA subtracted. I calculated DIC_{nonupw} using CO_2SYS with inputs of TA_{nonupw} and in situ pCO_2, SST and salinity.

(4) Normalize salinity for consistency with other calculated effects.

(5) Finally, the long-term effect of upwelling through the upwelled TA and the subsequent air-sea gas exchange is calculated as

$$\Delta nDIC_{upw\_lt} = nDIC_{obs} - nDIC_{nonupw} \quad (3.11)$$

where $\Delta nDIC_{upw\_lt}$ corresponds to the magnitude of ⑤ in Fig. 3.6.

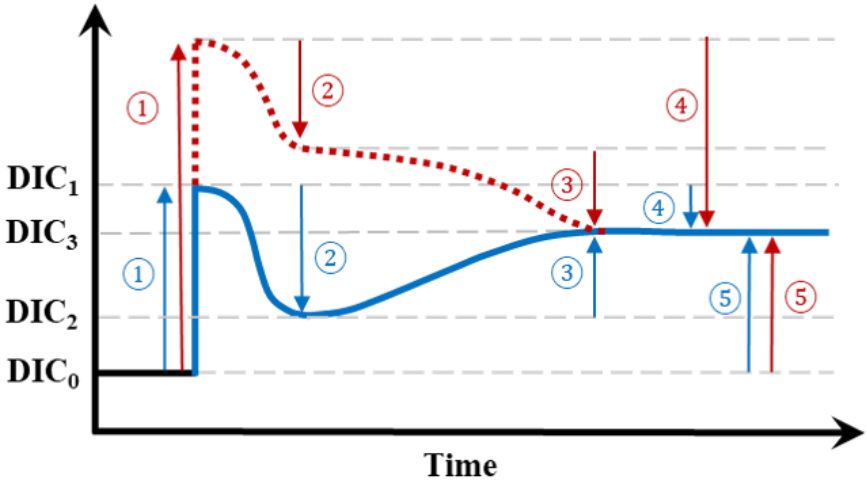

Figure 3.6. A schematic illustrating the various effects of upwelling on surface DIC. Numbers represent processes changing surface DIC, and arrows point in the direction of change: ①: the *direct effect* of upwelling which elevates surface DIC from DIC_0 to DIC_1; ②: the DIC uptake by biology supported by upwelled nutrients, dropping DIC from DIC_1 to DIC_2. The processes of ① and ② make up the *short-term* effect of upwelling (i.e., difference between DIC_2 and DIC_0); ③: the change brought about by air-sea CO_2 gas exchange which continues towards the equilibrium with the atmosphere (DIC_3, whose level is determined by the amount of upwelled TA as well as by temperature); ④: the combination of both ② and ③ makes up the total *indirect effect* of upwelling (the difference between DIC_3 and DIC_1); ⑤: the *long-term* impact of upwelling on the level of surface DIC is the difference between DIC_3 and DIC_0. Blue and red indicate two scenarios with different amounts of upwelled DIC relative to upwelled TA, but the same amounts of upwelled TA. Blue is for upwelled water with a deficit in additional DIC relative to additional TA whereas red is for an excess in DIC relative to TA.

3.2.3.4 Iron-driven effect

The iron-limitation-driven DIC differences (ΔDIC_{Fe}) relate to the concepts of "unused nutrient", which can be thought of as the amounts of macronutrients and DIC that are left behind after iron limitation brings an end to biological uptake, in those regions where iron is the limiting nutrient. Iron limitation alters the impact of upwelling. In locations experiencing upwelling but where nitrate is the proximate limiting nutrient, the quantity of upwelled DIC might more or less be balanced by the quantity of subsequently exported DIC (fueled by the upwelled nutrients). In the Southern Ocean, however, the two appear not to be close to balance, even before considering iron limitation. According to the calculations in Section 3.2.3.2, the ratio of the excess upwelled nDIC against nPhos is around 250:2.3 ≈ 109:1 for the Southern Ocean, considerably exceeding the low C:P (average ≈ 80:1) of organic matter in the region (Martiny et al, 2013). So even if all

upwelled phosphate were to be used up and then exported in biomass in conjunction with carbon, a considerable surplus of DIC would be left behind. A lack of iron in surface waters, however, leads to even more upwelled DIC being left behind after the end of blooms induced by the upwelled nutrients.

I used phosphate as the unused nutrient from which to calculated ΔDIC_{Fe}. For each 1°×1° grid in the surface open ocean, the unused phosphate was taken from its annual minimum concentration based on the monthly data in World Ocean Atlas 2013 version 2 (WOA 2013: https://www.nodc.noaa.gov/OC5/woa13/, Boyer et al., 2013). The unused phosphate was then converted into unused DIC based on a standard $R_{C:P}$ of 106:1 (Redfield, 1963) for most of the global ocean, with the exceptions described in Section 3.2.3.2.

The amount of ΔDIC_{Fe} was therefore calculated as:

$$\Delta DIC_{Fe} = \text{unused phosphate} \times R_{C:P} \quad (3.12)$$

3.2.4 Uncertainty estimation

Uncertainties in the effects of different drivers were determined by a Monte Carlo approach (following e.g., Juranek et al., 2009; Ribas-Ribas et al., 2014). For example, the uncertainty of $\Delta nDIC_{temp}$ was calculated as follows: (1) given that $\Delta nDIC_{temp}$ is the difference between $nDIC_{obs}$ and $nDIC_{SST=27}$ (Eq. 3.4), its uncertainty is propagated from the uncertainties of both $nDIC_{obs}$ and $nDIC_{SST=27}$, where the uncertainty of $nDIC_{obs}$ is 5 µmol kg^{-1} (Table 3.2), and the uncertainty of $nDIC_{SST=27}$ was determined by a Monte Carlo approach; (2) for calculation of the uncertainty of $nDIC_{SST=27}$ (see its function in Table 3.1), I first calculated artificial random errors (normally distributed according to the central limit theorem, with a mean of zero and a standard deviation equal to the accuracy/uncertainty of measurement) using a random number generator. Then, new carbonate system variable values (the original ones plus the randomly generated errors) were input into the CO_2SYS program (Van Heuven et al., 2011) to calculate new $nDIC_{SST=27}$ values. By doing this 1000 times, I obtained a set of 1000 different values for every single data point in the dataset. I used the standard deviations of these sets to characterize their individual uncertainties. The overall uncertainty of $nDIC_{SST=27}$ was 6.4 µmol kg^{-1}; (3) by applying the same Monte Carlo method, but to calculate the uncertainty propagated through Eq. (3.4), I then calculated the uncertainty of $\Delta nDIC_{temp}$ to be 8.0 µmol kg^{-1} (see Table 3.2 for other variables).

Table 3.2. Uncertainties for variables in this study.

Initial Variable	*Uncertainty*	*Reference*
Salinity	0.005	Olsen et al. (2016)
Phosphate	0.05 µmol kg^{-1}	Olsen et al. (2016)
DIC	4 µmol kg^{-1}	Olsen et al. (2016)
TA	6 µmol kg^{-1}	Olsen et al. (2016)
pCO_2	6.8 µatm	Takahashi et al. (2014)
DIC normalized to 2005	5.0 µmol kg^{-1}	derived in this study[a]
Alk^*	6.1 µmol kg^{-1}	Modified from Fry et al. (2015)
$nPhos_{supply}$, Alk^*_{supply}, $nDIC_{supply}$	See text in Section 3.2.3.2	derived in this study[b]
Calculated Propagated Uncertainties		
$\Delta nDIC_{temp}$	8.0 µmol kg^{-1}	derived in this study
$\Delta nDIC_{upw\_st}$	5.4 µmol kg^{-1}	derived in this study
$\Delta nDIC_{upw\_lt}$	8.9 µmol kg^{-1}	derived in this study

[a]the uncertainty of DIC normalized to 2005 was primarily propagated from TA and $pCO^{2005}_{2,sw}$. The uncertainty of $pCO^{2005}_{2,sw}$ was calculated from error propagation (Fornasini, 2008), to be 0.17 µatm.

[b]the uncertainties for variables with subscript "supply" were from their standard error of the mean.

3.3 Results

3.3.1 Spatial distributions of observed DIC and nDIC

Surface observations reveal values of DIC across the global ocean ranging from less than 1850 µmol kg^{-1} in the tropics to more than 2200 µmol kg^{-1} in the high latitudes (Fig. 3.1a). To first order, surface DIC increases polewards, being positively correlated with absolute latitude (Spearman's rank correlation coefficient $\rho = 0.71$ for the global oceans, Table 3.3). Spatially, it is monotonically inversely related to sea surface temperature ($\rho = -0.78$, Table 3.3), with DIC being highest where the surface ocean is coolest. Another conspicuous feature of surface DIC is the higher values (by ~100 µmol kg^{-1}) in the tropical and subtropical Atlantic Ocean relative to the same latitudes in the

Pacific and Indian oceans (Fig. 3.1a), as attributed to the transport of water vapor from the Atlantic to the Pacific (Broecker, 1989). This is not considered further here because our main purpose is to explain the sizable observed latitudinal gradients in DIC (on average 153 µmol kg^{-1} higher in the Southern Ocean than at low latitudes, for instance) and nDIC (on average 223 µmol kg^{-1} higher in the Southern Ocean than at low latitudes).

Salinity-normalized DIC (nDIC) increases towards the poles in all three ocean basins (Fig. 3.1b), although less strongly in the North Atlantic. The surface nDIC correlates more tightly with latitude and SST than does DIC, yielding a positive correlation with absolute latitude and a negative correlation with SST (ρ = 0.86 and -0.94, respectively for the global ocean, Table 3.3).

The distributions of surface DIC and particularly nDIC also show modest regional maxima in the eastern equatorial Pacific, the Arabian Sea, and the eastern boundaries of the Pacific and Atlantic ocean basins, presumably as a result of upwelling (Capone and Hutchins, 2013; Chavez and Messié, 2009; Millero et al., 1998; Murray et al., 1994).

Table 3.3. Global and regional correlations between DIC and nDIC and SST and Latitude.

		DIC vs. Lat		nDIC vs. Lat		DIC vs. SST		nDIC vs. SST	
Ocean	Region	ρ[a]	N[b]	ρ	N	ρ	N	ρ	N
Global		**0.71**	14228	**0.86**	14228	**-0.78**	14228	**-0.94**	14228
Southern Ocean	S of 40° S	**0.79**	3061	**0.81**	3061	**-0.93**	3061	**-0.95**	3061
North Atlantic	N of 40° N	**0.30**	1640	**0.58**	1640	**-0.34**	1640	**-0.78**	1640
North Pacific	N of 40° N	**0.02**	1601	**0.34**	1601	**-0.78**	1601	**-0.87**	1601

[a]the Spearman's rank correlation coefficient, for assessing monotonic relationships (there is a non-linear relationship between SST and CO_2 solubility). Statistically significant correlations are shown in bold.

[b]the number of data points from that area that were used in calculating the correlations.

3.3.2 SST-driven effect in the global surface ocean

The differences between the latitudinal patterns of DIC_{obs} and $DIC_{SST=27}$ are shown in Fig. 3.7. As expected, $DIC_{SST=27}$ agrees well with DIC_{obs} in the subtropics where SST is close to 27°C; the differences become larger with increasing latitude and decreasing SST (Fig. 3.7a-c). Correcting for salinity variations (Fig. 3.7d-f) greatly reduces the variability in DIC at low latitudes: $nDIC_{obs}$ is fairly constant at ~1970 µmol kg^{-1} in the subtropics. $\Delta nDIC_{temp}$ (Eq. 3.4 but for nDIC), the temperature-

driven CO_2 gas exchange effect on surface nDIC, increases sharply with latitude (Fig. 3.7g-i), reaching ~200 µmol kg^{-1} at 60° N in the northern part of the Atlantic and Pacific Oceans, and ~220 µmol kg^{-1} at 70° S in the Southern Ocean. The average $\Delta nDIC_{temp}$ in the Southern Ocean is 182 µmol kg^{-1}, which is large enough to account by itself for most - but not all - of the nDIC latitudinal gradient of 223 µmol kg^{-1} (2193-1970 µmol kg^{-1}).

ΔDIC_{temp} and $\Delta nDIC_{temp}$ are very similar in magnitude, with the largest deviations (at high latitudes) being less than 10 µmol kg^{-1}. Uncertainties associated with the salinity normalization process must therefore be small and are not considered further.

The estimated overall uncertainty of SST-driven effect on surface nDIC (Table 3.2) ranges from 5 to 8 µmol kg^{-1}, which is of comparable magnitude to the uncertainty of DIC normalized to 2005 and much smaller than the large latitudinal variations in $\Delta nDIC_{temp}$.

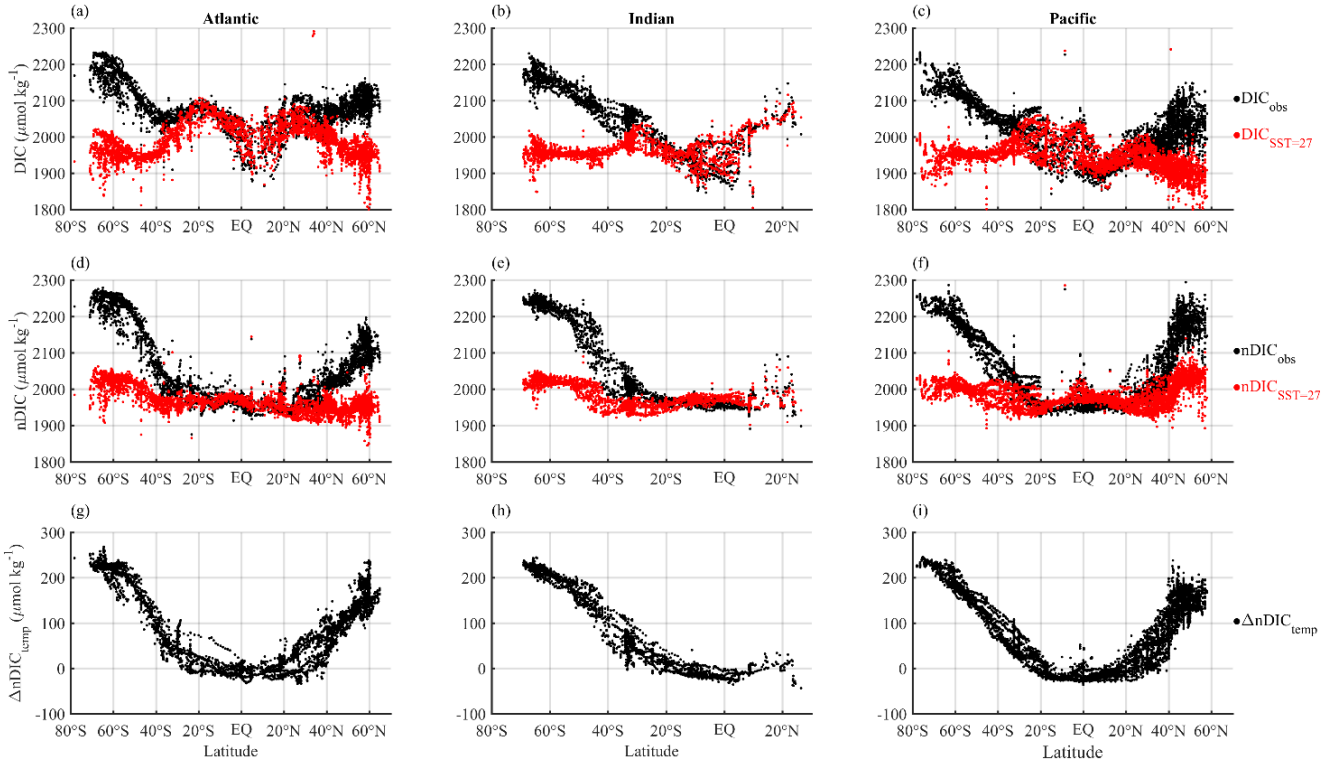

Figure 3.7. Latitudinal distributions of calculated temperature effect on surface DIC. Different columns show different basins (Atlantic, Indian and Pacific) and different rows show different calculated DIC variables. Panels (a), (b) and (c) show the observed surface DIC (black) and predicted DIC at SST of 27°C (red). Panels (d), (e) and (f) show the observed surface nDIC (black) and predicted nDIC at SST of 27°C (red). Panels (g), (h) and (i) show $\Delta nDIC_{temp}$, where $nDIC_{SST=27}$ is subtracted from $nDIC_{obs}$ to obtain the calculated temperature effect.

3.3.3 Upwelling-driven effects in the Southern Ocean

The upwelling-driven effects in the Southern Ocean calculated from both short- and long-term perspectives are shown in Fig. 3.8. The values were calculated from data collected along selected transects in each of the Atlantic, Indian, and Pacific sectors.

$\Delta nDIC_{upw\_st}$ increases polewards (Fig. 3.8a-c), with the same trends as surface phosphate (not shown), because it is calculated from phosphate. It can be seen that surface nDIC is potentially elevated dramatically by the Southern Ocean upwelling. The effect is of larger magnitude (average of 220 µmol kg^{-1} in the Southern Ocean) than that calculated for $\Delta nDIC_{temp}$ (Fig. 3.7g-i).

Fig. 3.8d-f show the long-term effect of upwelling, which is controlled by the concentration of TA in the upwelled water (how much upwelling increases surface TA values by). The average magnitude of $\Delta nDIC_{upw\_lt}$ is around 74 µmol kg^{-1} for the Southern Ocean.

The estimated overall uncertainty of upwelling-driven effects on surface nDIC (Table 3.2) ranges from 5 to 9 µmol kg^{-1}, close to the uncertainty of DIC normalized to 2005, and much smaller than the large latitudinal variations in $\Delta nDIC_{upw\_st}$ and $\Delta nDIC_{upw\_lt}$.

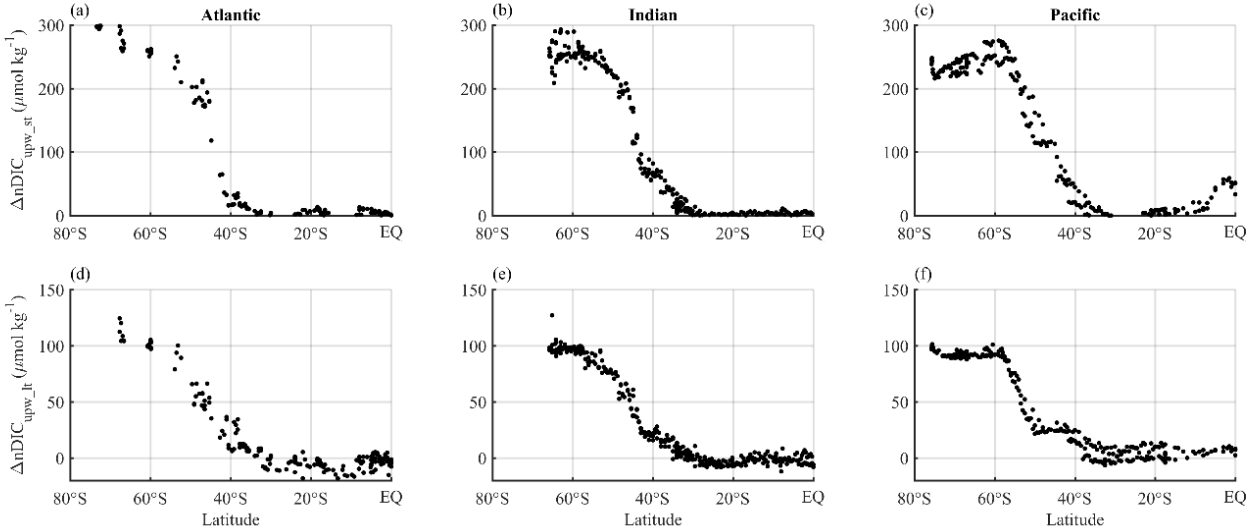

Figure 3.8. Latitudinal distributions of calculated upwelling effects on surface nDIC. Different columns show different sectors in ocean basins (Atlantic, Indian and Pacific) and different rows show different calculated effects on surface DIC. Panels (a), (b) and (c) show the short-term effect of upwelling ($\Delta nDIC_{upw\_st}$), which is driven by the direct supply of DIC from deep water and subsequent change by biology in the Southern Ocean. Panels (d), (e) and (f) show the long-term effect of upwelling ($\Delta nDIC_{upw\_lt}$), which is the difference between the observed nDIC value (determined mainly by the amount of upwelled TA, as well as by SST) and pre-upwelling nDIC value. The results were calculated from the three selected transects defined in Chapter 3.2.3.2.

3.3.4 Iron-driven effect in the global surface ocean

As shown in Fig. 3.9, ΔDIC_{Fe} is close to zero except in the classic HNLC regions (i.e., the North Pacific, the equatorial Pacific, and the Southern Ocean, Moore et al., 2013). There is also some residual nitrate during most summers in the Iceland and Irminger basins of the North Atlantic due to the seasonal iron limitation there (Nielsdóttir et al., 2009). The surface Southern Ocean south of 40° S has the largest unused DIC (ΔDIC_{Fe} of up to 180 µmol kg^{-1}, average of 120 µmol kg^{-1}), followed by the North Pacific 40° N-65° N (ΔDIC_{Fe} of up to 120 µmol kg^{-1}, average of 75 µmol kg^{-1}) and the equatorial Pacific (average of 35 µmol kg^{-1}). It is negligible elsewhere in the tropics and subtropics.

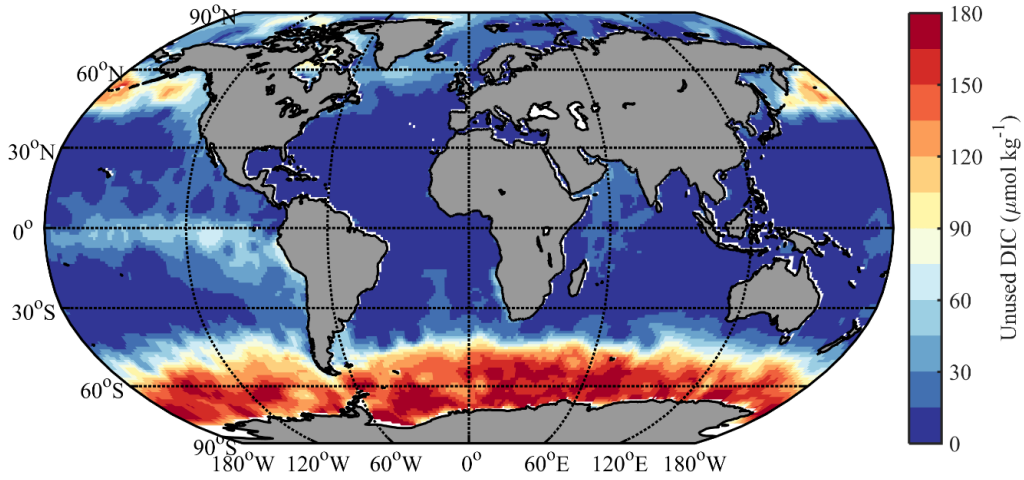

Figure 3.9. Calculated potential impact of iron limitation on surface DIC. Different colours correspond to different amounts of "unused DIC", calculated with the Redfield ratio from observed residual phosphate.

3.4 Discussion

3.4.1 Factors controlling the surface nDIC latitudinal variation

All effects discussed in this section are effects on nDIC rather than on DIC.

3.4.1.1 Effect of SST variation in the global surface ocean

The previously accepted explanation for higher DIC at high latitudes is that cooler SSTs there increase CO_2 solubility, resulting in a higher equilibrium DIC (Toggweiler et al., 2003a; Williams

and Follows, 2011). Our results support an important role for SST, but also that other processes contribute significantly.

Our analysis concludes that the latitudinal gradient in temperature is capable of raising nDIC by about 180 µmol kg^{-1} in the Southern Ocean, or in other words, explaining about four-fifths of the observed gradient of 223 µmol kg^{-1}. SST variation is thus able to explain most of the observed pattern.

3.4.1.2 Effect of TA distribution in the global surface ocean

A second factor that has been proposed as influential in driving spatial variations in the concentration of DIC in the surface ocean is TA (Williams and Follows, 2011). Our analysis supports this concentration, although I note that the effect of TA is most prominent at low latitudes. Large differences in DIC are observed between the subtropical gyres, where values are relatively high, and the vicinity of the Equator, where values are relatively low (Fig. 3.1a). These differences in DIC are driven initially by the direct effects of evaporation and precipitation on DIC. However, direct effects of evaporation and precipitation on TA also lead to indirect effects on DIC because of the influence of TA on the value of DIC required for gas exchange equilibrium with a given atmospheric CO_2 level. The indirect effects will dominate over longer timescales (Fig. 3.6). The role of TA explains the much clearer relationship between latitude and nDIC than between latitude and DIC (Fig. 3.1, Table 3.3); normalizing DIC to salinity is almost the same as normalizing DIC to TA, because salinity and TA are highly correlated in the surface open ocean. As a result, the effect of TA on DIC is counteracted by salinity normalization, with the pattern in nDIC (Fig. 3.1b) then revealing more clearly how other factors impact DIC.

The latitudinal pattern in TA is not the dominant driver of the DIC trend, because TA values are generally lower at high latitudes (where precipitation often exceeds evaporation) than they are at low latitudes (where evaporation often exceeds precipitation). However, TA is also biologically cycled and thus not perfectly correlated to salinity (Fry et al., 2015) and the presence of excess TA in deep water upwelled at high latitudes does contribute to the DIC trend.

3.4.1.3 Effect of upwelling in the Southern Ocean

Although not traditionally considered a factor, our analyses show that upwelling is important in driving the latitudinal gradient in DIC. Upwelling of DIC by itself is capable of producing an nDIC latitudinal gradient of 220 µmol kg^{-1} in the Southern Ocean, even higher than the effect of temperature (Fig. 3.8a-c, Table 3.4). However, the contribution of upwelling is reduced by about two-thirds if only the long-term effect through upwelled TA is considered (see Fig. 3.6 for definitions of terms).

Deep water usually has higher concentrations of nutrients, nDIC and nTA, than surface water does. Introduction of deep water into the surface mixed layer therefore usually stimulates increases in these concentrations, with three main consequences for DIC (Fig. 3.6), as follows. (A) If the upwelled water has higher DIC than the surface, the upwelling can cause an immediate initial increase in DIC; (B) additional nutrients stimulate phytoplankton blooms until the proximate limiting nutrient runs out, leading to a reduction in DIC over timescales of days to weeks (or months if, for instance, the upwelling occurs at high latitudes during winter when phytoplankton cannot bloom); (C) finally, air-sea gas exchange tends to remove any upwelling-induced air-sea CO_2 disequilibrium over a period of months to a year (Jones et al., 2014), although full equilibrium is seldom achieved across the global surface ocean (Takahashi et al., 2014).

The upwelling effects in Fig. 3.8 are calculations based on phosphate and TA concentrations, taking into account both the amount upwelled, and the amount subsequently removed by biology. They therefore correspond to the sum of the direct upwelling effect (① in Fig. 3.6) and the indirect upwelling effect through supplied nutrients (② in Fig. 3.6). There are two reasons why the initial amount of upwelled DIC considerably exceeds the amount of DIC subsequently taken up by phytoplankton growth fueled by the upwelled nutrients (why ① > ②) in the Southern Ocean.

Firstly, iron is typically much scarcer in deep waters than macronutrients are, relative to phytoplankton need (Moore, 2016). Regions like the Southern Ocean that are strongly influenced by upwelling are for this reason often iron-limited (Moore, 2016), leading to large amounts of 'unused DIC' (order of 120 μmol kg^{-1} in the Southern Ocean - Fig. 3.9) accompanying unused macronutrients. This scarcity of iron also leads to muted seasonal cycles of DIC (Merlivat et al., 2015) and thus year-round persistence of unused DIC. Secondly, as described in Section 3.2.3.2, the higher C:P ratio of supply (~109:1) compared to removal (~80:1) implies a considerable surplus of DIC even without iron limitation.

The upwelling effects shown in Fig. 3.8a-c are however relatively short term, and are expected to be overridden by air-sea gas exchange within months (Jones et al., 2014). They are thus likely to be most significant in the vicinity of where upwelling takes place (Morrison et al., 2015). For effects that may persist further away from locations of upwelling, it is important to also consider the long-term effect (⑤ in Fig. 3.6), the magnitude of which is dictated mainly by the change in TA brought about by upwelling. The level of TA in upwelled water (~2315, 2340, and 2337 μmol kg^{-1} in the Atlantic, Indian and Pacific sectors of the Southern Ocean, respectively; calculated according to the same method as in Section 3.2.3.2) are higher than the typical levels of TA in the surface waters of the high-latitude Southern Ocean (~2300, 2289, and 2288 μmol kg^{-1} in the

Atlantic, Indian, and Pacific sectors, respectively). The increase in TA brought about by upwelling corresponds to a long-term upwelling effect on nDIC of about 74 μmol kg^{-1} (Fig. 3.8d-f) in the Southern Ocean.

The results show that upwelling in the Southern Ocean can, by itself, generate high-latitude nDIC values that are around 220 μmol kg^{-1} greater than subtropical values. I emphasize that there is, in addition, a sizable long-term effect of upwelling (forcing nDIC values to be around 74 μmol kg^{-1} higher than they would be otherwise). Contrary to what might typically be assumed, the long-term effects of upwelling are dictated by the amounts of TA upwelled, and not by the amounts of DIC or nutrients.

3.4.2 A new understanding of the controls on the surface DIC distribution

Our analysis revises the prevailing paradigm of the causes of the latitudinal gradient in surface DIC. Previously, the gradient was thought to be completely explained by the effect of sea surface temperature on CO_2 solubility, but I have shown that upwelling is also an important contributor. DIC and nDIC would still be elevated at high latitudes even without any temperature effect.

Neither temperature patterns nor upwelling are responsible for all of the observed large latitudinal gradients in DIC and nDIC (for instance, the ~220 μmol kg^{-1} difference in nDIC between low latitudes and the Southern Ocean), but rather they are jointly responsible. There is an apparent contradiction because both $\Delta nDIC_{temp}$ and $\Delta nDIC_{upw\_st}$ appear to account for more than 80% of the nDIC latitudinal gradient. While both processes are capable individually of raising nDIC by 182 and 220 μmol kg^{-1} in the Southern Ocean, acting together they raise it by only 223 μmol kg^{-1} instead of 400 μmol kg^{-1}. An obvious explanation of this apparent paradox is that when we consider upwelling effects, we should consider not only its short-term effect through supplying DIC and nutrients (① + ② in Fig. 3.6), but also its long-term effect with gas exchange with the atmosphere (⑤ = ① + ② + ③ in Fig. 3.6), the amount of which is a function of the amount of upwelled TA (which, together with temperature, controls the equilibrium DIC). The sum of the SST-driven effect and the long-term effect of upwelling approximately equals the nDIC latitudinal gradient (Table 3.4).

On the global scale, therefore, the ultimate controls on the surface DIC and nDIC latitudinal gradients are the spatial patterns of SST and upwelling, and the chemical composition of the upwelled water.

Table 3.4. Summary of nDIC differences between low and high latitudes. Each ΔnDIC value is the amount by which the annual average nDIC value for the high latitude region exceeds the annual average value for the low latitudes (30° S to 30° N). Percentages in brackets represent the ratio of the observed nDIC difference in the second column; n.c. = not calculated.

Region[a]	Observed ΔnDIC (μmol kg^{-1})	$\Delta nDIC_{temp}$ (μmol kg^{-1})	$\Delta nDIC_{upw\_st}$ (μmol kg^{-1})	$\Delta nDIC_{upw\_lt}$ (μmol kg^{-1})
Southern Ocean	223	182 (82%)	220 (98%)	74 (33%)
North Atlantic	114	122 (107%)	n.c.	n.c.
North Pacific	192	137 (71%)	n.c.	n.c.

[a]the regions are defined as follows: North Atlantic: 40° N - 60° N; North Pacific: 40° N - 60° N; Southern Ocean: S of 40° S.

3.4.3 Importance of upwelling confirmed by the North Atlantic

From inspection of the global nDIC distribution (Fig. 3.1b), it can be seen that nDIC increases with latitude in all basins, but, as shown in Table 3.4, does so less strongly in the North Atlantic (difference between high latitudes and low latitudes of 114 μmol kg^{-1}) than in the North Pacific (difference of 192 μmol kg^{-1}). Although the latitudinal temperature gradient is less pronounced in the North Atlantic, this is not enough to explain the variation in gradients between the two basins: the average temperature of the high-latitude North Atlantic is 12.4°C and of the high-latitude North Pacific is 9.5°C, which can explain about 20 μmol kg^{-1} of variation between the two nDIC gradients but cannot explain the observed 78 μmol kg^{-1} variation (Table 3.4).

The reason for the discrepancy is that the Southern Ocean and the North Pacific experience elevations in values due to inputs of deep water whereas the North Atlantic does not. Upwelling occurs in the Southern Ocean and entrainment due to deep winter mixing occurs in the subarctic North Pacific (Mecking et al., 2008; Ohno et al., 2009) where it entrains waters high in both TA (Fry et al., 2016) and DIC. While deep winter mixing also occurs in the high-latitude North Atlantic (de Boyer Montégut et al., 2004), the entrained waters left the surface relatively recently and hence there is little accumulated remineralized DIC and TA in the deep water that is reintroduced to the surface. For this reason, winter entrainment produces little increase in surface nDIC in the North Atlantic. This makes the North Atlantic useful in discriminating between the two effects because, uniquely out of the three regions, only the SST effect operates there. As expected, the SST effect is able to completely account for the observed nDIC gradient in the North Atlantic, whereas it cannot in the other two regions (second and third columns in Table 3.4). The North

Atlantic confirms the important contribution of upwelling to latitudinal gradients, while also showing that latitudinal gradients occur in the absence of upwelling.

3.4.4 Comparison of nDIC distribution to Alk* and nutrients

Fig. 3.10 shows a comparison between the patterns of nDIC, the TA tracer Alk^* (Eq. 3.7, Fry et al., 2015) and salinity-normalized nutrients. The similarities and differences in distributions of Alk^* and nutrients have previously been discussed by Fry et al. (2015). Here I extend the comparison to also include nDIC. All exhibit low and fairly constant values at low latitudes. This is primarily due to biological uptake and restricted supply from subsurface waters, for most variables, but is primarily due to fairly uniform high temperatures for nDIC. All increase polewards due to upwelling/entrainment (and also declining SST for nDIC), and all exhibit maxima at high latitudes in the Southern Ocean and North Pacific. All exhibit a more modest increase in the North Atlantic than in the North Pacific, because the deep water formed relatively recently. There are differences in the latitudes at which the different parameters start to increase when moving from the Equator towards Antarctica, reflecting the different processes involved. Surface nDIC is the first to start increasing, under the influence of SST (third and fourth rows in Fig. 3.7), at 20° S to 25°S. Alk^* and nutrients, however, influenced by upwelling/entrainment, do not start to increase until somewhere between 30° S and 50°S.

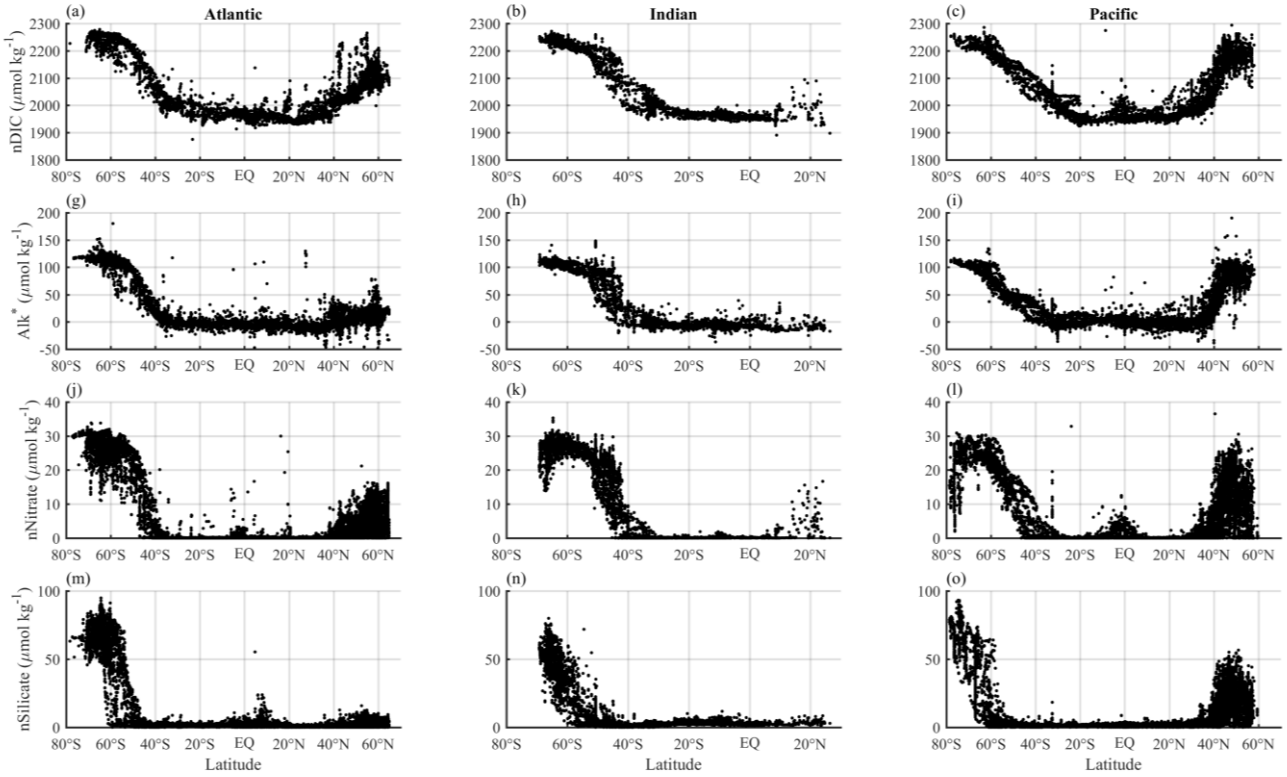

Figure 3.10. Latitudinal distributions of sea surface nDIC, Alk* (Fry et al., 2015), salinity-normalized nitrate and silicate in each ocean basin.

3.4.5 Implications for the future CO_2 sink under climate change

It is widely understood that global warming may alter the spatial distribution and intensity of upwelling in the ocean (Bakun, 1990; McGregor et al., 2007; Wang et al., 2015). It could either increase it on average, due to higher average wind speeds in a warmer, more energetic atmosphere (Bakun, 1990; Wang et al., 2015), or decrease it on average, due to enhanced stratification as the temperature differential between surface and deep waters is increased (Barton et al., 2013; Sarmiento et al., 2004). Furthermore, it is widely understood that an increase in upwelling would lead to an increase in the amount of CO_2 outgassed from the ocean, as larger quantities of CO_2-rich deep water are brought up to the surface and their CO_2 vented to the atmosphere (Evans et al., 2015; Marinov et al., 2006; Morrison et al., 2015). However, I have identified an additional effect here. Changes in upwelling would alter the distribution of carbon in the surface ocean not only through the supply of CO_2, but also through the supply of TA which determines the eventual surface carbonate system equilibrium with the same atmospheric pCO_2 (Humphreys et al., 2018). That is to say, the impact of changes in upwelling on the ocean's carbon source-sink strength depends not only on the DIC content of the upwelled water but also on its TA content. Ocean carbon cycle models should include these additional consequences if they are to make accurate predictions about the impacts of global warming on future carbon cycling. They should include the several routes identified here by which upwelling affects surface DIC: through upwelling of DIC, through upwelling of nutrients, and through upwelling of TA.

3.5 Conclusions

I investigated the global surface DIC and nDIC distributions in order to explain the large differences between high-latitude (especially Southern Ocean) and low-latitude regions. This issue has been addressed in previous studies and here I revisited it using new analytical approaches that lead to new findings. I considered three drivers for how the phenomenon could be explained: (1) sea surface temperature variations through their effect on CO_2 system equilibrium constants, (2) salinity-related TA variations through their effect on pCO_2, and (3) upwelling in the subpolar oceans. Our analyses confirmed that temperature plays a dominant role through its effect on solubility, and is able to explain a large fraction of the surface nDIC latitudinal gradient (182 µmol kg^{-1} out of 223 µmol kg^{-1} in the high-latitude Southern Ocean). Variations in TA associated with evaporation and precipitation are unable to explain higher DIC concentrations at higher latitudes, because alone they would drive the opposite DIC pattern. Their role is therefore to reduce the magnitude of the polewards gradient

in DIC. Upwelling, whose role in driving the large-scale spatial patterns has not previously been appreciated, accounts for a sizable component of the surface nDIC latitudinal gradient (on average 220 μmol kg^{-1} in the Southern Ocean). Its importance is magnified by the iron limitation that frequently occurs in upwelling areas, leaving behind residual upwelled excess DIC and macronutrients that cannot be utilized by biology. I emphasize that the upwelling of TA alongside DIC generates a prolonged effect that persists beyond CO_2 gas exchange re-equilibration timescales. The long-term effect of upwelling (74 μmol kg^{-1} in the Southern Ocean) helps explain the shortfall between the observed nDIC latitudinal gradient (223 μmol kg^{-1}) and the magnitude of the temperature-driven effect (182 μmol kg^{-1}). On the global scale, I conclude that no single mechanism accounts for the full amplitude of surface DIC latitudinal variations but that temperature and the long-term effect of upwelling, in that order, are the two major drivers.

Chapter 4 Coupled deviations from gas equilibrium of carbon dioxide and oxygen in the global surface ocean

Abstract

The distributions of dissolved carbon dioxide (CO_2) and oxygen (O_2) in the surface ocean have not previously been investigated in a comparative manner from a global perspective, despite their significance for life and climate. Here I present a new technique - CORS (Carbon and Oxygen Relative to Saturation) to detect different processes (e.g. photosynthesis and respiration, upwelling of deep waters) impacting the distributions of dissolved CO_2 and O_2 in oceanic surface waters. I applied it to the high-quality observational dataset GLODAPv2 (Global Ocean Data Analysis Project version 2). In some regions, surface dissolved CO_2 and O_2 are seen to both exhibit large seasonal deviations from equilibrium values with the atmosphere. Moreover, although dissolved O_2 returns to gas exchange equilibrium much more rapidly than does CO_2, nevertheless coupled deviations are observed. These coupled deviations will be useful for quality-controlling and interpreting autonomously-collected data from floats and gliders.

4.1 Introduction

The dissolved gases in seawater that are of greatest biogeochemical interest are carbon dioxide (CO_2) and oxygen (O_2). Carbon dioxide is important because of its role as a greenhouse gas, with about one quarter of the anthropogenic CO_2 produced by fossil fuel combustion and land use changes being absorbed by the ocean (Le Quéré et al., 2018). Time-series observations (Bates et al., 2014) show that the partial pressure of CO_2 (pCO_2) in surface seawater is rising at a similar rate to the atmospheric CO_2 concentration, which has increased by more than 40% since pre-industrial times (from 280 to over 400 ppm). Oxygen is biologically linked to CO_2, as the gases are inter-converted by marine organisms during organic matter production and remineralization. Global change is affecting oceanic O_2 concentrations; warming decreases the oxygen solubility and enhances water column stratification, thereby reducing ventilation of subsurface waters with atmospheric oxygen (Helm et al., 2011; Schmidtko et al., 2017; Stramma et al., 2008).

The distributions of the soluble gases O_2 and CO_2 are usually considered from the perspectives of O_2 concentration ($[O_2]$) and partial pressure of CO_2 (pCO_2). For precise determination of biological and physical contributions to O_2 supersaturation in the ocean, Craig and Hayward (1987) first developed a technique based on comparing the concentration of O_2 to that of biologically inert gas argon (Ar) (i.e., $\Delta O_2/Ar$), as Ar has similar air-sea exchange characteristics. The $\Delta O_2/Ar$ ratio has been applied widely in a series of studies investigating the relationships between $[O_2]$ and pCO_2 in oceanic surface waters (e.g, Guéguen and Tortell, 2008; Tortell et al., 2014; Tortell et al., 2015; Tortell and Long, 2009). Other studies compared concentrations of dissolved O_2 to saturating values and related changes in O_2 to those of other biologically-related elements, taking advantage of the Redfield (stoichiometric) ratio between carbon, oxygen, and nutrients (Bushinsky et al., 2017; Dai et al., 2009; Jiang et al., 2013; Körtzinger et al., 2008; Zhai et al., 2009).

Although previous studies have calculated concentrations of both O_2 and CO_2, to our knowledge none have compared both to atmospheric equilibrium and each other. Coupled changes were perhaps thought unlikely because the return to equilibrium is about 20 times more rapid for O_2 than for CO_2 (Sarmiento and Gruber, 2006), leading to an expectation of disequilibria being persistent for CO_2 but ephemeral for O_2. This supposition was supported by time-series observations in the Labrador Sea, where, following disequilibria produced by spring phytoplankton blooms, O_2 returned to equilibrium within at most a few months while CO_2 was still far from equilibrium 6 months later (Körtzinger et al., 2008). In this study I use the dissolved concentrations of O_2 and CO_2 ($[CO_2]$ and $[O_2]$) in surface seawater and do not use partial pressures. I compare concentrations to saturation values (values at which the net air-sea gas exchange rate is zero).

The saturation value is highly temperature-dependent. The first plot of [O_2] against temperature over much of the surface ocean (<20 m depth) was made in the early 1980s using data collected during the GEOSECS program (Broecker and Peng, 1982, updated subsequently by Sarmiento and Gruber, 2006). It suggested, for temperatures above 0°C, a fairly close correspondence between the observed [O_2] and its temperature-dependent saturation concentration. The supersaturation of oxygen over much of the global ocean is roughly of order 3% (Sarmiento and Gruber, 2006). The global database has been greatly expanded in recent decades, including wider spatial coverage and more measurements, culminating now in GLODAPv2 (Key et al., 2015; Olsen et al., 2016). This expanded dataset has not previously been used to compare simultaneous changes in [O_2] and [CO_2].

Processes known to influence the sea surface [O_2] and [CO_2] and their deviations from equilibrium with the atmosphere (ΔO_2 and ΔCO_2, Eq. 2.7, 2.8), can be divided overall into physical and biological processes (see Fig. 4.1 and inset to Fig. 4.2): (1) warming and cooling, through temperature effects on the solubility of the gases (Weiss, 1970; Weiss, 1974) and consequently their equilibrium values with the atmosphere; (2) introduction of atmospheric gases by bubble injection (Gruber and Sarmiento (2016) suggested that bubble injection accounts for 25% of the observed O_2 supersaturation of 3%, i.e., oxygen saturation anomaly of 0.75%); (3) evaporation and precipitation, through concentration or dilution of the dissolved gases; (4) mixing with other water masses of different chemical compositions, such as surface water with upwelled (CO_2-rich and O_2-depleted) deep water; and (5) photosynthesis and respiration (Anderson and Sarmiento, 1994; Redfield, 1963).

Here I present new insights into the distributions of and controls on surface ocean [O_2] and [CO_2] based on the large GLODAPv2 dataset. I present a new technique - CORS (Carbon and Oxygen Relative to Saturation) plots, capable of identifying regions and periods where processes are driving O_2 and CO_2 away from their equilibrium with the atmosphere. Our analyses demonstrate coupling between the O_2 and CO_2 deviations and significant geographic and seasonal differences in the dominant mechanisms driving the O_2 and CO_2 deviations.

4.2 Methods

Data for this study were obtained from GLODAPv2 (Key et al., 2015; Olsen et al., 2016), which includes data from over 700 cruises conducted during the period 1972-2013. Only open ocean data (seafloor depth > 200 m) were investigated. I excluded data from the Arctic Ocean (>65°N) because there are only a few observations and they just simply follow the temperature-dependent trend. The surface ocean is defined as waters shallower than 30 m at latitudes greater than 30°, and shallower than 20 m at latitudes less than 30° (Fry et al., 2015; Lee et al., 2006). The Southern Ocean is defined

as regions south of 50°S. Boreal spring is defined as from April to June, and austral spring from October to December, and so on for the other seasons (de Boyer Montégut et al., 2004).

4.2.1 Calculation of deviations of O_2 and CO_2 from saturation

The calculation of $\Delta[O_2]$ and $\Delta[CO_2]$ is described in Section 2.2.4.

4.2.2 Calculation of effects of different processes

Slopes of $\Delta CO_2/\Delta O_2$ in the inset to Fig. 4.2 were calculated based on global average sea surface conditions: sea surface salinity and temperature of 34.6 and 15°C, TA of 2300 µmol kg^{-1}, and atmospheric pCO_2 of 380 µatm (for the year 2005), which yields saturating concentrations of CO_2 and O_2 of 14.2 µmol kg^{-1} and 248.5 µmol kg^{-1}, respectively, and DIC of 2071 µmol kg^{-1}.

For calculation of the effects of warming and cooling, I calculated saturating gas concentrations along a temperature gradient (e.g., from 5°C to 25°C with an interval of 5°C), and then compared the saturating value at 15°C (T_0) to that at another temperature (T_1), using Equation 4.3:

$$\Delta\mathrm{Gas} = [\mathrm{Gas_{sat}}]^{\mathrm{T_0}} - [\mathrm{Gas_{sat}}]^{\mathrm{T_1}} \quad (4.1)$$

Instantaneous warming and cooling must have an immediate impact on the CORS values because changes in temperature alter gas solubility. In practice, however, impacts of sea surface temperature changes will only induce deviation from saturation if the rates of temperature-driven change are faster than can be counteracted by gas exchange. Warming decreases the gas solubility (equilibrium value), so warming actually increases ΔCO_2 and ΔO_2, and vice versa for cooling. The calculated relationship for warming is $[CO_2] = 0.086 \times [O_2]$; and the calculated relationship for cooling is $[CO_2] = 0.091 \times [O_2]$.

For calculation of the effect of ice melting, I assumed that ice contains no dissolved gases (Nomura et al., 2006; Loose et al., 2009), so [DIC] and $[O_2]$ are subjected to the same degree of dilution during ice melting). A degree of dilution gradient (e.g., diluted by 5%, 10%, 20%, and 30%) was then assumed for salinity, TA, DIC, and O_2. Each degree of dilution yielded a new carbonate system and therefore $[CO_2]$ was calculated using CO_2SYS (Van Heuven et al., 2011). By comparing each $[CO_2]$ and $[O_2]$ to their original values, the relationship between them for ice melting was calculated to be: $[CO_2] = 0.067 \times [O_2]$.

For the calculation of effects of photosynthesis and respiration, DIC changes were made proportional to changes in O_2 of ±25, ±50, ±75, ±100 µmol kg^{-1}. The corresponding DIC changes were calculated as O_2 changes multiplied by the Redfield ratio of $DIC/O_2 = -117/170$ (Anderson and Sarmiento, 1994; e.g. DIC changed by -17.2 µmol kg^{-1} when O_2 changed by +25 µmol kg^{-1} due to

photosynthesis). Using CO_2SYS (Van Heuven et al., 2011), [CO_2] was then calculated to change by -1.28 µmol kg^{-1} for this example (ΔO_2:ΔCO_2 ratio of +25:-1.28 ≈ -20:1). Same logic was applied to changes in [CO_2] and [O_2] due to respiration. The calculated relationship for photosynthesis is [CO_2] = -0.044 × [O_2]; and the calculated relationship for respiration is [CO_2] = -0.067 × [O_2].

4.3 Results and discussion

4.3.1 Seasonal distributions of surface [CO_2] and [O_2]

To first order, both [CO_2] and [O_2] follow a solubility-induced relationship with temperature, but with deviations in certain regions and seasons (Fig. 4.1). Deviations of O_2 from its equilibrium with the atmosphere are usually of the opposite sign to corresponding CO_2 deviations (Fig. 4.1).

In both hemispheres, [CO_2] deviates furthest from its temperature-dependent saturation value in spring and summer. In autumn and winter, on the other hand, it tends to stay close to saturation, as does [O_2].

In spring, strong supersaturation of CO_2 (together with undersaturation of O_2) is observed in parts of the north and eastern equatorial Pacific where water temperatures are close to 10 or 18°C (F1 in Fig. 4.1a,b). However, most of the rest of the Pacific data exhibits modest CO_2 undersaturation and accompanying O_2 supersaturation. Cold (sea surface temperature <5°C) parts of the Atlantic experience the most intensive CO_2 undersaturation (85% of the spring data in the Atlantic are undersaturated in CO_2), with lowest [CO_2] around 10 µmol kg^{-1} lower than at similar temperatures in other ocean basins (F2 in Fig. 4.1a,b). In spring, the distributions of O_2 generally mirror those of CO_2, except in the Southern Ocean where most (68%) of the data are observed to be undersaturated in CO_2, but only 32% are supersaturated in O_2.

The undersaturation of CO_2 becomes less pronounced in the Atlantic and Pacific Oceans upon moving from spring to summer. In summer, the most conspicuous and puzzling feature is the unusual combination of simultaneous CO_2 and O_2 undersaturations observed in the Southern Ocean (F3 in Fig. 4.1c, d). 84% of the CO_2 data and 46% of the O_2 data in the Southern Ocean show undersaturation in summer.

In autumn and winter, both gases become less variable as biological activity weakens. There are striking opposite changes to CO_2 and O_2 in the Southern Ocean (F4 and F5 in Fig. 4.1e-h), where [CO_2] is elevated to as high as ~30 µmol kg^{-1} and [O_2] depleted to as low as ~260 µmol kg^{-1}. Overall, both gases deviate more strongly from saturation in winter than in autumn.

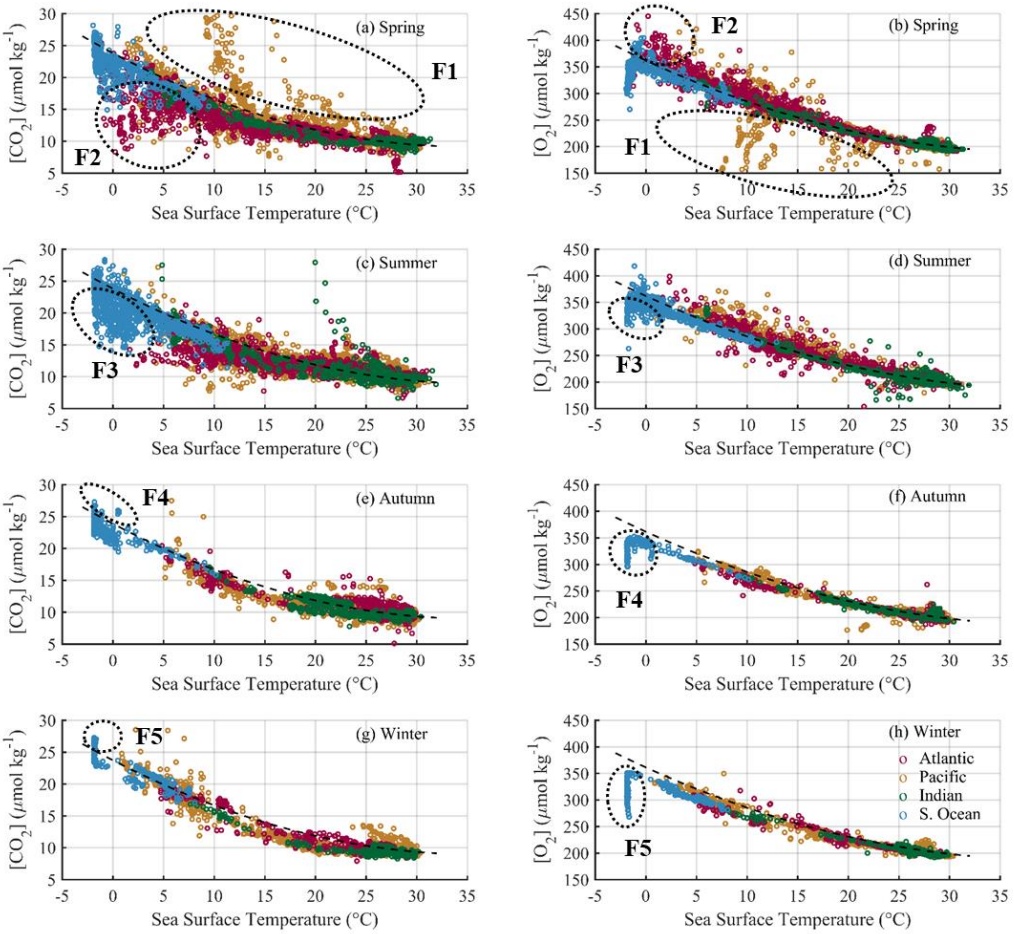

Figure 4.1. Seasonal distributions of sea surface dissolved CO_2 and O_2 against sea surface temperature in the global ocean. The black dashed curves indicate the saturation values of [CO_2] or [O_2] (i.e., concentrations that would be in equilibrium with the atmosphere). The saturation curves for [CO_2] were calculated with respect to the atmospheric pCO_2 of 380 µatm in year 2005. For this figure only, [CO_2] values measured in other years were adjusted to year 2005 following description in Section 2.2.1 to prevent artificial deviations from saturation. Colours indicate different ocean basins: Atlantic (magenta), Pacific (dark yellow), Indian (green) and Southern Ocean (blue). Dotted circles with labels F1-F5 highlight major features.

4.3.2 Controls on carbon and oxygen relative to their saturation

Figure 4.2 plots CO_2 deviations from saturation against O_2 deviations. Of the five features highlighted in Fig. 4.1, three also stand out in the CORS plots: (1) CO_2 undersaturation in association with O_2 supersaturation in the Atlantic and Pacific Oceans in spring (F2 in Fig. 4.2a); (2) simultaneous

undersaturation of both O_2 and CO_2 in the Southern Ocean in summer (F3 in Fig. 4.2b); and (3) supersaturation of CO_2 together with undersaturation of O_2 in the Southern Ocean in spring and autumn, but most strikingly in winter (F5 in Fig. 4.2d). Processes known to simultaneously affect ΔCO_2 and ΔO_2 include warming/cooling, ice melting, respiration and photosynthesis, and upwelling. Predicted impacts of these processes are shown in the inset to Fig. 4.2d.

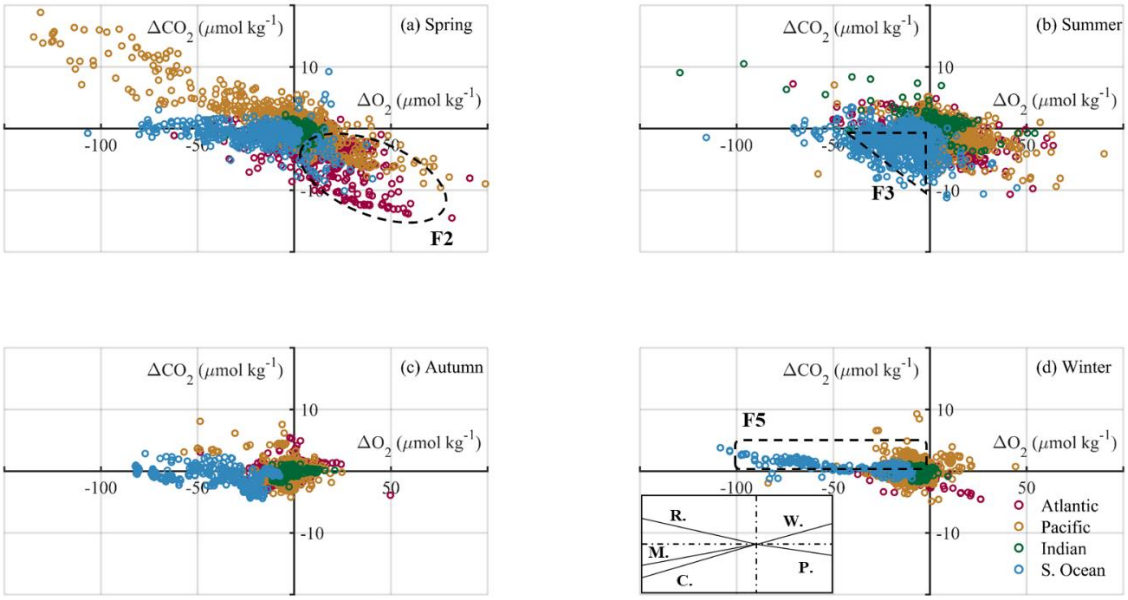

Figure 4.2. CORS plots: distributions of carbon and oxygen relative to their saturation in the surface global ocean in four seasons. Note the different axis scales for CO_2 and O_2. Colours indicate different ocean basins: Atlantic (magenta), Pacific (dark yellow), Indian (green) and Southern Ocean (blue). The inset in (d) shows the predicted effects (see methods) of different processes on ΔCO_2 and ΔO_2: warming (W), cooling (C), ice melting (M), photosynthesis (P) and respiration (R).

I suggest that F2 is caused by phytoplankton blooms (photosynthesis) which take up carbon and nutrients whilst producing oxygen. Fig. 4.3a shows a CORS plot of Atlantic and Pacific spring data, coloured by in-situ nitrate concentration. The data falling in the fourth quadrant (negative ΔCO_2 and positive ΔO_2) are associated with low nitrate concentrations and are located primarily in the Irminger Basin of the North Atlantic and the Oyashio region in the western subarctic Pacific Ocean, regions where intense spring blooms are observed (Henson et al., 2009; Mahadevan et al., 2012; Saito et al., 2002; Shiomoto, 2000). The data patterns are consistent with theoretical expectations of photosynthesis as the driver of the F2 deviations (see inset to Fig. 4.2d), although with differences in the slope of $\Delta CO_2/\Delta O_2$ from the expected trend (to be discussed in Section 4.3.3). Data in the opposite quadrant are from the eastern equatorial Pacific Ocean and off the northern California

coast, regions where seasonal upwelling is known to bring deeper waters (depleted in O_2 and enriched in CO_2 and nutrients from decomposition of organic matter) to the surface ocean (García-Reyes and Largier, 2012; Murray et al., 1994). The Pearson correlation coefficients (Table 4.1) show strong correlations between nitrate and CORS in the Pacific Ocean where upwelling dominates, whereas the correlations are weaker in the North Atlantic Ocean where phytoplankton blooms dominate.

Feature F3 can only be realized by a process that negatively changes both CO_2 and O_2 in summer, such as ice melting or cooling of surface water (Fig. 4.2d-inset). Most F3 data (CO_2 and O_2 both undersaturated) have below-average salinity, and about 40% of the F3 data locate at latitudes polewards of 66.5°S (the Antarctic circle) where ice melting may be partly responsible for the changes in ΔCO_2 and ΔO_2. The average salinity anomaly (anomaly from the mean surface salinity in summer in the Southern Ocean) south of the Antarctic Circle is -0.32, with a maximum of -1.40. Therefore, compared to the average summer salinity in the Southern Ocean of 33.83, the maximum dilution of seawater salinity resulting from ice melting is 1.40/33.83 = 4% at most, much less than the 10-20% required to explain the observed ΔO_2 and ΔCO_2. Table 4.1 also shows a fairly weak correlation between the salinity anomaly and CORS. Although Fig. 4.2d-inset implies that cooling of surface water can possibly cause undersaturation of O_2 and CO_2, it is difficult to envision this in summer, especially at the same time of sea ice melting, F3 therefore remains unexplained.

The undersaturation of O_2 and CO_2 actually starts in spring (Fig. 4.2a) then intensifies in summer. The ΔO_2 and ΔCO_2 signals contain a memory of processes that may have occurred several months ago as a result of their equilibrium timescales with the atmosphere lasting from weeks (O_2) to months (CO_2). The data in the Southern Ocean (Fig. 4.2) therefore nicely exhibit the seasonal evolutions of undersaturation of O_2 and CO_2 from winter to autumn.

Figure 4.3c shows the relationship between ΔCO_2, ΔO_2, and ΔNO_3^- in the Southern Ocean in winter, where ΔNO_3^- refers to the difference of surface in-situ nitrate concentration from its annual mean value in the surface Southern Ocean based on GLODAPv2 database. In the surface waters of the Southern Ocean south of 50°S nutrients remain at relatively elevated levels all the year round because of growth limitation of phytoplankton communities due to an insufficient iron supply (Boyd et al., 2000; Moore et al., 2013). Large differences in ΔNO_3^- (ranging from 0 to 8 µmol kg^{-1}) exist in the second quadrant between the data further away from the origin (ΔO_2 < -15 µmol kg^{-1}) and data close to the origin (-15 µmol kg^{-1} < ΔO_2 < 0 µmol kg^{-1}). The nitrate anomaly is strongly correlated with CORS (Table 4.1). Applying the opposite logic to the explanation for F2, the winter data in the Southern Ocean (Fig. 4.3c) imply that respiration (or, more likely, upwelling of old water into which organic matter has been respired) is responsible for F5.

Table 4.1. Regional correlations between NO_3^-, Salinity Anomaly, NO_3^- Anomaly and CORS (ΔO_2 and ΔCO_2).

		r [a]	
	Region	ΔO_2	ΔCO_2
		vs. NO_3^-	**vs. NO_3^-**
Second Quadrant in Fig. 4.3a	The Pacific Ocean	-0.69, n = 511	0.78, n = 511
Fourth Quadrant in Fig. 4.3a	The Atlantic Ocean	-0.14, n = 805	0.14, n = 805
		vs. S_{Anom}	**vs. S_{Anom}**
Third Quadrant in Fig. 4.3b	The Southern Ocean	0.17, n = 887	0.44, n = 887
		vs. NO_3^-, Anom	**vs. NO_3^-, Anom**
Second Quadrant in Fig. 4.3c	The Southern Ocean	-0.85, n = 213	0.60, n = 213

[a]the Pearson correlation coefficient (linear correlation) between two variables.

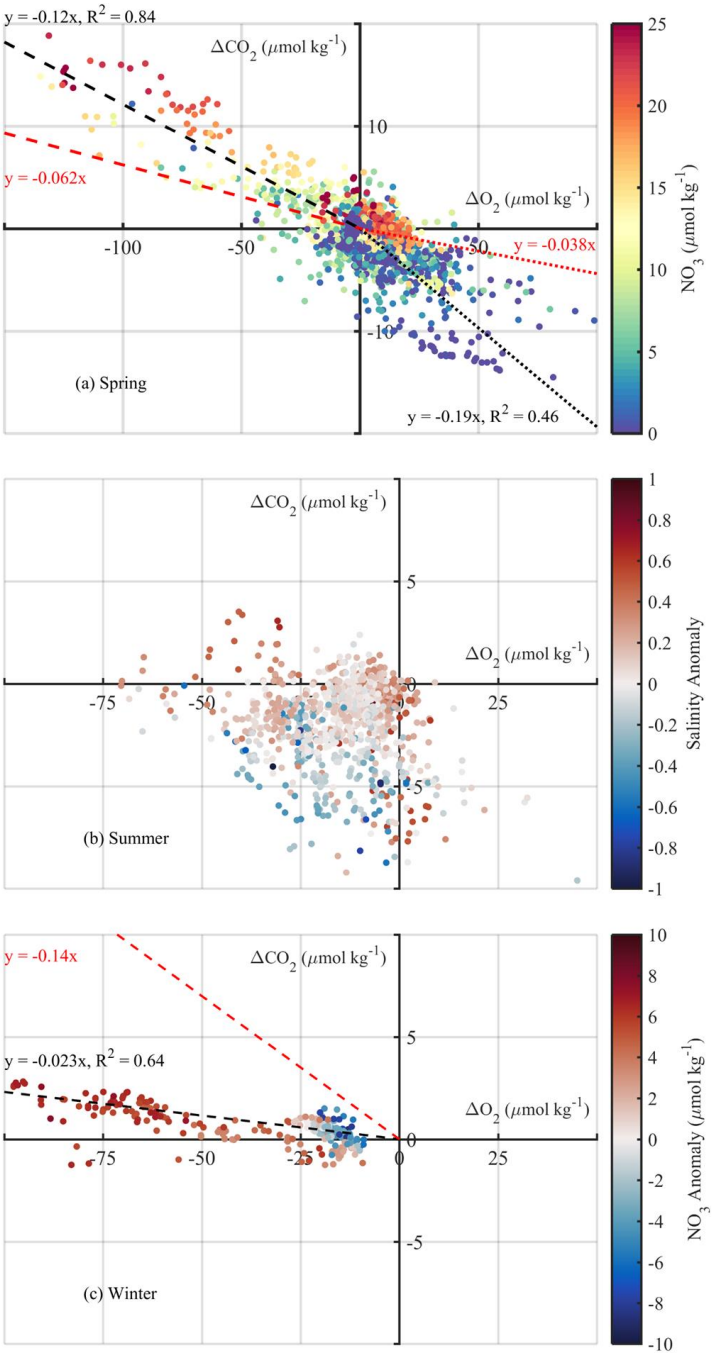

Figure 4.3. Colour-coded CORS plots for specific regions and seasons. (a) data in the Atlantic and Pacific Oceans in spring, coloured by the concentration of in-situ nitrate; (b) data in the Southern Ocean in summer, coloured by salinity anomaly (see text); and (c) data in the Southern Ocean in winter, coloured by nitrate anomaly (see text). The black dashed lines in (a) and (c) are the best-fit linear regressions (forced to intersect the origin) of data in the Pacific and the Southern oceans, respectively, in the second quadrant. The black dotted line in (a) is the best-fit linear regression (forced to intersect the origin) of data in the Atlantic, in the fourth quadrant. The red dashed and dotted lines in (a) are the expected slopes due to respiration and photosynthesis under average

conditions (the slopes are different from that in Section 4.2.2 because of different oceanic conditions applied) for the two specific regions (i.e., the Pacific data falling in the second quadrant and the Atlantic data falling in the fourth quadrant). The red dashed line in (c) is the expected slope due to respiration under average condition in the Southern Ocean.

4.3.3 Coupled ΔCO_2 and ΔO_2 deviations

As noted earlier, because of the buffering system of CO_2 in seawater (i.e., free CO_2 only accounts for ~0.5% of DIC, Zeebe and Wolf-Gladrow, 2001), it should take CO_2 around 20 times longer (Sarmiento and Gruber, 2006) to (re)equilibrate with the atmosphere than O_2. Because of these different air-sea equilibration timescales for CO_2 and O_2, O_2 deviations are expected to be short-lived and CO_2 deviations long-lived, as observed in the Labrador Sea (Körtzinger et al., 2008). The observations reported here show a greater than expected degree of coupling between O_2 and CO_2 deviations (Fig. 4.2). Furthermore, whereas rapid oxygen re-equilibration leads to a prediction that many points will lie along the ΔCO_2 axis in CORS plots (i.e. many points will have negligible ΔO_2 in conjunction with sizable ΔCO_2), in actuality the data exhibit if anything the opposite, with more points close to the ΔO_2 axis than the ΔCO_2 axis (Fig. 4.2). One possible explanation for this apparent contradiction between observations and theory lies in the much larger initial impacts on $[O_2]$ than on $[CO_2]$. As noted in Section 4.2.2, whereas the impacts of a phytoplankton bloom on $[O_2]$ and [DIC] are at close to -1:1, because CO_2 makes up only a small fraction of DIC, the impacts on $[CO_2]$ are much smaller; for this reason bloom impacts are in the ratio ΔO_2:$\Delta CO_2 \approx$ -20:1.

The different re-equilibration timescales of O_2 and CO_2 may however explain the discrepancy (fourth quadrant in Fig. 4.3a) between the red dotted/dashed line (predicted immediate effect of photosynthesis) and the black dotted/dashed line (best-fit to observations): in actuality O_2 re-equilibration is faster than CO_2 re-equilibration, resulting in a steeper slope in the best-fit regression to observations. A similar discrepancy exists in the second quadrant of Fig. 4.3a (predicted impact of respiration versus observed impact of upwelling in the Pacific).

It is also worth noting that the slope of -0.023 in the second quadrant of Fig. 4.3c (the Southern Ocean) significantly differs from the slope of -0.12 in the second quadrant of Fig. 4.3a (the Pacific Ocean), even though both are attributed in large part to upwelling. In fact, the expected slopes for these two regions also differ from each other because they are under different oceanic conditions: for instance, CO_2 solubility is much higher in the high-latitude Southern Ocean so that the change in $[CO_2]$ due to respiration is larger than elsewhere (per unit of organic matter respired).

The large discrepancy between the observed and expected slopes in the second quadrant in Fig. 4.3c is hard to explain by the longer equilibrium timescale of CO_2; it reveals that the distribution of CORS in the Southern Ocean in winter is controlled by physical (upwelling and entrainment) rather than biogeochemical processes. As shown in Fig. 4.4a and b, the deep water upwelled in the Southern Ocean (neutral density > 27.8 kg m^{-3}; Marshall and Speer, 2012) is seen to contribute to the formation of surface water masses. These consist of two endmembers: one endmember at the origin of coordinates where data are characterized by the lowest neutral density and shallowest depth (Fig. 4.4a, b), and another endmember, of similar CORS values to the deepest water, at latitude greater than 65°S (Fig. 4.4c). As a consequence, the characteristics of the deep water which upwells determines the $\Delta CO_2/\Delta O_2$ slope for the surface water in the Southern Ocean in winter.

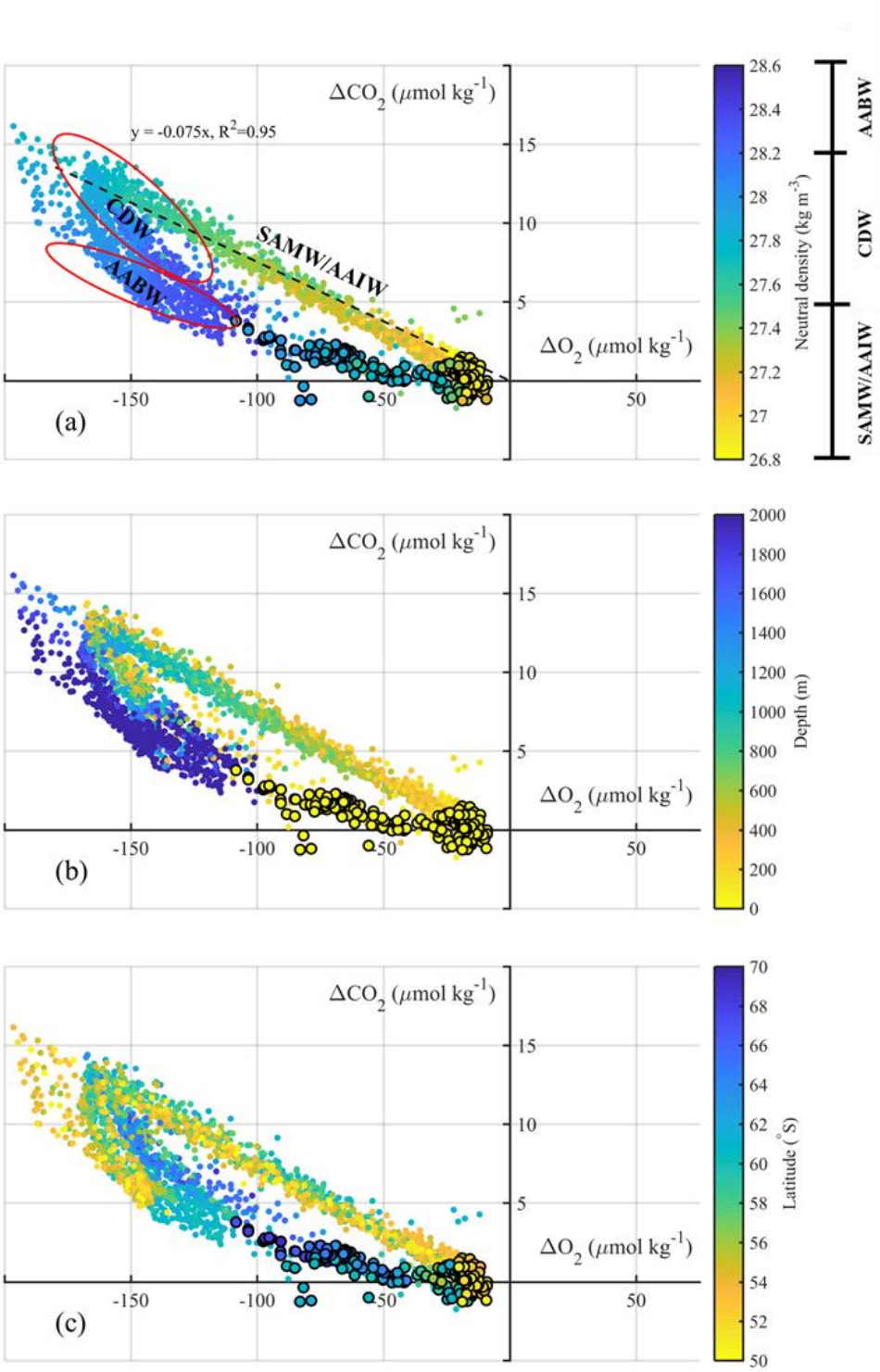

Figure 4.4. Comparison of ΔCO_2 and ΔO_2 between the surface, subsurface, and deep water in the Southern Ocean in winter. (a), (b) and (c) are the same data coloured by different variables ((a) neutral density, (b) depth, and (c) latitude). Circles with solid black edges denote surface water (shallower than 30 m), and circles without edges denote subsurface water (deeper than 30 m). The black dashed line in (a) is a best-fit linear regression line to subsurface (neutral density less than 27.8

μmol kg^{-1}) data in the second quadrant. The Subantarctic Mode Water and Antarctic Intermediate Water (SAMW/AAIW) were defined as water masses with neutral density ranging from 26.8 to 27.5 kg m^{-3}; Circumpolar Deep Water (CDW) was defined as neutral density ranging from 27.5 to 28.2 kg m^{-3}; and Antarctic Bottom Water (AABW) was defined as neutral density greater than 28.2 kg m^{-3} (Talley et al., 2003; Talley, 2013).

4.3.4 Utility in analysis of autonomously-collected data

Recent developments in sensor technologies have enabled an increasing amount of biogeochemical data to be collected autonomously by sensors mounted on gliders, floats, and moorings. These technologies have become increasingly important because they provide opportunities for sampling in remote regions and in inclement weather where traditional shipboard measurements are difficult and expensive. Along with the basic hydrological parameters (i.e., temperature and salinity), biogeochemical variables such as nutrients, oxygen and carbon (directly measured or indirectly calculated from pH) are now being measured (e.g. Gray et al., 2018). As a consequence, ΔCO_2 and ΔO_2 can be readily calculated, and hence the CORS technique can be applied. The application of CORS technique to future autonomously-collected datasets will have at least two benefits. On one hand, it will serve as a useful tool for detection of processes (e.g., bloom and upwelling) that simultaneously affect both oxygen and carbon. On the other hand, it will allow the validation of sensor's performance, important for sensors operating without human monitoring; because ΔCO_2 and ΔO_2 exhibit simultaneous and proportional changes, and because their scatterplots should intersect the origin (Fig. 4.2), systematic errors in either $[CO_2]$ or $[O_2]$ measurements can be visible in CORS plots.

4.4 Conclusions

A new method of visualizing carbon and oxygen data has been presented here, and applied to the large, high-quality, global dataset GLODAPv2. CORS plots provide a new insight into the identity and intensity of processes impacting CO_2 and O_2. Surprisingly, given that elimination of air-sea gradients should occur much more rapidly for oxygen, correlated simultaneous changes are seen in carbon and oxygen deviations from gas exchange equilibrium. Although both gas concentrations are usually close to the temperature-determined equilibrium value, three noteworthy deviations from equilibrium were noted and the possible processes driving them were discussed: (1) in spring, phytoplankton bloom (most notably those in the Irminger Basin of the North Atlantic and in the Oyashio region in the western subarctic Pacific Ocean) was identified as driving an undersaturation

of CO_2 and supersaturation of O_2; (2) in summer, a simultaneous undersaturation of both CO_2 and O_2 occurs in the Southern Ocean for reasons that are not understood; (3) in winter, upwelling in the Southern Ocean produces supersaturation of CO_2 and undersaturation of O_2. CORS is shown to have the potential to be a useful technique for revealing biogeochemical processes and for quality-controlling data from sensors on unmanned platforms.

Chapter 5 Carbon balance in the Drake Passage: an application of CORS

Abstract

This study is motivated by the recent challenging finding from autonomous biogeochemical floats of significant CO_2 outgassing in the high-latitude Southern Ocean. Here I present new insights into the Southern Ocean surface carbon balance. I do this by taking the Drake Passage as an example assuming Drake Passage to be representative of the subpolar Southern Ocean. Both observations and carbon balance estimations suggest the implausibility of significantly higher sea surface pCO_2 than atmospheric pCO_2 in Drake Passage. However, due to the lack of observational data, I cannot extend this result to the broader Southern Ocean outside the Drake Passage. Further, I take advantage of the CORS technique to examine the deviations of surface dissolved O_2 and CO_2 from their equilibrium with the atmosphere. By comparing the SOCCOM estimates to climatology, large discrepancies in pCO_2 and pH are found at regions outside the Drake Passage. In addition, the 'intercept issue' in the CORS plots from several floats is found to be most likely related to systematic bias in the measurements of pH and associated estimations of carbonate system parameters, which could result in biases in the estimated pCO_2 of up to -60 µatm.

5.1 Introduction

The Southern Ocean was recognized to play a crucial role in the global carbon cycle and climate a few decades ago (Sarmiento and Toggweiler, 1984). The Southern Ocean (south of 30°S) is responsible for around 40% of the global total oceanic sink of anthropogenic CO_2 (DeVries, 2014; Gruber et al., 2009; Gruber et al., 2019; Mikaloff Fletcher et al., 2006) even though it covers only 30% of the world's surface ocean. In addition, this region also acts to control the large-scale supply of nutrients to the low-latitude oceans and therefore the magnitude of low-latitude biological productivity (Sarmiento et al., 2004). The Southern Ocean is uniquely important due in large part to its circulation, in which deep waters from both the Atlantic and the Indo-Pacific upwell to the surface, and are then transformed into intermediate waters or densest bottom waters (Lumpkin and Speer, 2007; Marshall and Speer, 2012; Talley, 2013).

Observations and models have demonstrated large variability in the efficiency of uptake of CO_2 in the Southern Ocean over the past few decades. The strength of the Southern Ocean CO_2 sink was reported to have slackened from the 1980s to the early 2000s due to the increase in Southern Ocean winds which enhances the upwelling and outgassing of natural CO_2 (Le Quéré et al., 2007; Lovenduski et al., 2008). In contrast, recent studies (DeVries et al., 2017; Landschützer et al., 2015; Munro et al., 2015b) suggest reinvigoration of the Southern Ocean CO_2 uptake since 2002, due to the cooling in the Pacific Ocean, enhanced stratification in the Atlantic and Indian Ocean sectors, and a reduced overturning (Gruber et al., 2019; Landschützer et al., 2015).

Despite its vital impact on the carbon cycle and climate system, the Southern Ocean remains one of the most poorly sampled regions of the global ocean. The Drake Passage (DP) is, however, an exception with many observations made since 2002 as part of the Drake Passage Time-series. Because of the high-frequency observational data over time and space, the carbon cycle and carbonate system in DP is better understood (Fay et al., 2018; Munro et al., 2015a; Munro et al., 2015b) than elsewhere in the Southern Ocean. The carbon cycle in DP was also suggested by Fay et al. (2018) to be representative of a broader region in the Southern Ocean in both seasonality and long-term CO_2 trends.

With the aim of filling data gaps and gaining better understandings of the Southern Ocean carbon cycle, the Southern Ocean Carbon and Climate Observations and Modeling (SOCCOM) program started deploying in 2014 the first biogeochemical float array across the Southern Ocean. So far more than 150 floats, equipped with oxygen, nitrate, pH, and bio-optical sensors (Johnson et al., 2017) have been released, with 138 floats still being active (soccom.princeton.edu, latest access: 07

November 2019). The carbonate system data (e.g., pCO_2) were derived from the float-measured pH and algorithm-calculated TA. It was reported that the float-estimated pCO_2 values have an uncertainty of 2.7% (Williams et al., 2017); Takeshita et al. (2018) found that float values agreed well with the underway directly-measured pCO_2.

The SOCCOM floats have thus produced insightful understandings of the Southern Ocean's role in the global carbon cycle, with one of the most striking findings (Gray et al., 2018; Williams et al., 2018) being that the high-latitude Southern Ocean (the Antarctic Southern Zone) is outgassing CO_2 to the atmosphere in winter at a much greater rate (0.36 Pg C $year^{-1}$) than suggested by previous observational-based estimates (from -0.05 to 0.03 Pg C $year^{-1}$ according to Landschützer et al. (2014) and Takahashi et al. (2009)).

The discrepancy between previous studies and SOCCOM results motivated me to investigate the possibility of strong CO_2 outgassing in the Southern Ocean, by taking DP as representative. This study examines the surface pCO_2 level in DP in winter from both observations and theoretical estimation. I then take advantage of the new tool – CORS, described in Chapter 4 – to visualize and investigate the co-variations of surface ocean dissolved O_2 and CO_2, I also discuss the implications for our understanding for the likely validity of the SOCCOM estimates.

5.2 Methods

5.2.1 Study area: Drake Passage

A previous study divided DP into four regions according to its unique physical oceanography and the geographic setting (Munro et al., 2015a; Munro et al., 2015b). The strong flow of the zonally unbounded Antarctic Circumpolar Current (ACC) is constricted to as narrow as ~800 km, making DP a natural laboratory for investigating the entire ACC system over a relatively short distance (Sprintall et al., 2012). The four regions (Fig. 5.1) in DP are oriented parallel to the Antarctic Polar Front (APF) and the mean flow of the ACC, with two of them (R1 and R2) located north of the APF and the other two (R3 and R4) located south of the APF. The Subantarctic Front (SAF) locates within R1, and the APF locates between R2 and R3. The coordinates of the box corners from the top corner of Region 1 to the bottom corner of Region 4 are: 55.06°S, 63.29°W; 57.52°S, 70.97°W; 56.49°S, 61.87°W; 58.95°S, 69.85°W; 57.92°S, 60.39°W; 60.38°S, 68.71°W; 59.34°S, 58.85°W; 61.81°S, 67.54°W; 60.77°S, 57.26°W; and 63.24°S, 66.35°W (Munro et al., 2015a).

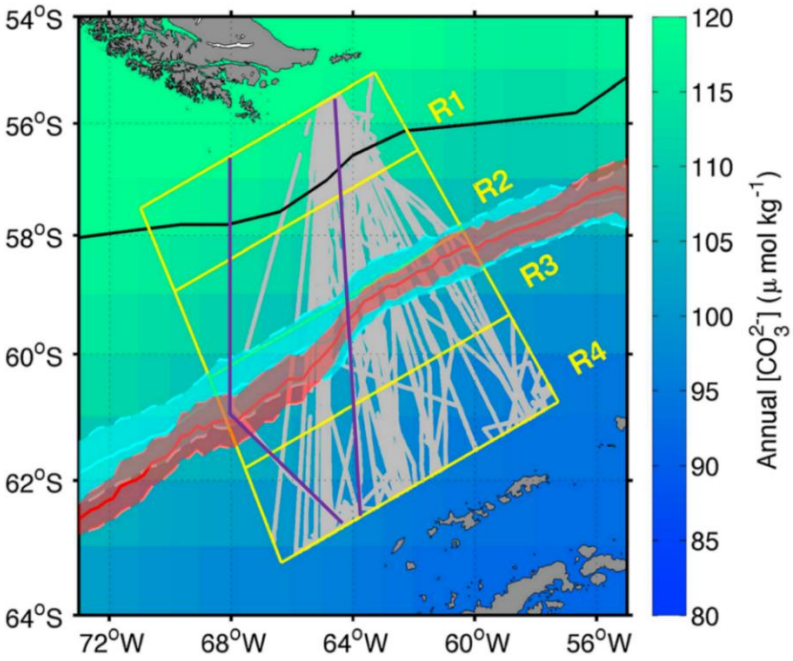

Figure 5.1. Drake Passage regions used in this chapter. Grey lines indicate cruise tracks with underway pCO_2 data (from 2002 to 2015). The black line indicates the mean position of the SAF. The red line (summer) and blue line (winter) with shadings (standard deviation of the APF position) indicate the position of APF in the two seasons (from 2002 to 2011). The background indicates the annual average concentration of carbonate ion. The purple polyline on the left-hand side indicates station locations with depth profiles collected in February 2009, and the purple straight line on the right-hand side indicates depth profiles collected in March 2006 and September 2009. Figure modified from Munro et al. (2015a).

5.2.2 Data source

This chapter uses several observational datasets of surface pCO_2 and carbonate system parameters in the Southern Ocean, mainly from the Drake Passage Time-series and SOCCOM floats. The austral spring is defined as from October to December, and so on for the other seasons. Below, I describe each in turn.

The Drake Passage Time-series

Discrete surface samples for parameters (e.g., salinity, macronutrients, and DIC) as well as high-frequency underway pCO_2 measurements were collected and measured on five to eight transects of DP per year by the Antarctic Research Supply Vessel *Laurence M. Gould* from 2002 to 2011. The carbonate system parameters as well as other biogeochemical variables measured onboard allow for

a comprehensive understanding of the biogeochemistry in DP. The analytical precision was ±2 µatm for underway pCO_2, and approximately ±1 µmol kg^{-1} for DIC (Munro et al., 2015a,b). TA was calculated from DIC, pCO_2, temperature, salinity, phosphate, and silicate data, as described in detail by Munro et al. (2015b). The estimated accuracy of each TA value was 2 µmol kg^{-1} based on the analytical precision of pCO_2 and DIC (Munro et al., 2015a,b; Takahashi et al., 2014). The computed TA values were relatively close to the measured TA values (of the samples with pCO_2, DIC, and TA measurements) by titration (root-mean-square deviation of ±4 µmol kg^{-1} (Takahashi et al., 2014)). Data are accessible at https://www.ldeo.columbia.edu/res/pi/CO_2/.

In addition to the surface measurements, depth profiles were carried out for investigating the vertical distribution of the carbonate system in DP at the end of summer and the end of winter: the research cruise in February 2009 (the purple cruise track on the left hand-side on Fig. 3.1), and research cruises in March 2006 and September 2009 (the purple cruise track on the right hand-side on Fig. 3.1). The data were obtained from the GLODAPv2 dataset, with uncertainties of 4 µmol kg^{-1} and 6 µmol kg^{-1} for DIC and TA, respectively (Olsen et al., 2016).

SOCCOM floats

The SOCCOM project (https://soccom.princeton.edu/) has deployed over 150 biogeochemical profiling floats in the Southern Ocean since 2014, each one mounted with a combination of biogeochemical sensors measuring water column pH, oxygen, nitrate, fluorescence, and backscattering (Johnson et al., 2017). With the measured pH and estimated TA using multiple linear regression (MLR, Williams et al., 2017; Williams et al., 2016) or locally interpolated alkalinity regression (LIAR, Carter et al., 2018; Carter et al., 2016) algorithms, pCO_2 and other carbonate chemistry parameters can be calculated from the collected observations (Williams et al., 2017). All float data were quality controlled as described in Johnson et al. (2017). The measured oxygen and pH have a reported uncertainty of 1% and 0.005 respectively (Johnson et al., 2017), and the estimated TA and pCO_2 have a reported uncertainty of 5.6 µmol kg^{-1} and 2.7% respectively (Williams et al., 2017).

The uncertainty associated with the float-estimated pCO_2 mainly results from three factors: accuracy of the estimated TA, accuracy of the measured pH, and the choice of equilibrium constants used for calculating the carbonate system (Williams et al., 2017). Among them, the accuracy of the measured pH was proven to be the dominant factor (Takeshita et al., 2018; Williams et al., 2017). According to a quality control assessment through December 2016 (Johnson et al., 2017), the pH sensor was

recorded to have the lowest percentage (88%) of good data return, while the oxygen sensor had the best percentage (100%) of good data return. The oxygen sensor has therefore been shown to be robust, with good stability, and almost all the oxygen data passed the preliminary quality checks (Johnson et al., 2017). The oxygen sensor data was further corrected with respect to the atmospheric oxygen when the float surfaced, and the correction could be applied to the entire profile (Johnson et al., 2017). The pH data were corrected for offsets and drifts over time by an empirical algorithm method, after compared values at 1500 m depth to the nearest available ship-collected data from GLODAPv2 (Williams et al., 2016). From the crossover comparison to GLODAPv2, the float-measured oxygen data tend to show great performance (the slope of the oxygen data versus the GLODAPv2 data at the crossover stations is very close to 1), while the float-measured pH data exhibit large offsets (0.031 at pH = 8.05) and the slope is significantly lower than 1 (Johnson et al., 2017).

Apart from these datasets, I also used the **LDEO** (Lamont-Doherty Earth Observatory) dataset to understand the climatological distribution of the carbonate chemistry in DP. This is also known as the Takahashi et al. (2014) climatology (T14) which is built upon the data synthesis of the GLODAP database (Key et al., 2004). The climatological distributions for TA, pCO_2, pH and DIC in surface waters of the global oceans were calculated and interpolated into 4°×5° box areas for the reference year 2005 (https://www.ldeo.columbia.edu/res/pi/CO_2/; see also Takahashi et al., 2014 for detailed calculations) . The estimated uncertainties for TA and pCO_2 are ±10 µmol kg^{-1} and ±10 µatm respectively; the combined uncertainty for each of the computed properties is ±0.01 for pH, and ±10 µmol kg^{-1} for DIC.

5.2.3 Data processing

5.2.3.1 Normalization of pCO_2 and DIC to a reference year

In order to prevent the temporal CO_2 trends (due to invasion of ever larger amounts of anthropogenic CO_2) from generating artificial spatial variability due to anthropogenic influence, I applied a different correction to the surface Drake Passage Time-series carbonate chemistry data than the method described in Section 2.2.1. The aim was to provide a more accurate correction for this specific region. Instead of the global scale correction described in Section 2.2.1, surface pCO_2 and DIC were normalized to the year 2005 using a mean decadal rate of changes of 19 µatm $decade^{-1}$ (for pCO_2) and 11 µmol kg^{-1} $decade^{-1}$ (for DIC), respectively (Takahashi et al., 2014), according to the multi-decadal time-series observations of carbon chemistry across DP.

5.2.3.2 Surface carbon balance calculation

Figure 5.2 shows the seasonal changes in water mass properties in DP area (Evans et al., 2014). In winter, a large amount of Antarctic Winter Water (AAWW) and Antarctic Intermediate Water (AAIW) are formed due to strong surface cooling and consequent deep mixed layers, whilst in summer, AAWW is eroded through surface warming and interior mixing with surface water until the following winter. Compared to the surface water in either summer or winter, AAWW is supposed to exhibit increased salinity and DIC (Table 5.1; see also Evans et al., 2014), indicative of the denser waters and accumulated CO_2 during remineralization. By quantifying the individual contributions of Summer Surface Water (SSW) and AAWW to the surface carbon balance in Winter Surface Water (WSW), I can then reach an estimate of how seasonal water mass transformation changes surface DIC and pCO_2. Note that I divide the Antarctic Surface Water (AASW, Fig. 5.2) into SSW and WSW according to different seasons.

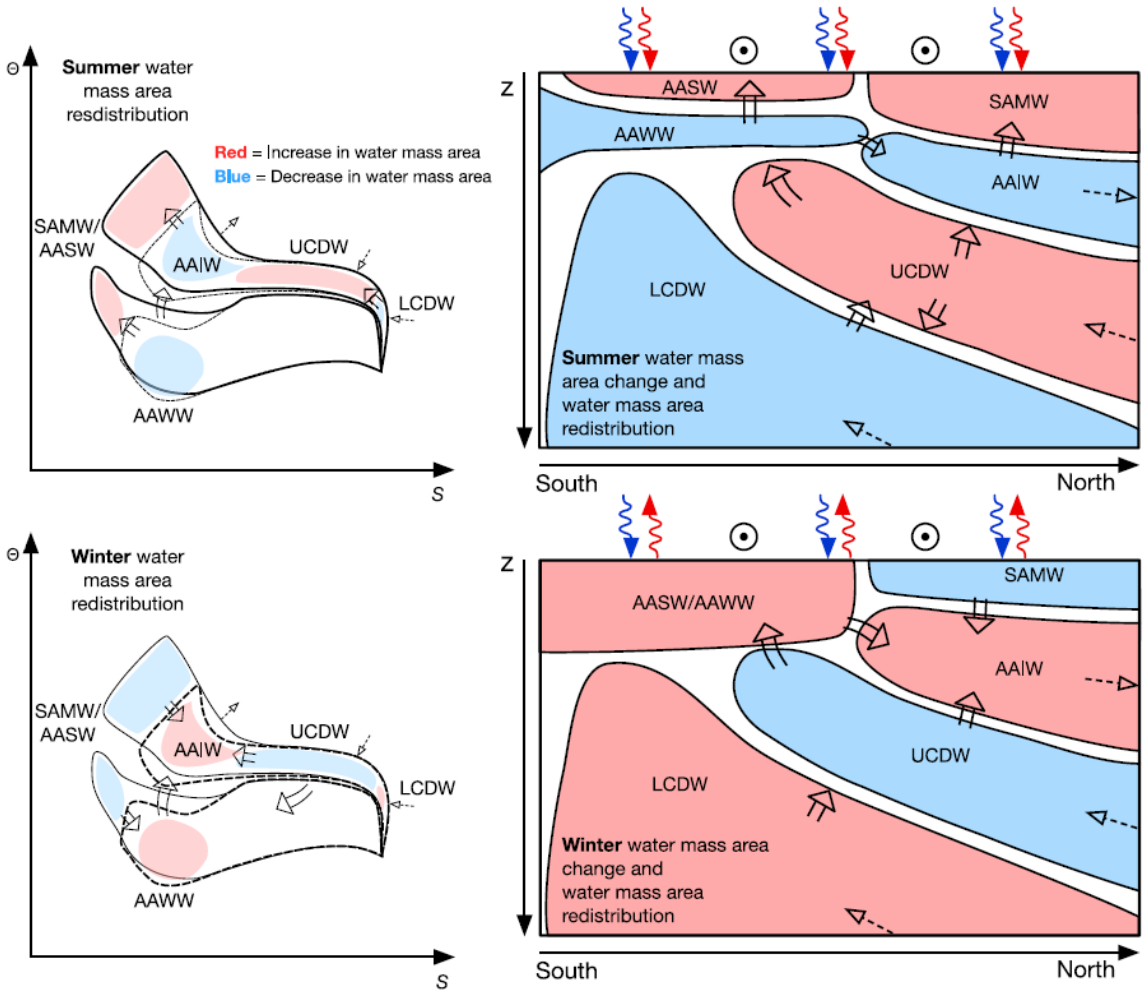

Figure 5.2. Schematic showing the changes in the distributions of water masses during (top) summer and (bottom) winter in thermohaline coordinates (left) and depth vs. latitude coordinates (right) highlighting processes affecting the key water masses within DP. In both, the solid black arrows indicate the transformation of water mass and the dashed black arrows represent an advection of water into and out of the geographical domain from which water mass area is calculated. The colour change represents the change in water mass area (red = increase, blue = decrease). In the thermohaline coordinate schematic, the solid line and dashed lines are the summer and winter distributions of water mass area, respectively. In the depth vs. latitude coordinate schematic, the red and blue arrows represent fluxes of heat and freshwater, respectively, in or out of the ocean and the black circles with dots represent the direction of the zonal winds out of the page. Figure from Evans et al. (2014). SAMW is Subantarctic Mode Water; UCDW/LCDW is Upper/Lower Circumpolar Deep Water.

Due to the fact that most of the SOCCOM-suggested strong CO_2 outgassing occurs in the zone around Antarctica (Gray et al., 2018; Williams et al., 2017), I chose zone R4 (R3 was excluded because of the lack of depth profile data in this region) in DP (Fig. 5.1) to investigate the surface carbon balance. During the mixing of SSW and AAWW to make WSW, the fraction of AAWW (f_{AAWW}) was calculated as the amount necessary to change the surface concentration [X] of a specific tracer from its observed value at the beginning of the entrainment (summer months: January to March) period to the value at the end of the entrainment (winter months: July to September), according to Equations 5.1 and 5.2:

$$f_{SSW} + f_{AAWW} = 1 \quad (5.1)$$

$$([X]_{SSW} \times f_{SSW}) + ([X]_{AAWW} \times f_{AAWW}) = [X]_{WSW} \quad (5.2)$$

where $[X]_{SSW}$ is the concentration in Summer Surface Water, and $[X]_{WSW}$ is for Winter Surface Water. Two conservative parameters, total alkalinity (TA) and absolute salinity (S_A), were chosen to quantify this process separately. The absolute salinity is defined as the mass fraction of salt in seawater as opposed to practical salinity which is essentially a measure of the conductivity of seawater to describe the salt content of seawater; absolute salinity is an SI unit of concentration with units of g kg^{-1}.

The AAWW water mass is defined by its characteristic ranges in absolute salinity and conservative temperature (T_{cons}), with S_A ranging from 34 g kg^{-1} to 34.3 g kg^{-1}, and T_{cons} ranging from -2 °C to 1°C (Evans et al., 2014). The conservative temperature is a new standard for ocean temperature adopted by the oceanographic community as part of the Thermodynamic Equation of Seawater – 2010 (TOES-10), which is based on a hypothetical adiabatic and isohaline change in pressure to the sea surface. Table 5.1 summarizes the average values of the two tracers as well as the carbonate parameters in each mixing endmember; the values for AAWW were taken from depth profile data (see Section 5.2.2), and the values for SSW and WSW were taken from the Drake Passage Time-series dataset. DIC and pCO_2 values were normalized to the reference year 2005. The Gibbs-SeaWater (GSW, McDougall and Barker, 2011) Toolbox was used to calculate absolute salinity and conservative temperature. The advantages of using S_A and T_{cons} over practical salinity and potential temperature are described in more detail in IOC et al. (2010).

Table 5.1. Values of absolute salinity (S_{abs}), conservative temperature (T_{cons}), TA, DIC, and pCO_2 in each endmember water mass. The surface waters were defined as depths shallower than 30 m.

	S_A (g kg^{-1})	T_{cons} (°C)	TA (μmol kg^{-1})	DIC (μmol kg^{-1})	pCO_2 (μatm)
AAWW					
value	34.1	-0.67	2301.3	2174.2	355.6
n*	91	91	37	40	19
S.D.**	0.07	0.58	7.6	17.6	31.2
SSW					
value	33.9	2.39	2275.3	2133.8	359.1
n	12846	12846	12798	12167	13091
S.D.	0.09	0.80	6.9	12.4	20.7
WSW					
value	34.0	-1.33	2279.0	2164.8	368.9
n	7102	7102	7091	6573	6848
S.D.	0.10	0.29	7.8	10.0	13.5

*the number of data for the analysis.

**standard deviation.

5.2.3.3 Carbon and oxygen relative to saturation calculation

The CORS technique was applied in this Chapter to the SOCCOM float data to investigate the deviations of O_2 and CO_2 from their saturations in the surface waters, as well as to validate the sensors' performance: the deviations of O_2 and CO_2 from their saturations should exhibit simultaneous and proportional changes, and the overall pattern of ΔO_2 vs. ΔCO_2 should basically follow the larger scale trend observed in the Southern Ocean (as shown in the previous chapter using GLODAPv2 data).

The calculation of CORS is described in Section 2.2.4.

5.3 Results

5.3.1 Spatial distribution of surface pCO_2, pH, TA and DIC in the Drake Passage

The February and August values of the carbonate chemistry parameters are shown in Fig. 5.3 as examples to represent the austral summer and winter conditions in DP respectively. The spatial distributions of all these parameters in the surface waters mostly exhibit a meridional trend:

The pCO_2 distributions are distinctly different in summer and winter (Fig. 5.3 a,b). The pCO_2 decreases polewards in summer and, in contrast, increases polewards in winter. Surface waters are undersaturated with respect to the atmospheric CO_2 level of around 380 µatm (in 2005) in summer, ranging from 300 to 370 µatm; however, some regions are supersaturated in winter. The southern part (south of the APF, ~ 60°S) of DP experiences the greatest seasonal variation in pCO_2 (amplitude of 80 µatm). The latitudinal gradient in pCO_2 is also sizable in both summer and winter, with spatial variation of up to 50 µatm in winter.

The pH distributions mirror pCO_2 well (Fig. 5.3 c,d), ranging from 8.01 to 8.14 from winter to summer, with a seasonal amplitude of 0.09 units in the southern part.

In contrast to the distributions of pCO_2 and pH in DP, TA does show a weaker meridional trend in summer (Fig. 5.3 e). The TA values are fairly constant in the core zone of DP (R1 to R4 in Fig. 5.1) in both summer and winter, with spatial variation of less than 15 µmol kg^{-1}. The TA values also show an increasing polewards trend, similar to pCO_2, in winter.

The DIC values range between 2080 µmol kg^{-1} in the northern DP in summer to 2200 µmol kg^{-1} in the polar regions in winter (Fig. 5.3 g,h). The amplitude of seasonal change is generally about 60 µmol kg^{-1} for areas south of the APF, and the amplitude of spatial change from SAF to APF is about 50 µmol kg^{-1}.

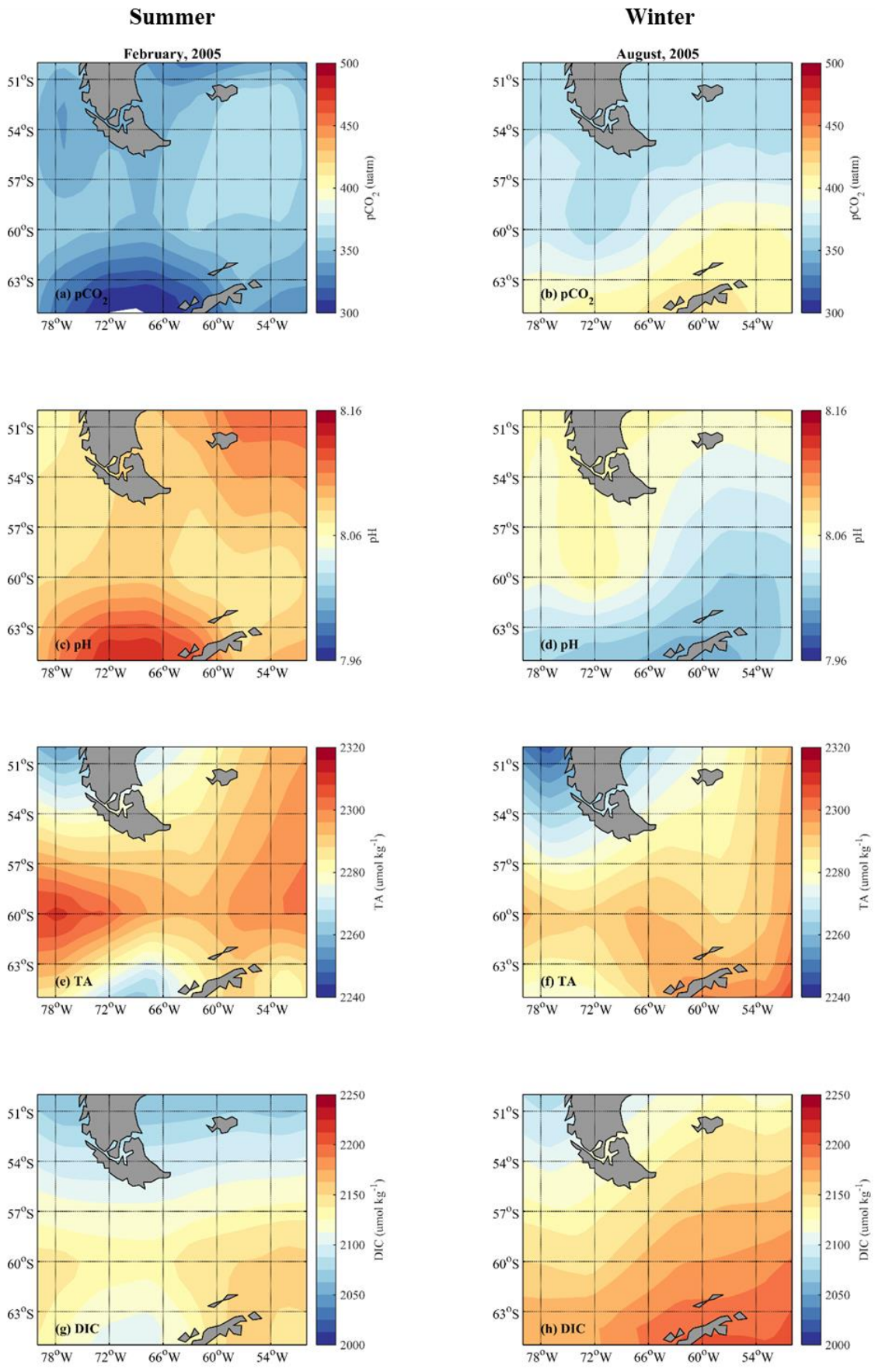
Summer
Winter
February, 2005
August, 2005
(a) pCO2
(b) pCO2
(c) pH
(d) pH
(e) TA
(f) TA
(g) DIC
(h) DIC
pCO2 (uatm)
pH
TA (umol kg-1)
DIC (umol kg-1)
51°S
54°S
57°S
60°S
63°S
78°W
72°W
66°W
60°W
54°W
500
450
400
350
300
8.16
8.06
7.96
2320
2300
2280
2260
2240
2250
2200
2150
2100
2050
2000

Figure 5.3. Climatological mean distributions of (a, b) pCO_2, (c, d) TA, (e, f) pH and (g, h) DIC in the Drake Passage normalized to year 2005. Summer distributions (February) are shown on the left, winter (August) at the right. The values of these parameters are based upon T14 (Takahashi et al., 2014).

5.3.2 Surface pCO_2 seasonal cycle in the Drake Passage

Figure 5.4 shows the seasonal variation of surface ΔpCO_2 (sea surface pCO_2 minus atmospheric pCO_2) from R1 to R4 (Fig. 5.1) based on the Drake Passage Time-series dataset. Overall the region acts as a weak sink of CO_2 from the atmosphere, with R1 and R2 being a near neutral region, and R3 and R4 being a sink region. The maximum of surface ocean pCO_2 was often reached in austral winter, when upward transport of deep water brings CO_2-rich water to the surface, and the minimum was mostly observed in austral summer, when biological production draws down the surface CO_2 level (Takahashi et al., 2009). The seasonal amplitude of ΔpCO_2 is generally less than 35 µatm throughout DP, in agreement with the comprehensive study of surface pCO_2 in DP carried out by Fay et al. (2018).

However, a significant disagreement between the time-series observations and SOCCOM floats observations is found with respect to the magnitude of ΔpCO_2 in regions south of the APF. The magnitude of ΔpCO_2 in R4 only reached as large as positive 15 ± 10 µatm in winter, which is far less than the substantial CO_2 outgassing (around positive 34 µatm; Williams et al., 2017; Williams et al., 2018) suggested by the SOCCOM estimation.

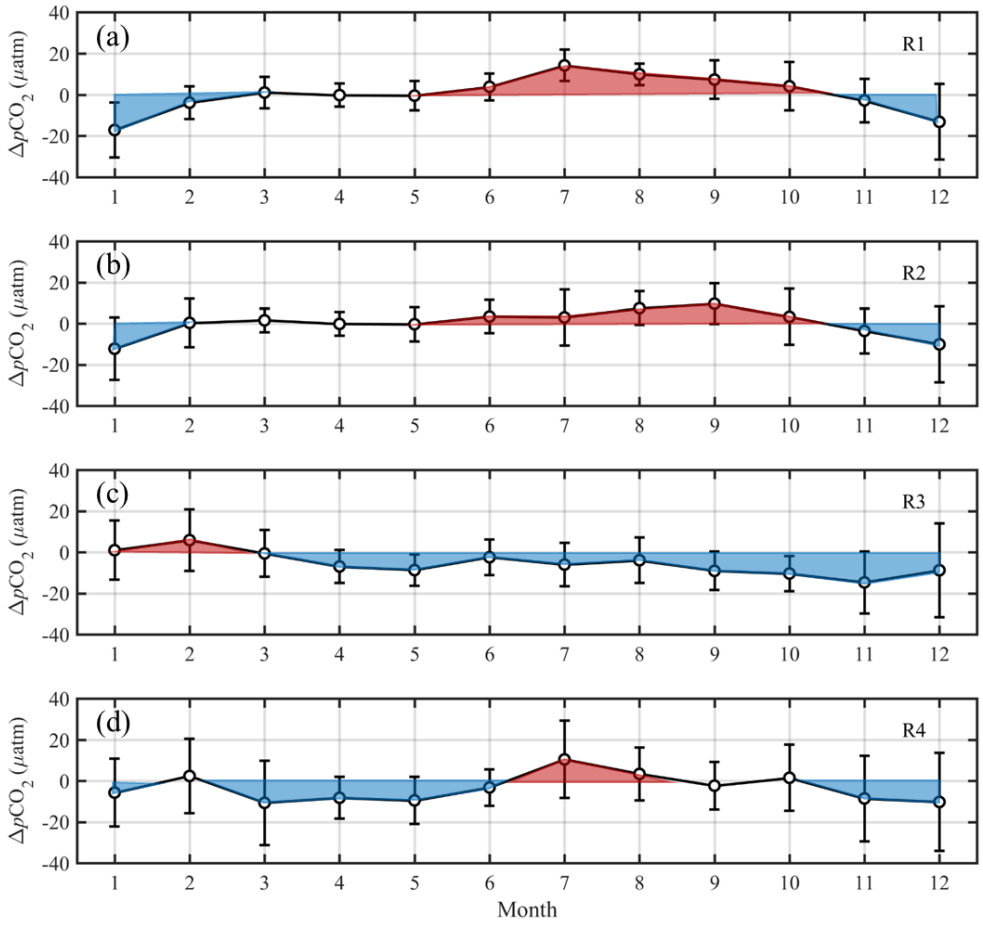

Figure 5.4. The monthly variations of surface ΔpCO_2 (difference between the sea surface pCO_2 and atmospheric pCO_2) in each region of the Drake Passage. The circles represent the average ΔpCO_2 values in each month, and the error bars represent the standard deviations. Blue shading represents CO_2 sink to the ocean, and red shading represents CO_2 source to the atmosphere. Data from the Drake Passage Time-series dataset.

5.3.3 Surface carbon balance calculation

Tracer values from Table 5.1 were applied to Equations 5.1 and 5.2 to estimate the fractions of AAWW and SSW present in surface water. Since DIC is conservative during the mixing process, I calculated the concentrations of 'mixed' DIC in WSW from mixing of AAWW and SSW using Equation 5.2. However, pCO_2 is not conservative during the mixing process; the values of 'mixed' pCO_2 in WSW were therefore calculated from the carbonate system with the inputs of 'mixed' TA and 'mixed' DIC, using CO_2SYS (Van Heuven et al., 2011; see Section 2.2.3 for selection of dissociation constants).

Using TA as a tracer results in calculated fractions of AAWW=14% and SSW=86%. Calculating DIC with these fractions results in DIC=2139 µmol kg^{-1} and pCO_2=307 µatm, both of which are less than the observed DIC and pCO_2 levels in the WSW at the reference year. Using salinity as a tracer results in calculated fractions of AAWW = 48% and SSW = 52%, leading to DIC=2153 µmol kg^{-1} and pCO_2=337 µatm, still less than the observed levels in the WSW at the reference year.

Although the estimated DIC and pCO_2 of surface water due to winter entrainment exhibit large differences depending on which tracer is used to calculate the mixing proportions, they both suggest lower levels of DIC and pCO_2 than their observed values in the WSW. The physically 'mixed' pCO_2 resulting from winter entrainment of CO_2-rich water (Table 5.1) is still below the atmospheric level (consistent with Fig. 5.4d); R4 thus remains a CO_2 sink region, which agrees well with the results from Fay et al. (2018) and Munro et al. (2015b) that DP is overall a persistent CO_2 sink in all regions including R1 to R4.

5.3.4 Applying CORS to SOCCOM data

Figure 5.6 shows the results of applying the CORS technique (Chapter 4) to the profiling floats in and near to DP (Fig. 5.5). Six relevant floats were selected for investigating the distributions of ΔO_2 and ΔCO_2 in different oceanographic regimes of the Southern Ocean (as defined in Gray et al. (2018)). Floats F9646 and F9666 were located in the Subantarctic Zone (SAZ), a region with deep winter mixed layers. Float F0569 was located in the Polar Frontal Zone (PFZ), which encompasses the northern part of the Antarctic Circumpolar Current. Floats F12545, F9092, and F9652 were located in the Antarctic-Southern Zone (ASZ), which extends from the Polar Front in the north to the edge of the seasonally ice-covered zone. Both the PFZ and ASZ have colder surface waters and larger nitrate concentrations (greater than 20 µmol kg^{-1}) because of the upwelling in these regions.

Overall, the CORS plots (Fig. 5.6) suggest a predominance of CO_2 undersaturation along with O_2 supersaturation in austral spring and summer, and the reverse in autumn and winter. For those floats further south (e.g., F12545, F9092, and F9652), the undersaturation of O_2 combined with supersaturation of CO_2 in the surface waters becomes stronger in cold seasons, which implies the influence of upwelled deep water with elevated CO_2 and deficient O_2. For F9652 (Fig. 5.6f), significant CO_2 supersaturations (around 6 µmol kg^{-1}) with O_2 undersaturations (around -100 µmol kg^{-1}) were even observed in summer, which has not been found in any of the other floats. A Y-intercept of up to -5 µmol kg^{-1} ΔCO_2 (the Y-intercepts of the fitted curves range from -3.65 to 0.50 µmol kg^{-1}; Fig. 5.10, Table 5.2) was found in most of the floats, which suggests disproportional

changes in ΔO_2 and ΔCO_2. However, this Y-intercept was barely observed in the surface waters based on the GLODAPv2 dataset (see Chapter 4, Fig. 4.2, Fig. 4.3, and Table 5.2), where ΔCO_2 vs. ΔO_2 tends to cross the Y-axis very close to the origin.

Figure 5.7 extends the application of CORS to the wider Southern Ocean, with F9031 located in the SAZ, F9265 in the PFZ, F9096 in the ASZ, and F9099 in the Seasonal Ice Zone (SIZ) where coldest surface waters and largest seasonal salinity changes are found. The distributions of ΔO_2 and ΔCO_2 generally fell close to the origin in the SAZ region (Fig. 5.7a); however, large variations in CORS were found by F9099 (Fig. 5.7d), the float which has been repeatedly reported and discussed by previous studies (Gray et al., 2018; Williams et al., 2017; Williams et al., 2018). F9099 exhibited regular changes in ΔO_2 and ΔCO_2 in the second quadrant; however, the scatterplot does not intersect near to the coordinate origin, an X-intercept of -38 µmol kg^{-1} ΔO_2 was found (i.e., O_2 was undersaturated by 30 µmol kg-1 where CO_2 was in equilibrium with the atmosphere) and the largest Y-intercept among all relevant floats in this Chapter of -3.65 µmol kg^{-1} ΔCO_2 was found (Fig. 5.10, Table 5.2).

It is also noteworthy that CORS plots are capable of distinguishing suspect data from credible data (quality-controlled data). Fig. 5.8 shows a comparison between unfiltered and filtered data (data flag 0 = ”good”) from F9096. The unfiltered data (Fig. 5.8a) in the CORS plot show abnormally high (up to 20 µmol kg^{-1}) and varying ΔCO_2 with respect to a certain and small ΔO_2 range in each season; this is significantly different from the general pattern of CORS distribution in the Southern Ocean (see Fig. 4.2 and Fig. 4.4). The ratio between the changes in ΔO_2 and ΔCO_2 (in the second quadrant) is not consistent with respiration as a cause. A small portion of data in autumn (Fig. 5.8a) were found in the third quadrant with fairly low ΔCO_2 values (around -18 µmol kg^{-1}), which was also beyond the general pattern. Although these data have already been flagged as suspect, CORS plots clearly and immediately show them up as implausible.

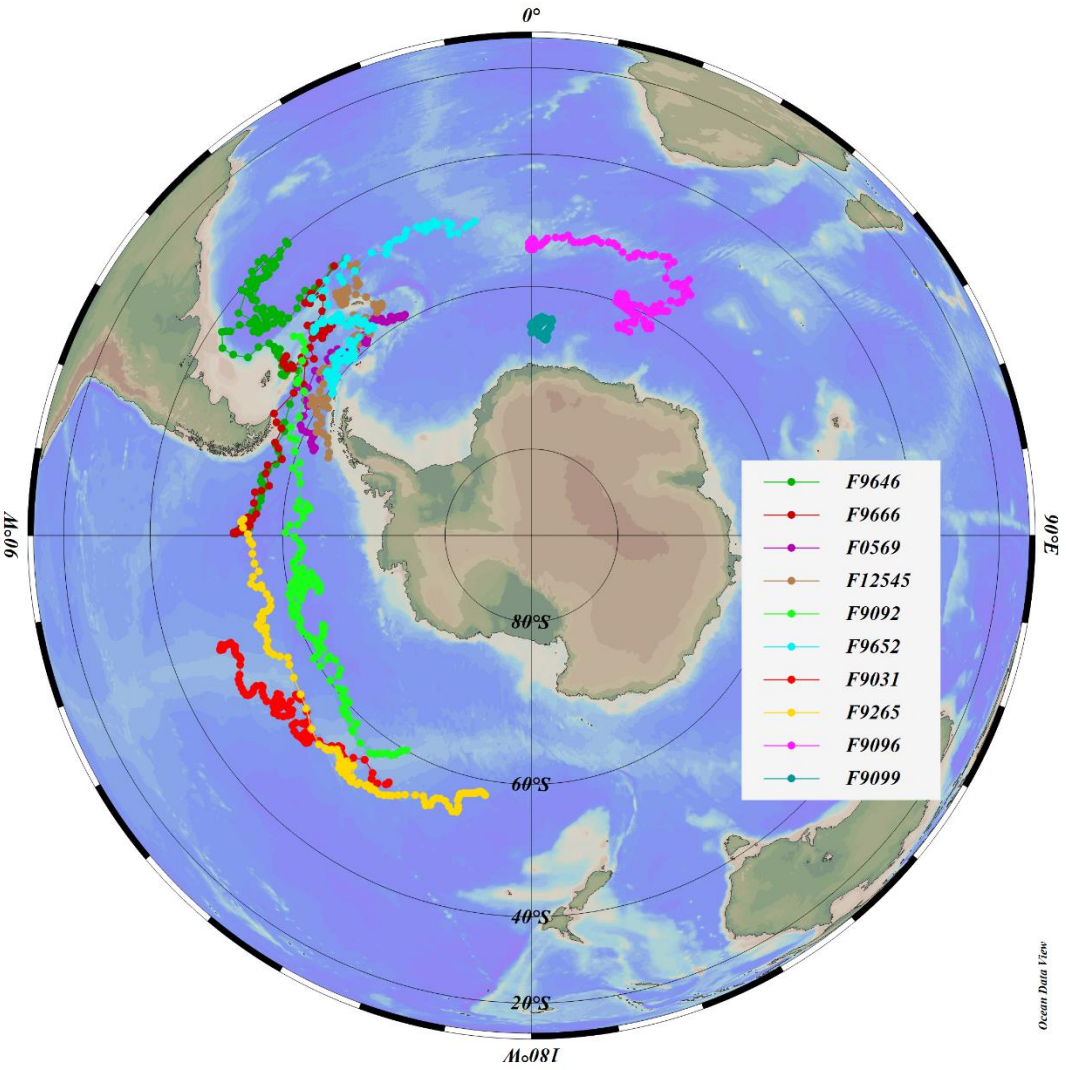

Figure 5.5. A map of 10 relevant float trajectories across and outside Drake Passage included in this study. The top 6 floats listed in the legend box are in and near to DP, and the other 4 floats are outside DP. Background colour shows ocean bathymetry from the ETOPO1 Global Relief dataset. Coloured dots show the time-varying locations of each float, with their UW float ID numbers in the legend box.

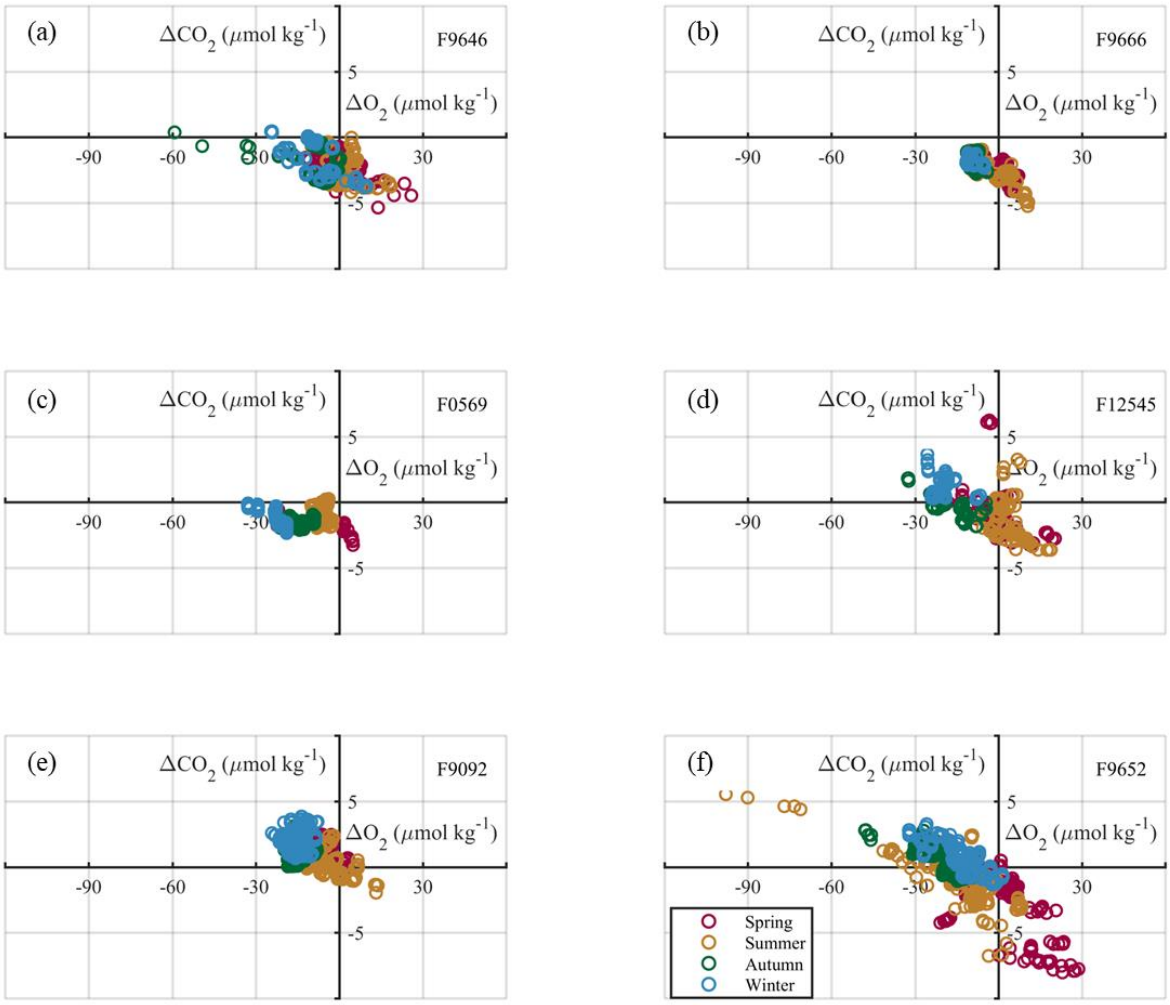

Figure 5.6. CORS plots from data collected by 6 different floats in and relatively near to Drake Passage. Distributions of carbon and oxygen relative to their saturation in the surface water in four seasons. Note the different axis scales for CO_2 and O_2. Colours indicate different seasons: spring (magenta), summer (dark yellow), autumn (green) and winter (blue). The label on the top right of each subplot denotes the UW float ID number.

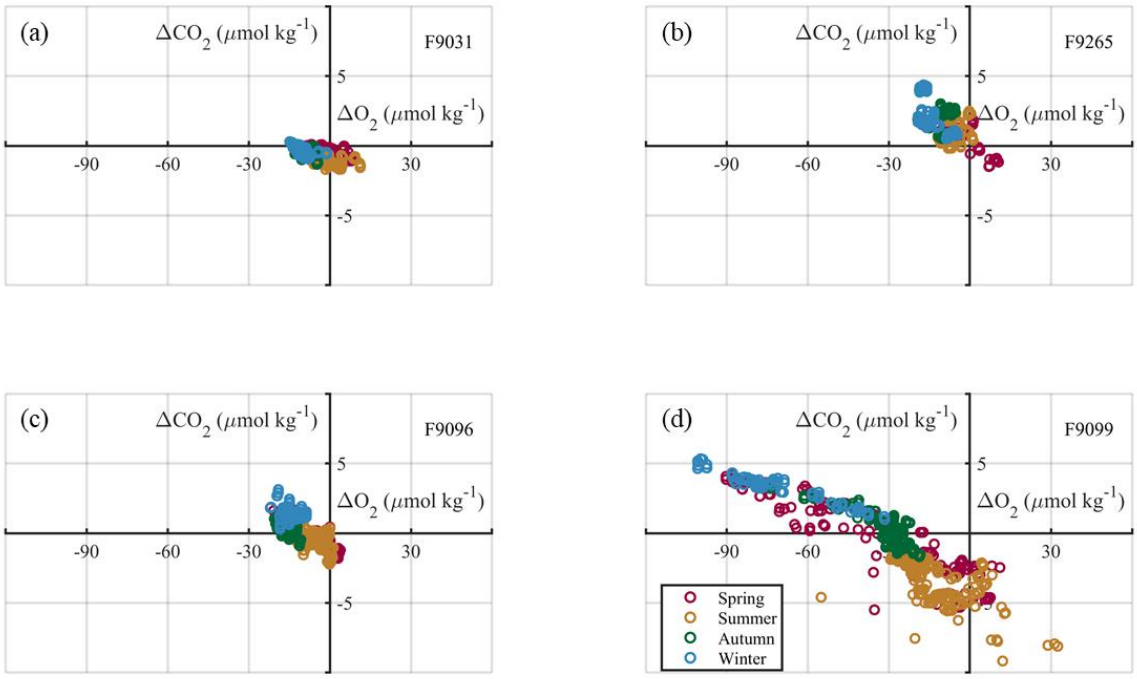

Figure 5.7. CORS plots from data collected by 4 different floats outside Drake Passage. Distributions of carbon and oxygen relative to their saturation in the surface water in four seasons. Note the different axis scales for CO_2 and O_2. Colours indicate different seasons: spring (magenta), summer (dark yellow), autumn (green) and winter (blue). The label on the top right of each subplot denotes the UW float ID number.

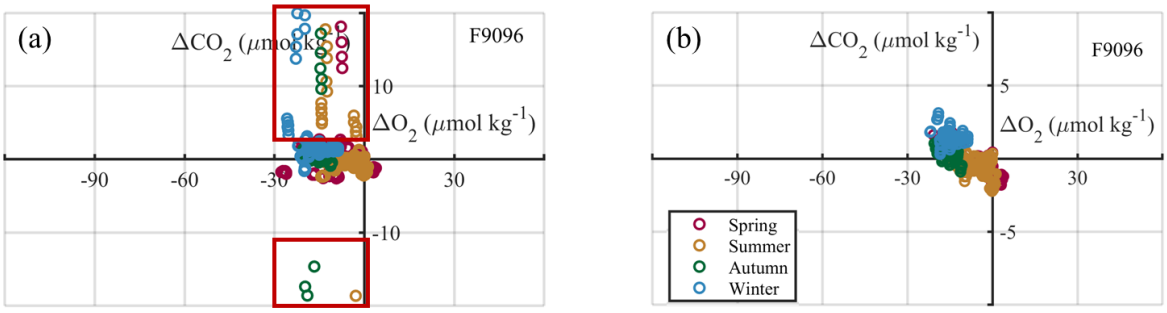

Figure 5.8. Comparison between unfiltered and filtered data (only with data flag = 0) from F9096. Note the different y axis scale between (a) and (b). The red boxes in (a) show the data flagged as suspect.

5.4 Discussion

5.4.1 Comparisons of winter pCO_2, pH, TA and DIC between SOCCOM and climatology

Given that most of the conspicuous features (e.g., strong CO_2 outgassing, large deviations of O_2 and CO_2 in CORS) observed by SOCCOM floats took place in winter, it is therefore useful to evaluate these float-based estimations against an existing climatological product (i.e., T14). For comparison between different sampling years, the floats data are adjusted to the climatological reference year of 2005 according to the reported rates of anthropogenic change in the Southern Ocean (Section 5.2.3). Specifically, pCO_2 and DIC were normalized to year 2005 using mean rates of change of 1.9 µatm year^{-1} and 1.1 µmol kg^{-1} year^{-1}, respectively (Takahashi et al., 2014). In this section, four floats were chosen for comparison with the T14 climatology. In order to be representative, they are taken from the PFZ, ASZ and SIZ regions rather than just one region: F12545 (located in the ASZ) showed reasonable changes in the combination of ΔO_2 and ΔCO_2 (Fig. 5.6d); the deviations of O_2 and CO_2 were smaller than those from the other three floats, and ΔO_2 vs. ΔCO_2 is found to cross both X- and Y-axis very close to the origin. F9652 (located in the PFZ and ASZ at different time) and F9099 (located in the SIZ) show extremely large variations in the combination of ΔO_2 and ΔCO_2 (Fig. 5.6f and Fig. 5.7d). F9099 and F9096 (located in the ASZ) have been the focus of many SOCCOM studies and central to the high-latitude CO_2 source conclusion (e.g., Gray et al., 2018; Williams et al., 2017; Williams et al., 2018; see also Section 5.1).

Figure 5.9 shows the winter distributions of carbonate chemistry parameters from the floats measurements (pH) and estimations (TA, pCO_2, and DIC) superimposed over the background of the T14 climatology. For F9652 and F12545, the estimated pCO_2 agreed well (difference less than 20 µatm) with T14 around the DP region; however, for F9096 and F9099, large discrepancies (up to 70 µatm) from T14 were found outside DP. Discrepancies were found between T14 and floats, especially for regions south of the PFZ and regions outside DP. This phenomenon has been previously reported (Gray et al; 2018; Williams et al., 2017; Williams et al., 2018), and it was attributed partly to the sparse wintertime observations outside DP, as well as the change in Southern Ocean circulation between the T14 climatology (reference year 2005) and 2014-2017: an increase in wind-driven upwelling is thought to have brought more CO_2-rich deep water to the surface (Lovenduski et al., 2008).

The distribution of SOCCOM pH overall mirrored its pCO_2 distribution, because the result of calculated pCO_2 from pH depends mostly on the measured pH rather than on TA (Dickson and Riley, 1978). Discrepancies of up to 0.04 pH units between floats and T14 were found for F12545 at around

40°W, while the other SOCCOM pH values measured by F12545 and F9652 were close to the climatological values at longitudes between 45°W and 60°W. The pH values measured by F9096 and F9099 were, however, less than the T14 pH by a greater magnitude of 0.06 to 0.2. Note that although SOCCOM pH measured by F12545 at 40°W is lower than T14 pH, the SOCCOM pCO_2 at the same area matches the T14 pCO_2 very well: probably due to the higher SOCCOM TA (Fig. 5.9c), with which SOCCOM pCO_2 was calculated.

The SOCCOM-estimated TA differed significantly from the T14-estimated TA, because of different empirical methods: the T14 TA was derived from a potential alkalinity (PALK)-salinity relationship (Takahashi et al., 2014), and the SOCCOM TA was derived using the LIAR algorithm (Carter et al., 2018) relying on float-measured temperature, salinity, pressure, oxygen, and location. Consequently, large discrepancies were seen between the SOCCOM-estimated DIC and T14 DIC: the accuracy of calculated DIC from pH or pCO_2 relies more on the accuracy of the TA estimate (Dickson and Riley, 1978); that is to say, the bias in estimated DIC between these two datasets actually results from a bias in TA.

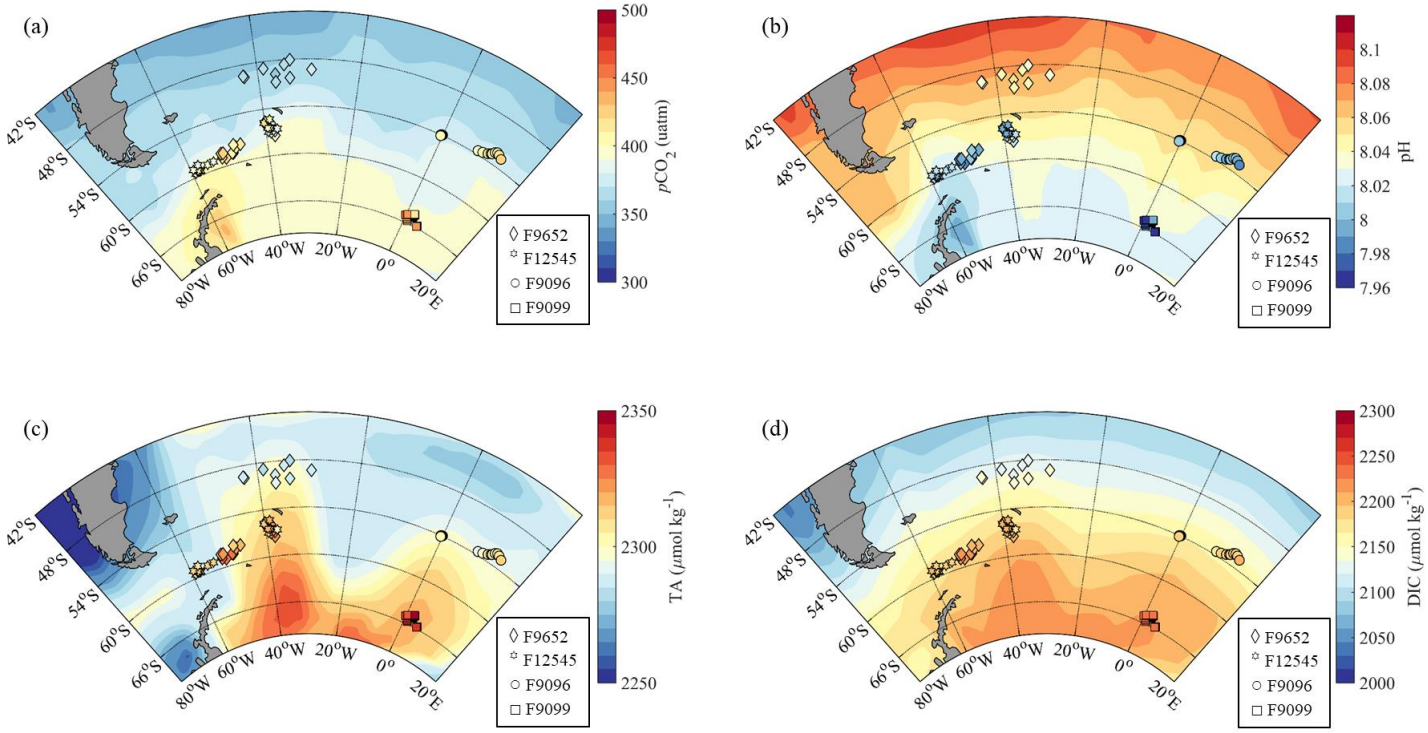

Figure 5.9. Comparisons between the SOCCOM-estimated (symbols) (a) pCO_2, (b) pH, (c) TA, and (d) DIC and Takahashi et al. (2014) climatologies (background) in the Southern Ocean in winter months (July to September). Floats F9652, F12545, F9096, and F9099 are selected for comparison, with float data normalized to year 2005. The Takahashi 2014 climatology is also normalized to year 2005.

5.4.2 Is the winter CO_2 source in the high-latitude Southern Ocean real?

Our results challenge the finding (Gray et al., 2018; Williams et al., 2017) of strong CO_2 outgassing in the high-latitude Southern Ocean (i.e., PFZ and ASZ); our results (Fig. 5.4 and Section 5.3.3) imply that DP is a nearly neutral oceanic sink/source for CO_2. It seems unlikely that winter entrainment of AAWW into DP surface water could produce the magnitude of surface water ΔpCO_2 (compared to the atmosphere) of as large as 40 µatm as suggested by the SOCCOM floats pCO_2 estimates in winter (Williams et al., 2017). Even if I took the Upper Circumpolar Deep Water (UCDW) into consideration of the seasonal formation of the surface water in winter as an extreme situation (i.e., UCDW mixes with SSW to form WSW), the results still yielded a lower pCO_2 (pCO_2 in the 'mixed' water mass from UCDW and SSW ranges between 310 and 330 µatm, with proportion of UCDW ranging from 6% to 14% depending on which tracer is used) than the atmospheric level (around 365 µatm in year 2005). Both the observed surface water pCO_2 seasonal cycle and the carbon balance calculation suggest that it is implausible for DP to have a strong CO_2 outgassing in winter. This is in line with Fig. 5.9 that large discrepancies in float-estimated pCO_2 were only found in areas outside DP.

However, it is difficult to evaluate the possibility of strong CO_2 outgassing outside DP because of the lack of data, particularly in winter. Gray et al. (2018) and Williams et al. (2018) attributed the increases in the carbon and nutrient content of surface waters in the high-latitude Southern Ocean primarily to interannual variability – they suggested that a positive Southern Ocean Annular Mode Index over 2014-2017 resulted in increased wind-driven upwelling (Lovenduski et al., 2008; Lovenduski et al., 2007). The discrepancy between SOCCOM pCO_2 and that from the T14 climatology could also be due to specific locations sampled (floats and ship observations not exactly coincident/synchronous) or specific events (e.g., phytoplankton blooms) occurred during the float measurements as reported by Fay et al. (2018).

5.4.3 What do the CORS offsets tell us?

I now consider what the CORS analysis suggests about the validity of the SOCCOM float-estimated high winter-time pCO_2.

Figure 5.10 and Table 5.2 synthesizes the CORS distributions of the floats discussed above, the CORS plots of most floats in the Southern Ocean are found to exhibit an offset when crossing the X or Y-axis, which is contradictory to the inset to Fig. 4.2 (Chapter 4): various processes tend to drive the concentrations of surface O_2 and CO_2 away from equilibrium (the coordinate origin) with

the atmosphere, and tend to return concentrations towards the origin. Neither theory nor GLODAPv2 data (Table 5.2) lead to an expectation of non-zero Y-intercepts.

Among the floats, only the CORS plots from F12545, F9092, F9031, F9265, and F9096 show good agreement with the general pattern (Fig. 4.2 and Fig. 4.4 in Chapter 4, based on the GLODAPv2 dataset) i.e., intersects near to the coordinate origin. All the other floats (Table 5.2) have X-intercepts of from -10 to -30 µmol kg^{-1} in ΔO_2, and Y-intercepts ranging from -3.65 to -1.01 µmol kg^{-1} in ΔCO_2. Due to the fact that oxygen sensors are more stable, precise and accurate (Johnson et al., 2017; see also description in Section 5.2.2) than pH sensors from which the carbonate system was calculated, the CORS analyses above would seem to suggest that the offsets of intercepts are more likely to result from the pH sensor errors/biases.

The offset in ΔCO_2 translates to a pCO_2 difference according to the solubility of CO_2:

$$K_H = [CO_2]/pCO_2 \quad (5.3)$$

where K_H is the Henry's constant for CO_2, representing the solubility of CO_2), which can be rearranged into

$$pCO_2 = [CO_2]/K_H \quad (5.4)$$

For an average sea surface temperature of 1°C in the Southern Ocean, $1/K_H$ approximates 16 in units of µatm (µmol $kg^{-1})^{-1}$ (Zeebe and Wolf-Gladrow, 2001). Therefore, at 1°C, an offset in ΔCO_2 of -3.65 µmol kg^{-1} equates to a difference in pCO_2 of 58 µatm. The X- and Y-intercept offsets could be due to systematic biases in either the O_2 measurements or the pCO_2 estimations from pH and TA (more likely in the pCO_2 estimations from pH). By correcting the bias, it would make up to 60 µatm difference to pCO_2 (Table 5.2), which means that, for some of the floats where systematic biases are applicable, the corrected pCO_2 values would be up to 60 µatm higher than previously estimated.

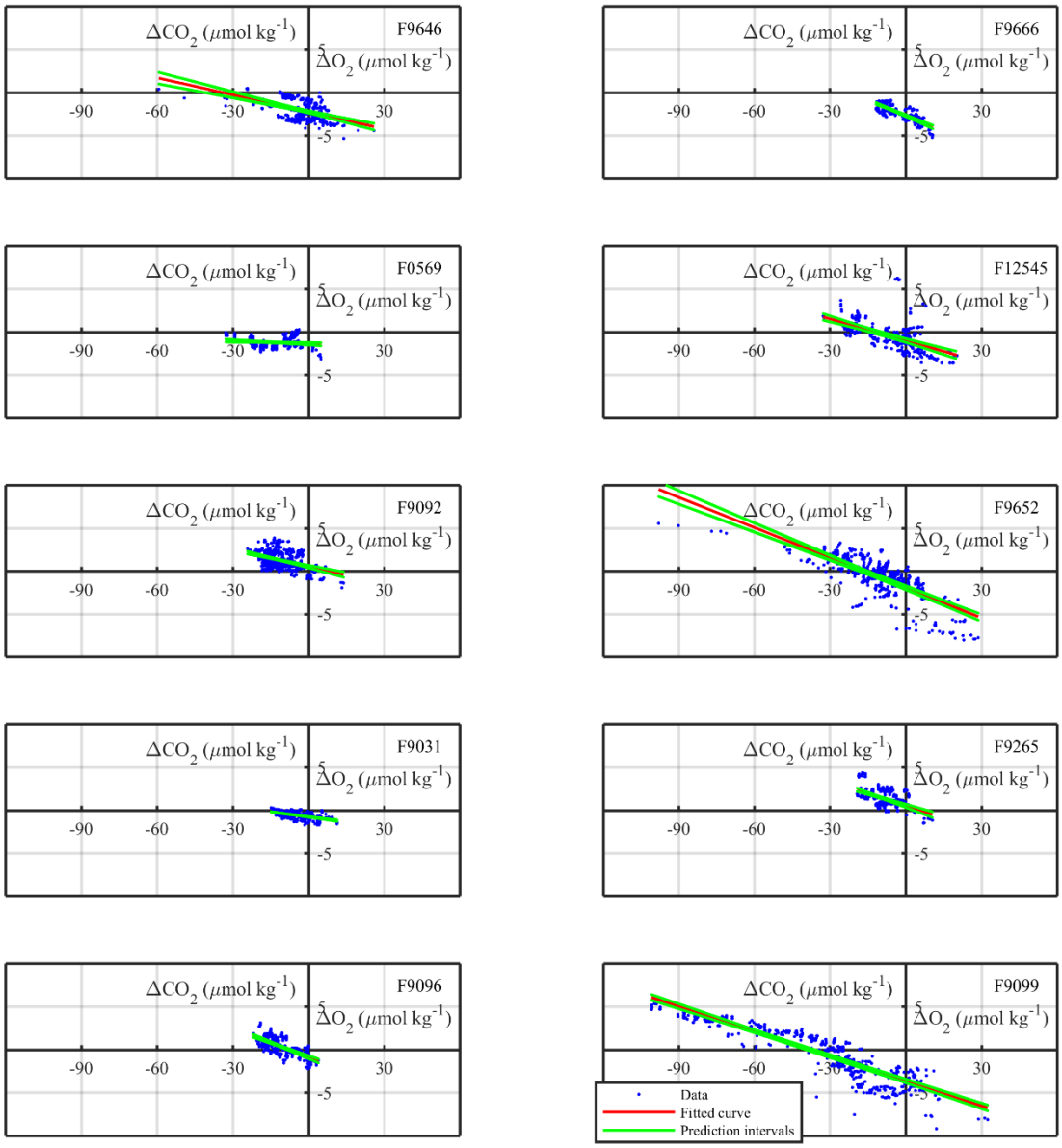

Figure 5.10. CORS plots from data collected by the 10 relevant floats in and near to Drake Passage. Distributions of carbon and oxygen relative to their saturation in the surface water. Data values are displayed by blue dots. Red lines are the least-squares best-fit straight lines; green lines are the 95% confidence bounds for the fitted coefficients (more detail in Table 5.2). The label on the top right of each subplot denotes the UW float ID number.

Table 5.2. Statistical analysis of fitted lines to the CORS plots from data collected by the 10 relevant floats in and near to Drake Passage, together with statistics from the GLODAPv2 database. The fourth column converts the offsets in Y-intercept (μmol kg^{-1}) to differences in pCO_2 (μatm) for average sea surface temperature of 1°C.

Float ID number	Fitted curve: Y = p1 × X + p2 (with 95% confidence bounds)		pCO_2 difference (μatm) corresponding to p2 offset
	p1	p2	
F9646	-0.066 (-0.076, -0.056)	-2.26 (-2.34, -2.17)	-36
F9666	-0.122 (-0.132, -0.112)	-2.71 (-2.78, -2.63)	-43
F0569	-0.011 (-0.018, -0.005)	-1.38 (-1.50, -1.27)	-22
F12545	-0.084 (-0.095, -0.072)	-1.01 (-1.17, -0.84)	-16
F9092	-0.067 (-0.077, -0.057)	0.50 (0.38, 0.63)	8
F9652	-0.117 (-0.125, -0.109)	-1.96 (-2.10, -1.82)	-31
F9031	-0.039 (-0.043, -0.035)	-0.78 (-0.82, -0.75)	-12
F9265	-0.097 (-0.110, -0.083)	0.50 (0.36, 0.64)	8
F9096	-0.112 (-0.124, -0.101)	-0.89 (-1.03, -0.74)	-14
F9099	-0.096 (-0.100, -0.093)	-3.65 (-3.82, -3.48)	-58
GLODAPv2-based			
Pacific Ocean data in spring (Fig. 4.3a)	-0.113 (-0.119, -0.107)	1.21 (0.89, 1.54)	19
Atlantic Ocean data in spring (Fig. 4.3a)	-0.151 (-0.158, -0.143)	-0.29 (-0.44, -0.15)	5
Southern Ocean data in winter (Fig. 4.3c)	-0.023 (-0.025, -0.021)	0.25 (0.14, 0.33)	4

5.5 Conclusions

By taking advantage of the Drake Passage Time-series data and the surface carbon balance calculation, I suggest the implausibility of significantly strong CO_2 outgassing in winter in the Drake Passage. This challenges the novel finding (from SOCCOM float data) that the high-latitude Southern Ocean is a massive CO_2 source in winter (Gray et al., 2018). The winter entrainment of CO_2-rich deep water has a limited impact on elevating the surface pCO_2 in Drake Passage. However, care should be taken in extrapolating this result to the broader Southern Ocean outside of Drake Passage due to the lack of observational data: a comprehensive understanding of the Southern Ocean CO_2 source/sink requires more observations with improved accuracy and temporal- and spatial-coverage.

This study also applied the CORS technique to float-measured/estimated O_2 and CO_2 data. The CORS distribution is capable of distinguishing suspect data from credible data, and thus validating the sensor performance. The X- and Y-intercept offsets are presumed to be primarily associated with the pH sensor biases; it would seem that these are associated with underestimations of float-estimated pCO_2 of as large as 60 µatm.

Finally, it is not within the scope of this chapter to discuss the procedure of data quality control and assessment of the SOCCOM float data, but I do suggest the possibility of previously undiscovered sensor errors.

Chapter 6 Conclusions and implications

This chapter draws together the major findings of this thesis, and suggests the pending questions raised and future work where these findings might be applied.

6.1 Overview of thesis

In Chapter 1, I introduced and summarized the carbon cycle and past researches into the marine carbonate system (especially in terms of DIC and aqueous CO_2) and dissolved oxygen in the surface open ocean. Due to the fact that the surface ocean links the atmosphere and the deep ocean, it therefore plays a vital role in the global carbon cycle. The importance of high-latitude oceans (especially the Southern Ocean) in regulating the distributions of CO_2 and O_2 in the surface ocean was also explained. In Chapter 2, I described the main datasets used in this thesis, as well as the common data processing methods used in the following chapters. In Chapter 3, I investigated the controls on the latitudinal gradient in open-ocean surface DIC and emphasized the importance of upwelling in the Southern Ocean. In Chapter 4, I developed a technique called CORS to investigate the distributions and controls on dissolved CO_2 and O_2 across the global surface ocean. In Chapter 5, I revisited the carbon cycle in the Drake Passage using two independent approaches, aiming to test the truth of the significant winter CO_2 outgassing in the high-latitude Southern Ocean, as suggested by the SOCCOM biogeochemical float data. I also used the CORS technique to examine the validity of the float data.

6.2 Towards a better understanding of the role of upwelling on the carbonate system

To investigate the drivers of observed latitudinal gradients in surface nDIC (Chapter 3), I used the GLODAPv2 database to test three hypotheses: (1) sea surface temperature driven effect; (2) salinity-related TA driven effect; and (3) high latitude upwelling of DIC- and TA-rich deep waters driven effect. Upon quantifying the relative importance of these three drivers, I found that no single mechanism can actually explain the full amplitude of surface DIC and nDIC latitudinal variation, but temperature seems to contribute the majority (Fig. 6.1). However, I also surprisingly found that upwelling-driven effects account for a sizable part, ranging from 74 to 220 of the 223 μmol kg^{-1} depending on which time scale is based upon. This finding sheds light on the importance

of upwelling in shaping the global surface DIC spatial pattern, which has never been appreciated in any of the previous studies, and thus may be of great significance in future studies.

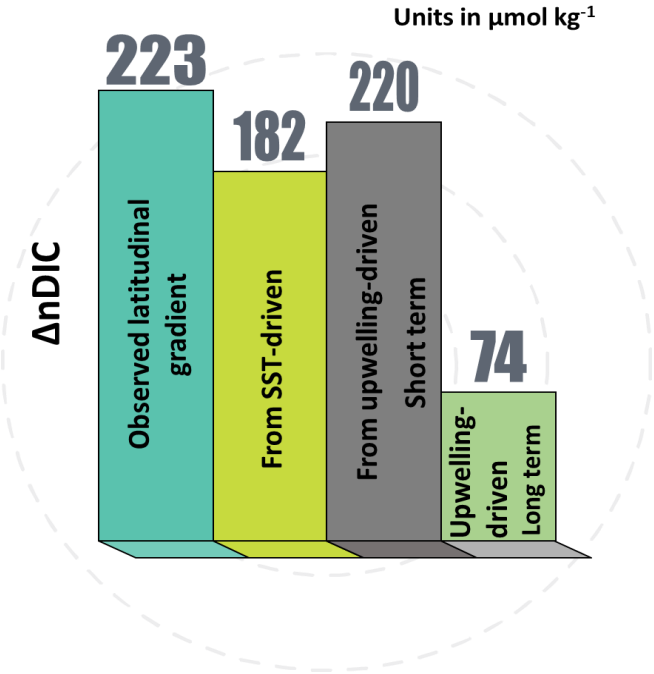

Figure 6.1. The contributions of SST-, short-term effect of upwelling-, and long-term effect of upwelling-driven effect on the latitudinal gradient of nDIC in the Southern Ocean. Number above the histogram shows the magnitude of each effect.

By taking the Southern Ocean as an instance to study the impact of high-latitude upwelling, I concluded that two effects from upwelling have to be considered: the short-term and long-term effects (Fig. 6.2). The short-term effect of upwelling works immediately in the upwelled deep waters, and it is likely to be most significant in the vicinity of where upwelling takes place. The short-term effect usually lasts over a timescale of weeks to months (Jones et al., 2014; Fig. 6.2), and creates a large impact on the observed latitudinal gradient of ΔnDIC (Fig. 6.1). However, this contribution is reduced by about two-thirds if the long-term effect of upwelling is considered (Fig. 6.1), which is usually more important for areas further away from locations of upwelling. The long-term effect of upwelling is driven by CO_2 air-sea gas exchange as it moves the surface ocean to a new carbonate system equilibrium with respect to the addition of TA from deep waters. The long-term effect usually dominates on timescales longer than months to a year (beyond the CO_2 gas exchange re-equilibrium timescale; Jones et al., 2014; Fig. 6.2), and the magnitude of this effect explains the shortfall between ΔnDIC and $\Delta nDIC_{temp}$ (Fig. 6.1).

The analysis of the comparison of nDIC in the North Atlantic and North Pacific (Section 3.4.3) also confirmed the important contribution of high-latitude upwelling to ΔnDIC.

In order to improve understanding of the role of upwelling at high latitudes on the surface DIC concentration, future efforts (both observational-based analysis and model simulation) need to be made to better constrain the two routes identified in Chapter 3 by which upwelling affects surface DIC on different timescales. The previous view (e.g., Takahashi et al., 2014) that upwelling elevates surface DIC solely or mainly through the introduction of high-DIC water may need revision.

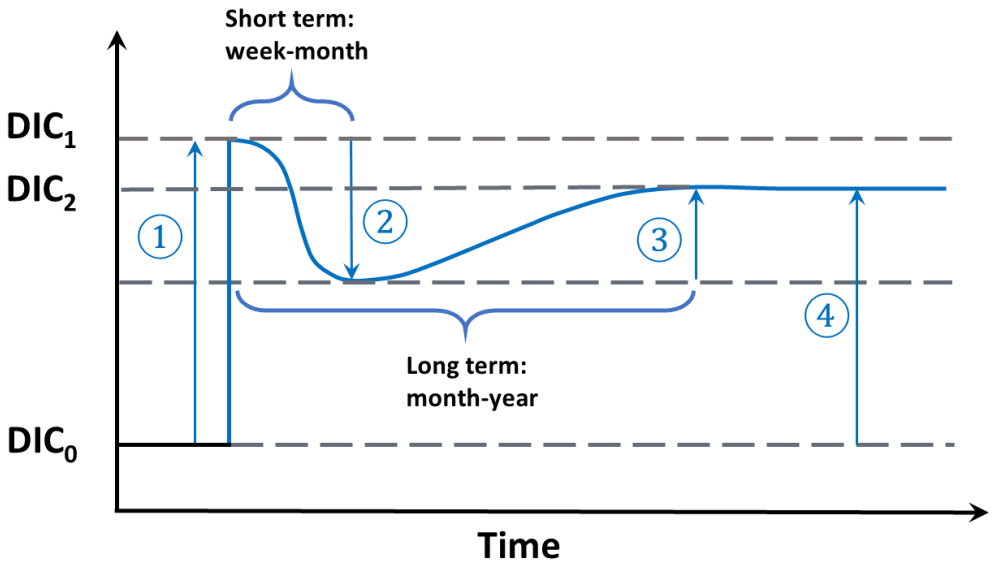

Figure 6.2. A schematic illustrating the short-term and long-term effects of upwelling on surface DIC.

Numbers represent processes changing surface DIC, and arrows point in the direction of change: ①: upwelling and supply of CO_2-rich deep waters; ②: DIC uptake by biology. The processes of ① and ② together make up the short-term effect of upwelling; ③: the change brought about by air-sea CO_2 gas exchange; ④: the long-term impact of upwelling after the third stage (③). Note that this is a simplified version of Fig. 3.6.

6.3 Towards a more straightforward illustration of coupled changes in dissolved gases CO_2 and O_2

After recognizing the importance of upwelling in the Southern Ocean, I then looked into the relationship between dissolved CO_2 and dissolved O_2 in this region, which are biologically linked due to primary production, respiration and remineralization. Previous studies have not compared the concentrations of [CO_2] and [O_2] in the same way as here. By doing this, I aimed to create a useful tool that could be applied to investigate different biogeochemical processes affecting

dissolved CO_2 and O_2 (inset to Fig. 4.2d), just like the TA-DIC diagram (Fig. 6.3) that is capable of tracing different biogeochemical processes using the ratio between changes in TA and DIC (Humphreys et al., 2018; Zeebe, 2012). I adopted a related method to that shown in Fig. 6.3, but one which instead considered impacts of processes on $[CO_2]$ and $[O_2]$ rather than on concentrations of DIC and TA. I used CORS plots of data on CO_2 and O_2 axes to work out which processes were driving the patterns seen in the observations.

By applying the new technique – CORS – to the GLODAPv2 dataset (Chapter 4), I investigated the co-variation of CO_2 and O_2 in the surface seawater and their deviations from equilibrium with the atmosphere. Large seasonal deviations of $[CO_2]$ and $[O_2]$ from their equilibrium values were found on the global scale, and three outstanding features of particular interest were studied. Possible explanations for the deviations in CORS were given by comparing observed slopes in $\Delta[CO_2]$ vs. $\Delta[O_2]$ to the stoichiometric ratio of different processes: phytoplankton blooms in spring were identified as the dominant factor driving the undersaturation of CO_2 and supersaturation of O_2 in the North Atlantic and the subarctic Pacific Ocean; upwelling in winter was identified as the cause of supersaturation of CO_2 and undersaturation of O_2 in the Southern Ocean; ice melting in summer seemed to partly contribute to the simultaneous undersaturation of CO_2 and O_2 in the Southern Ocean, however, as yet no robust explanation could be made regarding this phenomenon.

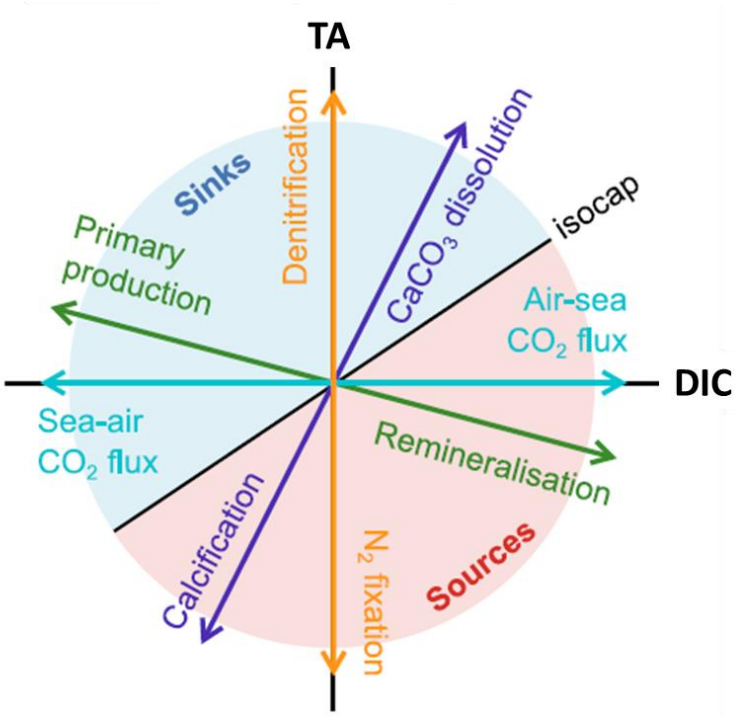

Figure 6.3. Schematic trajectories of the influence of biogeochemical processes on changes in TA and DIC. Figure modified from Humphreys et al. (2018). The blue and red shadings represent a CO_2 sink region (processes which increase pCO_2), and a CO_2 source region (processes which

decrease pCO_2), respectively. The slopes (TA:DIC) for different trajectories are: primary production and remineralisation: -17:106; $CaCO_3$ dissolution and calcification: 2:1; air-sea CO_2 exchange has no impacts on TA; N_2 fixation and denitrification have no impacts on DIC.

6.4 Towards a more cautious view of the SOCCOM float-suggested CO_2 source in the high-latitude Southern Ocean

In Chapter 5, I took advantage of the Drake Passage Time-series data to examine the feasibility of strong CO_2 outgassing in the high-latitude Southern Ocean suggested by SOCCOM float data. I applied an observational-based method (based on the seasonal variation of ΔpCO_2 in the Drake Passage) as well as a surface carbon balance calculation (based on the seasonal formation of water masses in the Drake Passage) to test if the strong winter CO_2 source is real. To my surprise, both results suggested the implausibility of strong CO_2 outgassing in winter in the Drake Passage. However, although the results were in contradiction to the float estimation, I still could not extrapolate this result (in and near to Drake Passage) to regions outside Drake Passage in the Southern Ocean because of the limitation of data availability in the broader Southern Ocean. I suggested that the SOCCOM finding should be treated with caution due to the associated uncertainty and more observations are required to understand this under-observed region of the open ocean.

6.5 Towards a more reliable utility in analysis and validation of autonomously-collected data

As a follow up to the development of CORS technique in Chapter 4, I then applied CORS to SOCCOM float-measured/estimated O_2 and CO_2 data in Chapter 5. Ten relevant floats in the Southern Ocean were selected to investigate the distribution of ΔO_2 and ΔCO_2. The CORS plot of the float data appeared to show the capability of CORS analysis to pick out erroneous float data.

Moreover, an “intercept issue” was found for most of the floats. A relatively large offset of either X- or Y-intercept appeared (Fig. 5.10) in the float data, which was not found in the GLODAPv2 dataset. Since the oxygen sensors have been developed and in use for longer, and are reported to be more stable, precise, and accurate (Johnson et al., 2017) than the pH sensors, these offsets seem most likely to be attributed to biases in the pH sensor measurements. If any corrections are applied due to the offset of Y-intercept, it would create differences in the float-estimated pCO_2 ranging from -8 to 58 µatm (Table 5.2).

Future work is required to make CORS a robust tool and to develop its potential for calibration/correction/screening of autonomously-collected data. It would also be useful to produce CORS plots of data from other independent databases as a check on the CORS plots from the GLODAPv2 database. One possible implication of doing this might be to see if the X- and Y-intercept offsets seen in the float data are also missing from other databases, as they seem to be from the GLODAPv2 database.

References

Anderson, L. A., & Sarmiento, J. L. (1994). Redfield ratios of remineralization determined by nutrient data analysis. *Global Biogeochemical Cycles, 8*(1), 65-80. doi: 10.1029/93GB03318

Assmy, P., Smetacek, V., Montresor, M., Klaas, C., Henjes, J., Strass, V. H., . . . Wolf-Gladrow, D. (2013). Thick-shelled, grazer-protected diatoms decouple ocean carbon and silicon cycles in the iron-limited Antarctic Circumpolar Current. *Proceedings of the National Academy of Sciences, 110*(51), 20633-20638. doi: 10.1073/pnas.1309345110

Bakun, A. (1990). Global climate change and intensification of coastal ocean upwelling. *Science, 247*(4939), 198-201. doi: 10.1126/science.247.4939.198

Balch, W. M., Bates, N. R., Lam, P. J., Twining, B. S., Rosengard, S. Z., Bowler, B. C., . . . Rauschenberg, S. (2016). Factors regulating the Great Calcite Belt in the Southern Ocean and its biogeochemical significance. *Global Biogeochemical Cycles, 30*(8), 1124-1144. doi: 10.1002/2016GB005414

Barton, E. D., Field, D. B., & Roy, C. (2013). Canary current upwelling: More or less? *Progress in Oceanography, 116*, 167-178. doi: 10.1016/j.pocean.2013.07.007

Bates, N., Astor, Y., Church, M., Currie, K., Dore, J., Gonaález-Dávila, M., . . . Santa-Casiano, M. (2014). A time-series view of changing ocean chemistry due to ocean uptake of anthropogenic CO_2 and ocean acidification. *Oceanography, 27*(1), 126-141.

Bates, N. R. (2012). Multi-decadal uptake of carbon dioxide into subtropical mode water of the North Atlantic Ocean. *Biogeosciences, 9*(7), 2649-2659. doi: 10.5194/bg-9-2649-2012

Bates, N. R., Knap, A. H., & Michaels, A. F. (1998a). Contribution of hurricanes to local and global estimates of air–sea exchange of CO_2. *Nature, 395*, 58. doi: 10.1038/25703

Bates, N. R., Michaels, A. F., & Knap, A. H. (1996). Seasonal and interannual variability of oceanic carbon dioxide species at the U.S. JGOFS Bermuda Atlantic Time-series Study (BATS) site. *Deep Sea Research Part II: Topical Studies in Oceanography, 43*(2), 347-383. doi: 10.1016/0967-0645(95)00093-3

Bates, N. R., Takahashi, T., Chipman, D. W., & Knap, A. H. (1998b). Variability of pCO_2 on diel to seasonal timescales in the Sargasso Sea near Bermuda. *Journal of Geophysical Research: Oceans (1978–2012), 103*(C8), 15567-15585.

Boyd, P. W., Watson, A. J., Law, C. S., Abraham, E. R., Trull, T., Murdoch, R., . . . Zeldis, J. (2000). A mesoscale phytoplankton bloom in the polar Southern Ocean stimulated by iron fertilization. *Nature, 407*, 695-702. doi: 10.1038/35037500

Boyer, T.P., Antonov, J. I., Baranova, O. K., Coleman, C., Garcia, H. E., Grodsky, A., Johnson, D. R., Locarnini, R. A., Mishonov, A. V., O'Brien, T. D., Paver, C. R., Reagan, J. R., Seidov, D., Smolyar, I. V. and Zweng, M. M.: World Ocean Database 2013, NOAA Atlas NESDIS 72, S. Levitus, Ed., A. Mishonov, Technical Ed.; Silver Spring, MD, pp. 209. doi: 10.7289/V5NZ85MT, 2013.

Bozec, Y., Thomas, H., Schiettecatte, L. S., Borges, A. V., Elkalay, K., & de Baar, H. J. W. (2006). Assessment of the processes controlling seasonal variations of dissolved inorganic carbon in the North Sea. *Limnology and Oceanography, 51*(6), 2746-2762.

Brewer, P. G., & Goldman, J. C. (1976). Alkalinity changes generated by phytoplankton growth. *Limnology and Oceanography, 21*(1), 108-117. doi: 10.4319/lo.1976.21.1.0108

Broecker, W. S. (1989). The salinity contrast between the Atlantic and Pacific oceans during glacial time. *Paleoceanography, 4*(2), 207-212. doi: 10.1029/PA004i002p00207

Broecker, W. S. (1991). The great ocean conveyor. *Oceanography, 4*(2), 79-89.

Broecker, W. S., & Peng, T.-H. (1982). *Tracers in the Sea*: Lamont-Doherty Geological Observatory, Columbia University.

Bushinsky, S. M., Gray, A. R., Johnson, K. S., & Sarmiento, J. L. (2017). Oxygen in the Southern Ocean from argo floats: determination of processes driving air-sea fluxes. *Journal of Geophysical Research: Oceans, 122*, 8661-8682. doi: 10.1002/2017JC012923

Cai, W.-J., Hu, X., Huang, W.-J., Jiang, L.-Q., Wang, Y., Peng, T.-H., & Zhang, X. (2010). Alkalinity distribution in the western North Atlantic Ocean margins. *Journal of Geophysical Research: Oceans, 115*(C8), C08014. doi: 10.1029/2009JC005482

Cameron, D. R., Lenton, T. M., Ridgwell, A. J., Shepherd, J. G., Marsh, R., & Yool, A. (2005). A factorial analysis of the marine carbon cycle and ocean circulation controls on atmospheric CO_2. *Global Biogeochemical Cycles, 19*(4), GB4027. doi: 10.1029/2005GB002489

Capone, D. G., & Hutchins, D. A. (2013). Microbial biogeochemistry of coastal upwelling regimes in a changing ocean. *Nature Geoscience, 6*(9), 711-717. doi: 10.1038/ngeo1916

Carter, B. R., Feely, R. A., Williams, N. L., Dickson, A. G., Fong, M. B., & Takeshita, Y. (2018). Updated methods for global locally interpolated estimation of alkalinity, pH, and nitrate. *Limnology and Oceanography: Methods, 16*(2), 119-131. doi: 10.1002/lom3.10232

Carter, B. R., Williams, N. L., Gray, A. R., & Feely, R. A. (2016). Locally interpolated alkalinity regression for global alkalinity estimation. *Limnology and Oceanography: Methods, 14*(4), 268-277. doi: 10.1002/lom3.10087

Chavez, F. P., & Messié, M. (2009). A comparison of eastern boundary upwelling ecosystems. *Progress in Oceanography, 83*(1–4), 80-96. doi: 10.1016/j.pocean.2009.07.032

Clargo, N. M., Salt, L. A., Thomas, H., & de Baar, H. J. W. (2015). Rapid increase of observed DIC and pCO_2 in the surface waters of the North Sea in the 2001-2011 decade ascribed to climate change superimposed by biological processes. *Marine Chemistry, 177*, 566-581. doi: 10.1016/j.marchem.2015.08.010

Craig, H., & Hayward, T. (1987). Oxygen supersaturation in the ocean: biological versus physical contributions. *Science, 235*(4785), 199-202. doi: 10.1126/science.235.4785.199

Dai, M., Lu, Z., Zhai, W., Chen, B., Cao, Z., Zhou, K., . . . Chenc, C. T. A. (2009). Diurnal variations of surface seawater pCO_2 in contrasting coastal environments. *Limnology and Oceanography, 54*(3), 735-745.

de Boyer Montégut, C., Madec, G., Fischer, A. S., Lazar, A., & Iudicone, D. (2004). Mixed layer depth over the global ocean: An examination of profile data and a profile-based

climatology. *Journal of Geophysical Research: Oceans, 109*, C12003. doi: 10.1029/2004JC002378

DeVries, T. (2014). The oceanic anthropogenic CO_2 sink: Storage, air-sea fluxes, and transports over the industrial era. *Global Biogeochemical Cycles, 28*(7), 631-647. doi: 10.1002/2013gb004739

DeVries, T., Holzer, M., & Primeau, F. (2017). Recent increase in oceanic carbon uptake driven by weaker upper-ocean overturning. *Nature, 542*(7640), 215-218. doi: 10.1038/nature21068

Dickson, A. G. (1981). An exact definition of total alkalinity and a procedure for the estimation of alkalinity and total inorganic carbon from titration data. *Deep Sea Research Part A. Oceanographic Research Papers, 28*(6), 609-623. doi: 10.1016/0198-0149(81)90121-7

Dickson, A. G. (1990). Standard potential of the reaction: AgCl (s)+ $12H_2$ (g)= Ag (s)+ HCl (aq), and and the standard acidity constant of the ion HSO_4^- in synthetic sea water from 273.15 to 318.15 K. *The Journal of Chemical Thermodynamics, 22*(2), 113-127.

Dickson, A. G., & Millero, F. J. (1987). A comparison of the equilibrium constants for the dissociation of carbonic acid in seawater media. *Deep Sea Research, 34*(10), 1733-1743.

Dickson, A. G., & Riley, J. P. (1978). The effect of analytical error on the evaluation of the components of the aquatic carbon-dioxide system. *Marine Chemistry, 6*(1), 77-85. doi: 10.1016/0304-4203(78)90008-7

Dittmar, T., & Kattner, G. (2003). The biogeochemistry of the river and shelf ecosystem of the Arctic Ocean: a review. *Marine Chemistry, 83*(3), 103-120. doi: 10.1016/S0304-4203(03)00105-1

Doney, S. C., Fabry, V. J., Feely, R. A., & Kleypas, J. A. (2009). Ocean acidification: the other CO_2 problem. *Ann Rev Mar Sci, 1*, 169-192. doi: 10.1146/annurev.marine.010908.163834

Dong, S., Sprintall, J., Gille, S. T., & Talley, L. (2008). Southern Ocean mixed-layer depth from Argo float profiles. *Journal of Geophysical Research: Oceans, 113*(C6), C06013. doi: 10.1029/2006JC004051

Dore, J. E., Lukas, R., Sadler, D. W., Church, M. J., & Karl, D. M. (2009). Physical and biogeochemical modulation of ocean acidification in the central North Pacific. *Proceedings of the National Academy of Sciences, 106*(30), 12235-12240. doi: 10.1073/pnas.0906044106

Evans, D. G., Zika, J. D., Naveira Garabato, A. C., & Nurser, A. J. G. (2014). The imprint of Southern Ocean overturning on seasonal water mass variability in Drake Passage. *Journal of Geophysical Research: Oceans, 119*(11), 7987-8010. doi: 10.1002/2014JC010097

Evans, W., Hales, B., Strutton, P. G., Shearman, R. K., & Barth, J. A. (2015). Failure to bloom: Intense upwelling results in negligible phytoplankton response and prolonged CO_2 outgassing over the Oregon shelf. *Journal of Geophysical Research: Oceans, 120*, 1446-1461. doi: 10.1002/2014JC010580

Falkowski, P. G., Scholes, R. J., Boyle, E., Canadell, J., Canfield, D., Elser, J., . . . Steffen, W. (2000). The Global Carbon Cycle: A Test of Our Knowledge of Earth as a System. *Science, 290*(5490), 291-296. doi: 10.1126/science.290.5490.291

Fay, A. R., Lovenduski, N. S., McKinley, G. A., Munro, D. R., Sweeney, C., Gray, A. R., . . . Williams, N. (2018). Utilizing the Drake Passage Time-series to understand variability and change in subpolar Southern Ocean pCO_2. *Biogeosciences, 15*(12), 3841-3855. doi: 10.5194/bg-15-3841-2018

Feely, R.A. (2008). Ocean Acidification. In State of the Climate in 2007. *Bulletin of the American Meteorological Society*, *89*(7), S58. doi: 10.1175/1520-0477-89.7.S10

Ferrari, R., Jansen, M. F., Adkins, J. F., Burke, A., Stewart, A. L., & Thompson, A. F. (2014). Antarctic sea ice control on ocean circulation in present and glacial climates. *Proceedings of the National Academy of Sciences, 111*(24), 8753-8758. doi: 10.1073/pnas.1323922111

Frigstad, H., Andersen, T., Hessen, D. O., Naustvoll, L. J., Johnsen, T. M., & Bellerby, R. G. J. (2011). Seasonal variation in marine C:N:P stoichiometry: can the composition of seston explain stable Redfield ratios? *Biogeosciences, 8*(10), 2917-2933. doi: 10.5194/bg-8-2917-2011

Friis, K., Körtzinger, A., & Wallace, D. W. (2003). The salinity normalization of marine inorganic carbon chemistry data. *Geophysical Research Letters, 30*(2), 1080. doi: 10.1029/2002GL015898

Fry, C. H., Tyrrell, T., & Achterberg, E. P. (2016). Analysis of longitudinal variations in North Pacific alkalinity to improve predictive algorithms. *Global Biogeochemical Cycles, 30*. doi: 10.1002/2016GB005398

Fry, C. H., Tyrrell, T., Hain, M. P., Bates, N. R., & Achterberg, E. P. (2015). Analysis of global surface ocean alkalinity to determine controlling processes. *Marine Chemistry, 174*, 46-57. doi: 10.1016/j.marchem.2015.05.003

Fujii, M., & Yamanaka, Y. (2008). Effects of storms on primary productivity and air-sea CO_2 exchange in the subarctic western North Pacific: a modeling study. *Biogeosciences, 5*(4), 1189-1197. doi: 10.5194/bg-5-1189-2008

García-Reyes, M., & Largier, J. L. (2012). Seasonality of coastal upwelling off central and northern California: New insights, including temporal and spatial variability. *Journal of Geophysical Research: Oceans*, 117, C03028. doi: 10.1029/2011JC007629

Garcia, H., & Gordon, L. (1993). Erratum: Oxygen solubility in seawater: Better fitting equations. *Limnology and Oceanography*, *38*(3), 656.

Garcia, H. E., & Gordon, L. I. (1992). Oxygen solubility in seawater: Better fitting equations. *Limnology and Oceanography*, *37*(6), 1307-1312. doi: 10.4319/lo.1992.37.6.1307

González-Dávila, M., Santana-Casiano, J. M., Rueda, M. J., & Llinás, O. (2010). The water column distribution of carbonate system variables at the ESTOC site from 1995 to 2004. *Biogeosciences*, *7*(10), 3067-3081. doi: 10.5194/bg-7-3067-2010

Gray, A. R., Johnson, K. S., Bushinsky, S. M., Riser, S. C., Russell, J. L., Talley, L. D., . . . Sarmiento, J. L. (2018). Autonomous biogeochemical floats detect significant carbon dioxide outgassing in the high-latitude Southern Ocean. *Geophysical Research Letters, 45*(17), 9049-9057. doi: 10.1029/2018GL078013

Gruber, N. (1998). Anthropogenic CO_2 in the Atlantic Ocean. *Global Biogeochemical Cycles, 12*(1), 165-191. doi: 10.1029/97GB03658

Gruber, N., Gloor, M., Fan, S.-M., & Sarmiento, J. L. (2001). Air-sea flux of oxygen estimated from bulk data: Implications For the marine and atmospheric oxygen cycles. *Global Biogeochemical Cycles, 15*(4), 783-803. doi: 10.1029/2000GB001302

Gruber, N., Gloor, M., Mikaloff Fletcher, S. E., Doney, S. C., Dutkiewicz, S., Follows, M. J., . . . Lindsay, K. (2009). Oceanic sources, sinks, and transport of atmospheric CO_2. *Global Biogeochemical Cycles, 23*(1).

Gruber, N., Landschützer, P., & Lovenduski, N. S. (2019). The variable Southern Ocean carbon sink. *Ann Rev Mar Sci*, *11*(1), 159-186. doi: 10.1146/annurev-marine-121916-063407

Gruber, N., Keeling, C. D., & Bates, N. R. (2002). Interannual variability in the North Atlantic Ocean carbon sink. *Science, 298*(5602), 2374-2378. doi: 10.1126/science.1077077

Gruber, N., & Sarmiento, J. L. (2002). Large-scale biogeochemical/physical interactions in elemental cycles. *The Sea, 12*, 337-399.

Guéguen, C., & Tortell, P. D. (2008). High-resolution measurement of Southern Ocean CO_2 and O_2/Ar by membrane inlet mass spectrometry. *Marine Chemistry, 108*(3), 184-194. doi: 10.1016/j.marchem.2007.11.007

IOC, SCOR, and IAPSO (2010). The international thermodynamic equation of seawater—2010: Calculation and use of thermodynamic properties [in English], Manuals and Guides 56, Intergovernmental Oceanographic Commission, UNESCO.

Helm, K. P., Bindoff, N. L., & Church, J. A. (2011). Observed decreases in oxygen content of the global ocean. *Geophysical Research Letters, 38*, L23602. doi: 10.1029/2011GL049513

Henson, S. A., Dunne, J. P., & Sarmiento, J. L. (2009). Decadal variability in North Atlantic phytoplankton blooms. *Journal of Geophysical Research: Oceans, 114*, C04013. doi: 10.1029/2008JC005139

Holzer, M., Primeau, F. W., DeVries, T., & Matear, R. (2014). The Southern Ocean silicon trap: Data-constrained estimates of regenerated silicic acid, trapping efficiencies, and global transport paths. *Journal of Geophysical Research: Oceans, 119*(1), 313-331. doi: 10.1002/2013JC009356

Humphreys, M. P. (2017). Climate sensitivity and the rate of ocean acidification: future impacts, and implications for experimental design. *ICES Journal of Marine Science, 74*(4), 934-940. doi: 10.1093/icesjms/fsw189

Humphreys, M. P., Daniels, C. J., Wolf-Gladrow, D. A., Tyrrell, T., & Achterberg, E. P. (2018). On the influence of marine biogeochemical processes over CO_2 exchange between the atmosphere and ocean. *Marine Chemistry, 199*, 1-11. doi: 10.1016/j.marchem.2017.12.006

Humphreys, M. P., Griffiths, A. M., Achterberg, E. P., Holliday, N. P., Rérolle, V. M. C., Menzel Barraqueta, J.-L., . . . Boyce, A. J. (2016). Multidecadal accumulation of anthropogenic and remineralized dissolved inorganic carbon along the Extended Ellett Line in the northeast Atlantic Ocean. *Global Biogeochemical Cycles, 30*, 293-310. doi: 10.1002/2015GB005246

IPCC (2013), Summary for Policymakers. In: Climate Change 2013: The Physical Science Basis., Contribution of Working Group I to the Fifth Assessment Report of the Intergovernmental Panel on Climate Change [Stocker, T.F., D. Qin, G.-K. Plattner, M. Tignor, S. K. Allen, J. Boschung, A. Nauels, Y. Xia, V. Bex and P.M. Midgley (eds.)]. Cambridge University Press, Cambridge, United Kingdom and New York, NY, USA.

Jiang, L. Q., Feely, R. A., Carter, B. R., Greeley, D. J., Gledhill, D. K., & Arzayus, K. M. (2015). Climatological distribution of aragonite saturation state in the global oceans. *Global Biogeochemical Cycles, 29*. doi: 10.1002/2015GB005198

Jiang, Z. P., Hydes, D. J., Tyrrell, T., Hartman, S. E., Hartman, M. C., Dumousseaud, C., . . . González -Pola, C. (2013). Key controls on the seasonal and interannual variations of the carbonate system and air-sea CO_2 flux in the Northeast Atlantic (Bay of Biscay). *Journal of Geophysical Research: Oceans, 118*(2), 785-800. doi: 10.1002/jgrc.20087

Jiang, Z. P., Tyrrell, T., Hydes, D. J., Dai, M., & Hartman, S. E. (2014). Variability of alkalinity and the alkalinity-salinity relationship in the tropical and subtropical surface ocean. *Global Biogeochemical Cycles, 28*(7), 729-742. doi: 10.1002/2013GB004678

Johnson, K. S., Plant, J. N., Coletti, L. J., Jannasch, H. W., Sakamoto, C. M., Riser, S. C., . . . Sarmiento, J. L. (2017). Biogeochemical sensor performance in the SOCCOM profiling float array. *Journal of Geophysical Research: Oceans, 122*(8), 6416-6436. doi: 10.1002/2017JC012838

Jones, D. C., Ito, T., Takano, Y., & Hsu, W.-C. (2014). Spatial and seasonal variability of the air-sea equilibration timescale of carbon dioxide. *Global Biogeochemical Cycles, 28*(11), 1163-1178. doi: 10.1002/2014GB004813

Juranek, L. W., Feely, R. A., Peterson, W. T., Alin, S. R., Hales, B., Lee, K., Sabine, C. L., and Peterson, J.: A novel method for determination of aragonite saturation state on the continental shelf of central Oregon using multi-parameter relationships with hydrographic data, *Geophysical Research Lettter*, *36*, L24601, doi: 10.1029/2009GL040778, 2009.

Kawakami, H., Honda, M. C., Wakita, M., & Watanabe, S. (2007). Time-series observation of dissolved inorganic carbon and nutrients in the northwestern North Pacific. *Journal of Oceanography, 63*(6), 967-982. doi: 10.1007/s10872-007-0081-y

Keeling, C. D., Brix, H., & Gruber, N. (2004). Seasonal and long-term dynamics of the upper ocean carbon cycle at Station ALOHA near Hawaii. *Global Biogeochemical Cycles, 18*(4). doi: 10.1029/2004GB002227

Key, R. M., Kozyr, A., Sabine, C. L., Lee, K., Wanninkhof, R., Bullister, J. L., . . . Peng, T. H. (2004). A global ocean carbon climatology: Results from Global Data Analysis Project (GLODAP). *Global Biogeochemical Cycles, 18*(4), GB4031. doi: 10.1029/2004GB002247

Key, R. M., Olsen, A., Van Heuven, S., Lauvset, S. K., Velo, A., Lin, X., . . . Hoppema, M. (2015). Global Ocean Data Analysis Project, Version 2 (GLODAPv2). *ORNL/CDIAC-162, NDP-093*. doi: 10.3334/CDIAC/OTG.NDP093_GLODAPv2

Körtzinger, A., Send, U., Wallace, D. W., Karstensen, J., & DeGrandpre, M. (2008). Seasonal cycle of O_2 and pCO_2 in the central Labrador Sea: Atmospheric, biological, and physical implications. *Global Biogeochemical Cycles, 22*(1), GB1014. doi: 10.1029/2007GB003029

Landschützer, P., Gruber, N., Bakker, D., & Schuster, U. (2014). Recent variability of the global ocean carbon sink. *Global Biogeochemical Cycles, 28*(9), 927-949.

Landschützer, P., Gruber, N., Haumann, F. A., Rödenbeck, C., Bakker, D. C. E., Van Heuven, S., . . . Wanninkhof, R. (2015). The reinvigoration of the Southern Ocean carbon sink. *Science, 349*(6253), 1221-1224. doi: 10.1126/science.aab2620

Lauvset, S. K., & Tanhua, T. (2015). A toolbox for secondary quality control on ocean chemistry and hydrographic data. *Limnology and Oceanography: Methods, 13*(11), 601-608. doi: 10.1002/lom3.10050

Le Quéré, C., Rödenbeck, C., Buitenhuis, E. T., Conway, T. J., Langenfelds, R., Gomez, A., . . . Heimann, M. (2007). Saturation of the Southern Ocean CO_2 sink due to recent climate change. *Science, 316*(5832), 1735-1738. doi: 10.1126/science.1136188

Le Quéré, C., Andrew, R. M., Friedlingstein, P., Sitch, S., Pongratz, J., Manning, A. C., . . . Zhu, D. (2018). Global Carbon Budget 2017. *Earth Syst. Sci. Data, 10*(1), 405-448. doi: 10.5194/essd-10-405-2018

Lee, K., Choi, S. D., Park, G. H., Wanninkhof, R., Peng, T. H., Key, R. M., . . . Kozyr, A. (2003). An updated anthropogenic CO_2 inventory in the Atlantic Ocean. *Global Biogeochemical Cycles, 17*(4), 1116. doi: 10.1029/2003GB002067

Lee, K., Kim, T.-W., Byrne, R. H., Millero, F. J., Feely, R. A., & Liu, Y.-M. (2010). The universal ratio of boron to chlorinity for the North Pacific and North Atlantic oceans. *Geochimica et Cosmochimica Acta, 74*(6), 1801-1811. doi: 10.1016/j.gca.2009.12.027

Lee, K., Tong, L. T., Millero, F. J., Sabine, C. L., Dickson, A. G., Goyet, C., . . . Key, R. M. (2006). Global relationships of total alkalinity with salinity and temperature in surface waters of the world's oceans. *Geophysical Research Letters, 33*(19), L19605. doi: 10.1029/2006GL027207

Lee, K., Wanninkhof, R., Feely, R. A., Millero, F. J., & Peng, T. H. (2000). Global relationships of total inorganic carbon with temperature and nitrate in surface seawater. *Global Biogeochemical Cycles, 14*(3), 979-994. doi: 10.1029/1998gb001087

Lefèvre, N., Guillot, A., Beaumont, L., & Danguy, T. (2008). Variability of fCO_2 in the Eastern Tropical Atlantic from a moored buoy. *Journal of Geophysical Research: Oceans (1978–2012), 113*(C1), C01015. doi: 10.1029/2007JC004146

Loose, B., McGillis, W. R., Schlosser, P., Perovich, D., & Takahashi, T. (2009). Effects of freezing, growth, and ice cover on gas transport processes in laboratory seawater experiments. *Geophysical Research Letters, 36*(5), L05603. doi: 10.1029/2008GL036318

Louanchi, F., Ruiz-Pino, D. P., Jeandel, C., Brunet, C., Schauer, B., Masson, A., . . . Poisson, A. (2001). Dissolved inorganic carbon, alkalinity, nutrient and oxygen seasonal and interannual variations at the Antarctic Ocean JGOFS-KERFIX site. *Deep Sea Research Part I: Oceanographic Research Papers, 48*(7), 1581-1603. doi: 10.1016/S0967-0637(00)00086-8

Louanchi, F., Ruiz-Pino, D. P., & Poisson, A. (1999). Temporal variations of mixed-layer oceanic CO2 at JGOFS-KERFIX time-series station: Physical versus biogeochemical processes. *Journal of Marine Research, 57*(1), 165-187. doi: 10.1357/002224099765038607

Lovenduski, N. S., Gruber, N., & Doney, S. C. (2008). Toward a mechanistic understanding of the decadal trends in the Southern Ocean carbon sink. *Global Biogeochemical Cycles, 22*(3). doi: 10.1029/2007gb003139

Lovenduski, N. S., Gruber, N., Doney, S. C., & Lima, I. D. (2007). Enhanced CO_2 outgassing in the Southern Ocean from a positive phase of the Southern Annular Mode. *Global Biogeochemical Cycles, 21*(2). doi: 10.1029/2006gb002900

Lueker, T. J., Dickson, A. G., & Keeling, C. D. (2000). Ocean pCO_2 calculated from dissolved inorganic carbon, alkalinity, and equations for K1 and K2: validation based on laboratory measurements of CO_2 in gas and seawater at equilibrium. *Marine Chemistry, 70*(1–3), 105-119. doi: 10.1016/S0304-4203(00)00022-0

Lumpkin, R., & Speer, K. (2007). Global ocean meridional overturning. *Journal of Physical Oceanography, 37*(10), 2550-2562. doi: 10.1175/JPO3130.1

Mahadevan, A., D'Asaro, E., Lee, C., & Perry, M. J. (2012). Eddy-Driven Stratification Initiates North Atlantic Spring Phytoplankton Blooms. *Science, 337*(6090), 54-58. doi: 10.1126/science.1218740

Marinov, I., Gnanadesikan, A., Toggweiler, J. R., & Sarmiento, J. L. (2006). The Southern Ocean biogeochemical divide. *Nature, 441*(7096), 964-967. doi: 10.1038/nature04883

Marshall, J., & Speer, K. (2012). Closure of the meridional overturning circulation through Southern Ocean upwelling. *Nature Geoscience, 5*(3), 171-180.

Martiny, A. C., Pham, C. T. A., Primeau, F. W., Vrugt, J. A., Moore, J. K., Levin, S. A., & Lomas, M. W. (2013). Strong latitudinal patterns in the elemental ratios of marine plankton and organic matter. *Nature Geoscience, 6*(4), 279-283. doi: 10.1038/ngeo1757

McDougall, T.J. and P.M. Barker. (2011). Getting started with TEOS-10 and the Gibbs Seawater (GSW) Oceanographic Toolbox, 28pp., SCOR/IAPSO WG127, ISBN 978-0-646-55621-5.

McGregor, H. V., Dima, M., Fischer, H. W., & Mulitza, S. (2007). Rapid 20th-Century Increase in Coastal Upwelling off Northwest Africa. *Science, 315*(5812), 637-639. doi: 10.1126/science.1134839

Mecking, S., Langdon, C., Feely, R. A., Sabine, C. L., Deutsch, C. A., & Min, D.-H. (2008). Climate variability in the North Pacific thermocline diagnosed from oxygen measurements: An update based on the U.S. CLIVAR/CO2 Repeat Hydrography cruises. *Global Biogeochemical Cycles, 22*(3), GB3015. doi: 10.1029/2007GB003101

Merlivat, L., Boutin, J., & Antoine, D. (2015). Roles of biological and physical processes in driving seasonal air–sea CO_2 flux in the Southern Ocean: New insights from CARIOCA pCO_2. *Journal of Marine Systems, 147*, 9-20. doi: 10.1016/j.jmarsys.2014.04.015

Mikaloff-Fletcher, S. E. (2015). An increasing carbon sink? *Science, 349*(6253), 1165. doi: 10.1126/science.aad0912

Mikaloff Fletcher, S. E., Gruber, N., Jacobson, A. R., Doney, S. C., Dutkiewicz, S., Gerber, M., . . . Sarmiento, J. L. (2006). Inverse estimates of anthropogenic CO_2 uptake, transport, and storage by the ocean. *Global Biogeochemical Cycles, 20*(2). doi: 10.1029/2005gb002530

Millero, F. J., Degler, E. A., O'Sullivan, D. W., Goyet, C., & Eischeid, G. (1998). The carbon dioxide system in the Arabian Sea. *Deep Sea Research Part II: Topical Studies in Oceanography, 45*(10–11), 2225-2252. doi: 10.1016/S0967-0645(98)00069-1

Moore, C. M. (2016). Diagnosing oceanic nutrient deficiency. *Philosophical Transactions of the Royal Society A, 374*, 20152090. doi: 10.1098/rsta.2015.0290

Moore, C. M., Mills, M. M., Arrigo, K. R., Berman-Frank, I., Bopp, L., Boyd, P. W., . . . Ulloa, O. (2013). Processes and patterns of oceanic nutrient limitation. *Nature Geoscience, 6*(9), 701-710. doi: 10.1038/ngeo1765

Morrison, A. K., Frölicher, T. L., & Sarmiento, J. L. (2015). Upwelling in the Southern Ocean. *Physics Today, 68*(1), 27-32. doi: 10.1063/pt.3.2654

Munro, D. R., Lovenduski, N. S., Stephens, B. B., Newberger, T., Arrigo, K. R., Takahashi, T., . . . Sweeney, C. (2015a). Estimates of net community production in the Southern Ocean determined from time series observations (2002–2011) of nutrients, dissolved inorganic

carbon, and surface ocean pCO_2 in Drake Passage. *Deep Sea Research Part II: Topical Studies in Oceanography, 114*, 49-63. doi: 10.1016/j.dsr2.2014.12.014

Munro, D. R., Lovenduski, N. S., Takahashi, T., Stephens, B. B., Newberger, T., & Sweeney, C. (2015b). Recent evidence for a strengthening CO_2 sink in the Southern Ocean from carbonate system measurements in the Drake Passage (2002–2015). *Geophysical Research Letters, 42*(18), 7623-7630. doi: 10.1002/2015GL065194

Murray, J. W., Barber, R. T., Roman, M. R., Bacon, M. P., & Feely, R. A. (1994). Physical and biological controls on carbon cycling in the Equatorial Pacific. *Science, 266*(5182), 58-65. doi: 10.1126/science.266.5182.58

Nielsdóttir, M. C., Moore, C. M., Sanders, R., Hinz, D. J., & Achterberg, E. P. (2009). Iron limitation of the postbloom phytoplankton communities in the Iceland Basin. *Global Biogeochemical Cycles, 23*(3), GB3001. doi: 10.1029/2008GB003410

Nomura, D., Yoshikawa-Inoue, H., & Toyota, T. (2006). The effect of sea-ice growth on air–sea CO_2 flux in a tank experiment. *Tellus B: Chemical and Physical Meteorology, 58*(5), 418-426. doi: 10.1111/j.1600-0889.2006.00204.x

Ohno, Y., Iwasaka, N., Kobashi, F., & Sato, Y. (2009). Mixed layer depth climatology of the North Pacific based on Argo observations. *Journal of Oceanography, 65*(1), 1-16. doi: 10.1007/s10872-009-0001-4

Olsen, A., Key, R. M., Van Heuven, S., Lauvset, S. K., Velo, A., Lin, X., . . . Suzuki, T. (2016). The Global Ocean Data Analysis Project version 2 (GLODAPv2) – an internally consistent data product for the world ocean. *Earth Syst. Sci. Data, 8*(2), 297-323. doi: 10.5194/essd-8-297-2016

Omta, A. W., Dutkiewicz, S., & Follows, M. J. (2011). Dependence of the ocean-atmosphere partitioning of carbon on temperature and alkalinity. *Global Biogeochemical Cycles, 25*(1). doi: 10.1029/2010GB003839

Orr, J. C., Fabry, V. J., Aumont, O., Bopp, L., Doney, S. C., Feely, R. A., . . . Yool, A. (2005). Anthropogenic ocean acidification over the twenty-first century and its impact on calcifying organisms. *Nature, 437*(7059), 681-686. doi: 10.1038/nature04095

Postma, H. (1964). The exchange of oxygen and carbon dioxide between the ocean and the atmosphere. *Netherlands Journal of Sea Research, 2*(2), 258-283. doi: 10.1016/0077-7579(64)90013-4

Redfield, A. C. (1963). The influence of organisms on the composition of sea-water. *The Sea*, 26-77.

Ribas-Ribas, M., Rérolle, V. M. C., Bakker, D. C. E., Kitidis, V., Lee, G. A., Brown, I., . . . Tyrrell, T. (2014). Intercomparison of carbonate chemistry measurements on a cruise in northwestern European shelf seas. *Biogeosciences, 11*(16), 4339-4355. doi: 10.5194/bg-11-4339-2014

Ruttenberg, K. C. (2003). The Global Phosphorus Cycle. In K. K. Turekian (Ed.), *Treatise on Geochemistry* (pp. 585-643). Oxford: Pergamon.

Sabine, C. L., Feely, R. A., Gruber, N., Key, R. M., Lee, K., Bullister, J. L., . . . Tilbrook, B. (2004). The oceanic sink for anthropogenic CO_2. *Science, 305*(5682), 367-371.

Sabine, C. L., Key, R. M., Feely, R. A., & Greeley, D. (2002). Inorganic carbon in the Indian Ocean: Distribution and dissolution processes. *Global Biogeochemical Cycles, 16*(4), 1067. doi: 10.1029/2002GB001869

Sabine, C. L., Key, R. M., Johnson, K. M., Millero, F. J., Poisson, A., Sarmiento, J. L., . . . Winn, C. D. (1999). Anthropogenic CO_2 inventory of the Indian Ocean. *Global Biogeochemical Cycles, 13*(1), 179-198. doi: 10.1029/1998GB900022

Saito, H., Tsuda, A., & Kasai, H. (2002). Nutrient and plankton dynamics in the Oyashio region of the western subarctic Pacific Ocean. *Deep Sea Research Part II: Topical Studies in Oceanography, 49*(24), 5463-5486. doi: 10.1016/S0967-0645(02)00204-7

Sarmiento, J. L., & Gruber N. (2006). Ocean Biogeochemical Dynamics, pp. 582, Princeton Univ. Press, Princeton, New Jersey, USA.

Sarmiento, J. L., Gruber, N., Brzezinski, M. A., & Dunne, J. P. (2004). High-latitude controls of thermocline nutrients and low latitude biological productivity. *Nature, 427*(6969), 56-60. doi: 10.1038/nature02127

Sarmiento, J. L., Slater, R., Barber, R., Bopp, L., Doney, S. C., Hirst, A. C., . . . Stouffer, R. (2004). Response of ocean ecosystems to climate warming. *Global Biogeochemical Cycles, 18*(3), GB3003. doi: 10.1029/2003GB002134

Sarmiento, J. L., & Toggweiler, J. R. (1984). A new model for the role of the oceans in determining atmospheric pCO_2. *Nature, 308*(5960), 621-624. doi: 10.1038/308621a0

Schlitzer, R. (2000). Applying the adjoint method for biogeochemical modeling: export of participate organic matter in the world ocean. *Inverse Methods in Global Biogeochemical Cycles, 114*, 107-124.

Schmidtko, S., Stramma, L., & Visbeck, M. (2017). Decline in global oceanic oxygen content during the past five decades. *Nature, 542*, 335. doi: 10.1038/nature21399

Shiomoto, A. (2000). Chlorophyll-a and primary production during spring in the oceanic region of the Oyashio Water, the north-western Pacific. *Journal of the Marine Biological Association of the United Kingdom, 80*(2), 343-354.

Sprintall, J., Chereskin, T. K., & Sweeney, C. (2012). High-resolution underway upper ocean and surface atmospheric bbservations in Drake Passage: synergistic measurements for climate science. *Oceanography, 25*(3), 70-81.

Stramma, L., Johnson, G. C., Sprintall, J., & Mohrholz, V. (2008). Expanding oxygen-minimum zones in the tropical oceans. *Science, 320*(5876), 655-658. doi: 10.1126/science.1153847

Takahashi, T., Sutherland, S. C., Chipman, D. W., Goddard, J. G., Ho, C., Newberger, T., . . . Munro, D. R. (2014). Climatological distributions of pH, pCO_2, total CO_2, alkalinity, and $CaCO_3$ saturation in the global surface ocean, and temporal changes at selected locations. *Marine Chemistry, 164*(0), 95-125. doi: 10.1016/j.marchem.2014.06.004

Takahashi, T., Sutherland, S. C., Wanninkhof, R., Sweeney, C., Feely, R. A., Chipman, D. W., . . . Sabine, C. (2009). Climatological mean and decadal change in surface ocean pCO_2, and net sea–air CO_2 flux over the global oceans. *Deep Sea Research II, 56*(8), 554-577.

Takeshita, Y., Johnson, K. S., Martz, T. R., Plant, J. N., & Sarmiento, J. L. (2018). Assessment of Autonomous pH Measurements for Determining Surface Seawater Partial Pressure of CO_2. *Journal of Geophysical Research: Oceans*, *123*(6), 4003-4013. doi: 10.1029/2017JC013387

Talley, L. D. (2013). Closure of the global overturning circulation through the Indian, Pacific, and Southern Oceans: Schematics and transports. *Oceanography, 26*(1), 80-97. doi: 10.5670/oceanog.2013.07

Talley, L. D., Reid, J. L., & Robbins, P. E. (2003). Data-Based Meridional Overturning Streamfunctions for the Global Ocean. *Journal of Climate*, *16*, 3213-3226. doi: 10.1175/1520-0442(2003)016<3213:dmosft>2.0.co;2

Tanhua, T., van Heuven, S., Key, R. M., Velo, A., Olsen, A., & Schirnick, C. (2010). Quality control procedures and methods of the CARINA database. *Open Access Earth System Science Data*, *2*, 35-49. doi: 10.5194/essd-2-35-2010

Toggweiler, J. R., Gnanadesikan, A., Carson, S., Murnane, R., & Sarmiento, J. L. (2003a). Representation of the carbon cycle in box models and GCMs: 1. Solubility pump. *Global Biogeochemical Cycles, 17*(1), 1026. doi: 10.1029/2001GB001401

Toggweiler, J. R., Murnane, R., Carson, S., Gnanadesikan, A., & Sarmiento, J. L. (2003b). Representation of the carbon cycle in box models and GCMs, 2, Organic pump. *Global Biogeochemical Cycles, 17*(1), 1027. doi: 10.1029/2001GB001841

Tortell, P. D., Asher, E. C., Ducklow, H. W., Goldman, J. A. L., Dacey, J. W. H., Grzymski, J. J., . . . Morel, F. M. M. (2014). Metabolic balance of coastal Antarctic waters revealed by autonomous pCO_2 and ΔO_2/Ar measurements. *Geophysical Research Letters, 41*(19), 6803-6810. doi: 10.1002/2014GL061266

Tortell, P. D., Bittig, H. C., Körtzinger, A., Jones, E. M., & Hoppema, M. (2015). Biological and physical controls on N_2, O_2, and CO_2 distributions in contrasting Southern Ocean surface waters. *Global Biogeochemical Cycles, 29*(7), 994-1013. doi: 10.1002/2014GB004975

Tortell, P. D., & Long, M. C. (2009). Spatial and temporal variability of biogenic gases during the Southern Ocean spring bloom. *Geophysical Research Letters, 36*(1), L01603. doi: 10.1029/2008GL035819

Tyrrell, T. (1999). The relative influences of nitrogen and phosphorus on oceanic primary production. *Nature, 400*(6744), 525-531. doi: 10.1038/22941

Van Heuven, S., D. Pierrot, J.W.B. Rae, E. Lewis, and D.W.R. Wallace. (2011). MATLAB Program Developed for CO_2 System Calculations. ORNL/CDIAC-105b. Carbon Dioxide Information Analysis Center, Oak Ridge National Laboratory, U.S. Department of Energy, Oak Ridge, Tennessee. doi: 10.3334/CDIAC/otg.CO2SYS_MATLAB_v1.1

Vance, D., Little, S. H., de Souza, G. F., Khatiwala, S., Lohan, M. C., & Middag, R. (2017). Silicon and zinc biogeochemical cycles coupled through the Southern Ocean. *Nature Geoscience, 10*(3), 202-206. doi: 10.1038/ngeo2890

Vázquez-Rodríguez, M., Touratier, F., Lo Monaco, C., Waugh, D. W., Padin, X. A., Bellerby, R. G. J., . . . Pérez, F. F. (2009). Anthropogenic carbon distributions in the Atlantic Ocean: data-based estimates from the Arctic to the Antarctic. *Biogeosciences, 6*(3), 439-451. doi: 10.5194/bg-6-439-2009

Wang, D., Gouhier, T. C., Menge, B. A., & Ganguly, A. R. (2015). Intensification and spatial homogenization of coastal upwelling under climate change. *Nature, 518*(7539), 390-394. doi: 10.1038/nature14235

Weiss, R. F. (1970). The solubility of nitrogen, oxygen and argon in water and seawater. *Deep Sea Research and Oceanographic Abstracts, 17*(4), 721-735. doi: 10.1016/0011-7471(70)90037-9

Weiss, R. F. (1974). Carbon dioxide in water and seawater: the solubility of a non-ideal gas. *Marine Chemistry, 2*(3), 203-215.

Weiss, R. F., & Price, B. A. (1980). Nitrous oxide solubility in water and seawater. *Marine Chemistry, 8*(4), 347-359. doi: 10.1016/0304-4203(80)90024-9

Williams, N. L., Juranek, L. W., Feely, R. A., Johnson, K. S., Sarmiento, J. L., Talley, L. D., . . . Takeshita, Y. (2017). Calculating surface ocean pCO_2 from biogeochemical Argo floats equipped with pH: An uncertainty analysis. *Global Biogeochemical Cycles, 31*(3), 591-604. doi: 10.1002/2016GB005541

Williams, N. L., Juranek, L. W., Feely, R. A., Russell, J. L., Johnson, K. S., & Hales, B. (2018). Assessment of the carbonate chemistry seasonal cycles in the Southern Ocean from persistent observational platforms. *Journal of Geophysical Research: Oceans, 123*(7), 4833-4852. doi: 10.1029/2017JC012917

Williams, N. L., Juranek, L. W., Johnson, K. S., Feely, R. A., Riser, S. C., Talley, L. D., . . . Wanninkhof, R. (2016). Empirical algorithms to estimate water column pH in the Southern Ocean. *Geophysical Research Letters, 43*(7), 3415-3422. doi: 10.1002/2016GL068539

Williams, R. G., & Follows, M. J. (2011). *Ocean dynamics and the carbon cycle: Principles and mechanisms*: Cambridge University Press.

Wolf-Gladrow, D. A., Zeebe, R. E., Klaas, C., Körtzinger, A., & Dickson, A. G. (2007). Total alkalinity: The explicit conservative expression and its application to biogeochemical processes. *Marine Chemistry, 106*(1), 287-300. doi: j.marchem.2007.01.006

Wong, C. S., Waser, N. A. D., Whitney, F. A., Johnson, W. K., & Page, J. S. (2002). Time-series study of the biogeochemistry of the North East subarctic Pacific: reconciliation of the Corg/N remineralization and uptake ratios with the Redfield ratios. *Deep Sea Research Part II: Topical Studies in Oceanography, 49*(24), 5717-5738. doi: 10.1016/S0967-0645(02)00211-4

Woodgate, R. A., Aagaard, K., & Weingartner, T. J. (2006). Interannual changes in the Bering Strait fluxes of volume, heat and freshwater between 1991 and 2004. *Geophysical Research Letters, 33*(15). doi: 10.1029/2006GL026931

Yasunaka, S., Nojiri, Y., Nakaoka, S.-i., Ono, T., Mukai, H., & Usui, N. (2013). Monthly maps of sea surface dissolved inorganic carbon in the North Pacific: Basin-wide distribution and seasonal variation. *Journal of Geophysical Research: Oceans, 118*(8), 3843-3850. doi: 10.1002/jgrc.20279

Yates, K. K., Dufore, C., Smiley, N., Jackson, C., & Halley, R. B. (2007). Diurnal variation of oxygen and carbonate system parameters in Tampa Bay and Florida Bay. *Marine Chemistry, 104*(1), 110-124.

Zeebe, R. E. (2012). History of Seawater Carbonate Chemistry, Atmospheric CO_2, and Ocean Acidification. *Annual Review of Earth and Planetary Sciences, 40*(1), 141-165. doi: 10.1146/annurev-earth-042711-105521

Zeebe, R. E., & Wolf-Gladrow, D. A. (2001). CO_2 in seawater: equilibrium, kinetics, isotopes (Vol. 65): Elsevier Oceanography Series.

Zhai, W., Dai, M., & Cai, W.-J. (2009). Coupling of surface pCO_2 and dissolved oxygen in the northern South China Sea: impacts of contrasting coastal processes. *Biogeosciences, 6*(11), 2589-2598. doi: 10.5194/bg-6-2589-2009